Technical Physics Letters, Vol. 27, No. 3, 2001, pp. 173–175. Translated from Pis'ma v Zhurnal Tekhnicheskoĭ Fiziki, Vol. 27, No. 5, 2001, pp. 1–7.

High-Efficiency 3.4–4.4 μm Light-Emitting Diodes Based on a *p*-AlGaAsSb/*n*-InGaAsSb/*n*-AlGaAsSb Heterostructure Operating at Room Temperature

B. Zhurtanov, É. V. Ivanov, A. N. Imenkov, N. M. Kolchanova, A. E. Rozov, N. Stoyanov, and Yu. P. Yakovlev

Ioffe Physicotechnical Institute, Russian Academy of Sciences, St. Petersburg, 194021 Russia

Received September 19, 2000

Abstract—Light-emitting diode structures operating at room temperature were obtained based on a *p*-AlGaAsSb/*n*-InGaAsSb/*n*-AlGaAsSb heterostructure with high Al content in the boundary layers formed on a *p*-GaSb(100) substrate. This structure ensures a threefold increase in the output radiant power and the external quantum yield (~1%) as compared to the known InAsSb/InAsSbP heterostructure grown on an InAs substrate. A considerable increase in the pulsed output radiant power is explained by a more effective confinement of nonequilibrium charge carriers in the active region and by a decrease in the nonradiative recombination level, which is achieved by creating an isoperiodic structure. © *2001 MAIK "Nauka/Interperiodica".*

Introduction. At present, semiconductor radiation sources are used in applied spectroscopy as the elements of sensors determining the presence of some gaseous pollutants in the atmosphere. Strong fundamental absorption bands of several gases that are of considerable practical interest, such as methane CH_4, carbon dioxide CO_2, carbon monoxide CO, and some others, fall within the middle IR range (3.0–5.0 μm). Considerable progress in detecting these gases was provided by the results of investigations performed at the Ioffe Physicotechnical Institute (St. Petersburg), which led to the creation and development of light-emitting diodes (LEDs) based on multicomponent heterostructures of the InAsSbP/InAsSb/InAsSbP type operating at room temperature in the 3–5 μm wavelength interval [1–4].

The next step, which consisted in increasing the efficiency of LED structures of this type, was made in a joint study undertaken by researchers from the Ioffe Physicotechnical Institute and Lancaster University [5]. The gain in the LED efficiency was provided by increasing the purity of material in the active region, which was achieved by doping this region with atoms of rare-earth elements. The resulting LEDs were characterized by a room-temperature pulsed output radiant power exceeding 1 mW.

General disadvantages of the InAsSbP/InAsSb LED structures are as follows: (i) the structure of semiconductor layers is nonisoperiodic with that of InAs substrates; (ii) the barrier height is insufficient for the effective confinement of nonequilibrium charge carriers in the active regions; (iii) the structures exhibit a relatively large absorption; and (iv) the system is characterized by a considerable impact recombination level related to the spin-orbit-split band. Practical application of the known LED structures of this type is limited by an insufficient output power (~1 mW in the pulse mode and ~80 μW in the continuous mode). Taking all these factors into account, we concentrated on the search for new approaches to the creation of high-efficiency LEDs based on new semiconductor materials.

Below, we propose for the first time a new approach to obtaining high-efficiency radiation sources operating in the 3.0–5.0 μm interval. The new LEDs are based on a double-junction heterostructure of the AlGaAsSb/InGaAsSb/AlGaAsSb type grown on a GaSb substrate. The main aim of the investigations in this direction is to provide for an increase in the quantum efficiency and output radiant power by at least one order of magnitude as compared to the known LED structures (based on InAs solid solutions) operating in the same spectral interval. Being the first step in the indicated direction, this study continues our previous investigations devoted to the creation and characterization of LEDs operating in the IR spectral range.

Experimental. The proposed LED heterostructure, grown by liquid phase epitaxy (LPE) on a *p*-GaSb(100) substrate, consists of a four epitaxial layers: *p*-AlGaAsSb/*n*-InGaAsSb/*n*-AlGaAsSb/*n*-GaSb. The composition of the narrow-bandgap layer corresponds to the middle of the aforementioned spectral interval. The *p*-GaSb substrate was not intentionally doped and possessed an equilibrium hole concentration of $(1–2) \times 10^{17}$ cm^{-3}. The wide-bandgap layers of the *n*- and *p*-type were grown so that the concentration of Al would exceed that of Ga; the *p*-type layer was not intentionally doped; the electron conductivity of the *n*-type layer was achieved at the expense of doping with Te. The wide-bandgap layers had a thickness of 1.5 μm.

1063-7850/01/2703-0173$21.00 © 2001 MAIK "Nauka/Interperiodica"

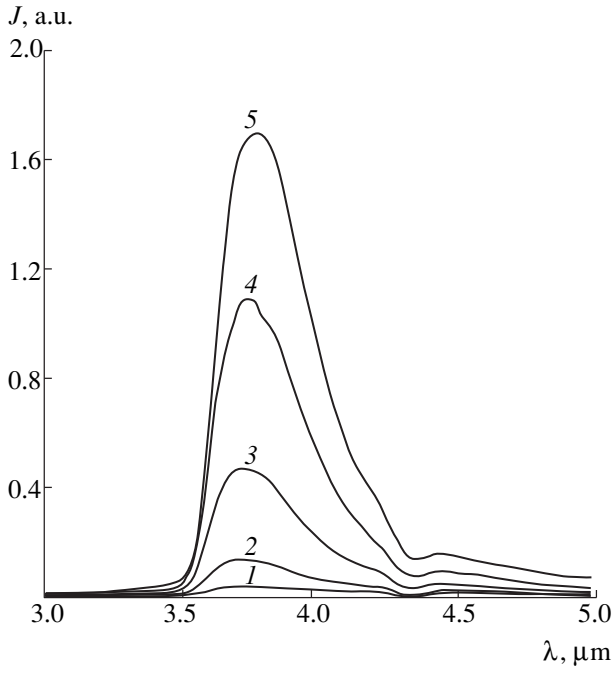

Fig. 1. Typical room-temperature emission spectra of LED 9602 measured for various currents I = 200 (*1*), 300 (*2*), 500 (*3*), 700 (*4*), and 1000 mA (*5*).

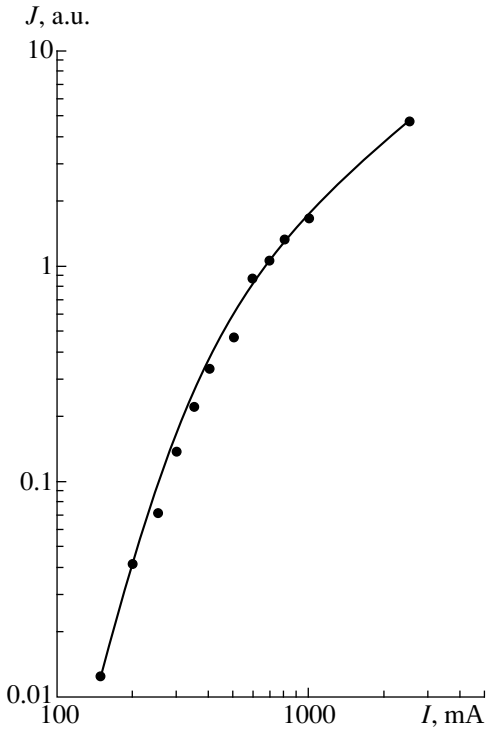

Fig. 2. The plot of room-temperature output radiant power versus current for LED 9602.

The 1.5- to 2-μm-thick narrow-bandgap layer of $In_{0.934}Ga_{0.066}As_{0.83}Sb_{0.17}$ in the active region was also not intentionally doped and had a free electron concentration of about 10^{18} cm^{-3}. The *n*-GaSb contact layer was strongly doped with Te. A distinctive feature of the proposed structure is that it is isoperiodic with the GaSb substrate. The measured relative lattice mismatch $\Delta a/a$ falls within the measurement accuracy limits (2×10^{-4}). A increase in the concentration of Al leads to a greater energy separation of the bands, which provides for the better confinement of nonequilibrium charge carriers in the active region of the structure.

The sample heterostructure was placed into a parallelepiped LED case with parabolic reflector. The square *p–n* junction area had a size of 0.5×0.5 mm; the parallelepiped height was 0.1 mm. The output radiation was emitted predominantly through the parallelepiped side faces in the direction of reflector. The emission spectra were measured upon applying a 20-μs current pulse with an off-duty factor of 49. The dispersive element was a monochromator with a liquid nitrogen cooled InSb photodetector placed at the output slit. The radiant power was measured using a standard Nova instrument equipped with a 2A-SH thermocouple sensor. The sample LED structures were characterized by the spectral and output power characteristics measured using various currents at room temperature.

Results. A typical emission spectrum contains a single band (Fig. 1) with a wavelength at maximum equal to 3.7–3.8 μm. The longwave side of the emission band exhibits a feature at λ = 4.27 μm corresponding to the absorption band of CO_2 present in air. The full width at half maximum (FWHM) of the emission band is 30–35 meV, which is 1.5–2 times smaller as compared to the typical room-temperature FWHM values of usual LEDs. It also should be noted that the shortwave side of the emission band is steeper than the longwave side. The shape of the emission band is virtually independent of the current.

The integral pulsed radiant power P, determined by the main emission band, exhibits a superlinear increase with the current I (Fig. 2). If the P versus I relationship is described by the formula $P \sim I^n$, the exponent n decreases with increasing current: from n = 3 for I = 150 mA to n = 1.2 for I = 2500 mA. The pulsed output power (equal to the average power measured by the Nova instrument multiplied by the off-duty factor) is 3.2 mW for the pulsed current with an amplitude of 1 A, a pulse width of 20 μs, and an off-duty factor of 49. This value correspond to an external quantum emission yield of 1%.

Discussion. As follows from the experimental data presented above, the energy corresponding to the maximum of the emission spectrum for all LEDs is 20–30 meV greater than the room-temperature gap width of the narrow-bandgap material. Therefore, the interband recombination of charge carriers in the LED structures under consideration dominates over the impurity and interface recombination mechanisms. The sloping longwave wing of the emission band is indicative of the presence of a tail of the density of states in

the bandgap. However, the presence of these states does not affect the position of the band maximum.

A considerable difference between the energy corresponding to maximum of the emission band and the gap width is explained by a large equilibrium concentration of electrons in the active region. However, the experimental emission band halfwidth is smaller than the value corresponding to this large carrier concentration, provided that the shortwave radiation absorption in the active region proper is ignored. This absorption can be related to the fact that the radiation emitted in the direction of the parabolic reflector travels through a distance of about several dozen microns in the active region. During this, the shortwave radiation is absorbed due to the interband transitions and then partly reirradiated. The reirradiation favors the superlinear increase in the emission intensity with the current. The main factor responsible for the superlinear growth of the emission intensity at small currents (<0.5 A) is probably the occupation of deep levels. For the currents above 0.5 A (>200 A/cm^2), the deep levels are almost completely occupied. The interval from 0.5 to 2.5 A is characterized by a high external quantum yield (close to 1%). The increase in the LED efficiency is certainly favored by a good confinement of the nonequilibrium charge carriers (holes) in the active region, which is provided by a high Al content in the boundary layers.

The superlinear variation of the radiant power with the current at large values (>1 A) is probably indicative of the absence of a nonradiative CHHS Auger recombination, whereby one hole passes into the spin-orbit-split subband of the valence band and another hole passes into the conduction band. This process is related to a large concentration of Sb (exceeding that of Ga), because Sb increases the spin-orbit-splitting energy in the active region.

Thus, the results of investigation of a new LED heterostructure of the *p*-AlGaAsSb/*n*-InGaAsSb/*n*-AlGaAsSb type with a high Al content in the boundary layers grown on a *p*-GaSb(100) substrate shows evidence of good prospects for the creation and development of high-efficiency LED structures on GaSb substrates possessing narrow emission bands in the 3.4–4.4 μm wavelength interval. The high efficiency of the new LEDs is due to a good matching of the lattice constants between different layers, a considerable barrier height favoring effective confinement of the nonequilibrium charge carriers in the active region, and a low level of the nonradiative Auger recombination (decreased at the expense of increasing spin-orbit-splitting energy in material of the active region). A prototype LED structure of the proposed type showed considerable advantages over the InAsSb/InAsSbP system. The new structure provides for at least a threefold gain in the pulsed radiant power and external quantum yield as compared to usual devices of the InAsSb/InAsSbP type grown on InAs substrates. This result opens principally new possibilities in constructing LEDs operating in the 3.4–4.4 μm wavelength interval.

Acknowledgments. This study was supported by the Russian Foundation for Basic Research, project nos. 99-02-18109 and 00-02-17047.

REFERENCES

1. N. P. Esina, N. V. Zotova, B. A. Matveev, *et al.*, Pis'ma Zh. Tekh. Fiz. **9** (7), 391 (1983) [Sov. Tech. Phys. Lett. **9**, 167 (1983)].
2. B. Matveev, N. Zotova, S. Karandashov, *et al.*, IEE Proc.: Optoelectron. **145** (5), 254 (1998).
3. A. A. Popov, V. V. Sherstnev, Yu. P. Yakovlev, *et al.*, Electron. Lett. **33**, 86 (1997).
4. A. A. Popov, M. V. Stepanov, V. V. Sherstnev, and Yu. P. Yakovlev, Pis'ma Zh. Tekh. Fiz. **24** (15), 34 (1998) [Tech. Phys. Lett. **24**, 596 (1998)].
5. A. Krier, H. H. Gao, V. V. Sherstnev, and Yu. P. Yakovlev, J. Phys. D (2001) (in press).

Translated by P. Pozdeev

Technical Physics Letters, Vol. 27, No. 3, 2001, pp. 176–179. Translated from Pis'ma v Zhurnal Tekhnicheskoĭ Fiziki, Vol. 27, No. 5, 2001, pp. 8–16.

Thin-Film Magnetically Soft Fe–Zr–N Alloys with High Saturation Induction

O. A. Bannykh, E. N. Sheftel', V. E. Zubov, D. E. Kaputkin, A. I. Krikunov, A. D. Kudakov, G. Sh. Usmanova, and T. S. Fedulova

Baikov Institute of Metallurgy, Russian Academy of Sciences, Moscow, 117334 Russia

Received August 8, 2000

Abstract—Thin films of magnetically soft nanocrystalline alloys of the Fe–Zr–N system with a high (1.6–1.8 T) saturation induction and a very low (record) coercive force (4–6 A/m) were obtained by magnetron sputtering followed by thermal treatment of the deposit. Direct magnetooptical observation of the domain motion revealed a high homogeneity of the film material and showed that remagnetization in the material proceeds by mechanism of the domain boundary displacement. *© 2001 MAIK "Nauka/Interperiodica".*

At present, considerable effort is devoted to the development and investigation of magnetically soft materials with a high saturation induction B_s which are employed, in particular, in the high-density magnetic recording devices. Since the maximum saturation induction value (B_s = 2.2 T) was reached in bcc iron, the most promising materials for these applications are offered by α-Fe based alloys. A small coercive force H_c of the magnetic material must be provided by its low magnetic anisotropy and zero magnetostriction λ_s. This can be achieved by forming a nanocrystalline structure (with a grain size on the order of 10 nm), composed of various structural and/or phase components possessing magnetostrictions of the opposite sense [1, 2]. The desired nanocrystalline structure can be formed by annealing thin-film alloys obtained in the initial amorphous state [3].

Previously [4], we developed the general principles of doping for magnetically soft alloys, which provide for the obtaining of materials possessing a combination of excellent magnetic properties in a broad frequency range with high wear resistance. This is achieved by forming a special heterophase structure comprising a magnetic matrix with dispersed particles of most thermodynamically stable and hard interstitial phases such as carbides, nitrides, and oxides of group III–V metals [5].

Below, we report on the results of investigation of a series of thin-film alloys of the Fe–Zr–N system which, owing to the alloying principles employed, must exhibit maximum possible values of the saturation induction together with a high level of thermally stable magnetically soft material properties. Obtained in the form of thin films, these alloys must initially possess an amorphous structure.

The samples of thin-film alloys of the Fe–Zr–N system with variable nitrogen content were obtained by magnetron sputtering of a target with the composition Fe—8 at. % (12.4 wt %) Zr in an Ar + N_2 atmosphere as described in [6]. The content of N_2 in the gas phase was varied from 2.5 to 20% relative to the total working gas pressure (0.66 Pa) in the sputtering chamber. The alloys (see table) were obtained in the form of 0.2- to 5-μm-thick films deposited onto glass substrates. After deposition, the samples were annealed for 1 h at 400 or 550°C under dynamic vacuum conditions (residual pressure about 1 mPa).

The annealed samples were studied by methods of electron-probe microanalysis (EPMA) [6] and X-ray diffraction. The X-ray diffraction measurements were performed using carbonyl iron as the reference. The amorphous structure formation was judged by the presence of a halo in the diffraction patterns. Since the only intense lines in the X-ray diffraction patterns were the {110} reflections due a bcc iron phase, the crystal lattice periods were compared using the values calculated for this single line with an error of ~0.0005 nm.

The static magnetic properties of the samples were studied with the aid of a vibrating magnetometer, using the magnetic fields with a strength of up to 1.2 MA/m perpendicular to the film surface. The quasistatic magnetization curves in weak fields (H = 0.8–160 A/m) were measured by the induction method in a low-frequency (f = 80 Hz) alternating magnetic field. Direct observations of the domain structure, domain boundaries, and their displacements were performed using a magnetooptical micromagnetometer [7] capable of determining the local magnetic properties on the sample surface with a lateral resolution of 0.2 μm. We have measured the magnetooptical equatorial Kerr (MEK) effect expressed as $\delta = (I - I_0)/I_0$, where I and I_0 are the intensities of light reflected from magnetized and nonmagnetized sample surface. Since the δ value is proportional to the sample magnetization, the $\delta(H)$ curve represents essentially the local magnetization of the probed surface area expressed in relative units.

1063-7850/01/2703-0176$21.00 © 2001 MAIK "Nauka/Interperiodica"

The structure (by X-ray diffraction data) and magnetic properties of thin-film Fe–Zr–N alloys

Alloy	Nitrogen content in atmosphere during sputtering, %	Sample state	Structure	Lattice period increment against reference, nm	Physical broadening of {100} line, deg	Saturation induction B_s, T	Coercive field strength H_c, A/m
1	2.5	Initial	bcc	0.0038	0.05	–	–
2	5	Initial	bcc	0.0037	0.15	–	–
3	7.5	Initial	bcc	0.0037	0.38	–	–
4	10	Initial	bcc + amorph.	0.0058	2.61	–	70 ⟶ 1000*
		Anneal 400°C	bcc + amorph.	0.0037	2.03	1.8	5–105*
		Anneal 550°C	bcc + amorph.	0.0019	1.52	–	135 ⟶ 1000*
5	15	Initial	Amorph.	–		–	>500
		Anneal 400°C	bcc + amorph.	0.0032	2.38	1.6	4–6
		Anneal 550°C	bcc + amorph.	0.0014	1.67	–	4–50*
6	20	Initial	Amorph.	–		–	>1000
		Anneal 400°C	bcc + amorph.	0.0042	2.20	2.0	8
		Anneal 550°C	bcc + amorph.	0.0020	1.40	–	96

* Values obtained for films with various thicknesses.

The results of the EPMA measurements showed that the ratio of metal components in the film is close to that in the sputtered target. For a film sputtered in argon, the atomic ratio of iron and zirconium was Fe/Zr = 92.5/7/5 (see table, alloy 1); the Fe/Zr ratios in the samples sputtered in an atmosphere containing 10 and 15% N_2 were 92.4/7.6 (alloy 4) and 91.2/8.8 (alloy 5), respectively.

According to the X-ray diffraction data, alloys 1–3 (see table) in the initial (as-deposited) state contain a single bcc crystal phase representing an α-Fe based solid solution with a lattice period 1.3% greater as compared to that in the pure reference iron sample. This significant increase is probably due to a considerable saturation of the solid solution with nitrogen and zirconium (equilibrium solubilities of N and Zr in α-Fe are 0.4 and 0.1 at. %, respectively [7]).

The increase in width of the X-ray diffraction lines of α-Fe observed in the alloys with increasing nitrogen content (see table) is known to be indicative of a decrease in the α-Fe grain size and an increase in the number of structural defects. As seen from the table, the α-Fe lattice period in all alloys is the same, which implies that equal amounts of elements are dissolved in the solid solutions. Taking this into account, we may suggest that the excess nitrogen present in alloys 2 and 3 is bound to additional defects formed in these alloy structures.

The X-ray data for alloy 4 characterized by a higher nitrogen content show the formation of two phases, crystalline (bcc α-Fe) and amorphous. The lattice period of α-Fe in alloy 4 is considerably greater as compared to that in alloys 1–3, where the amorphous phase is absent. The increase in the lattice period of alloy 4 is most likely due to a more pronounced decrease in the velocity of motion and the rate of annihilation for defects formed during the alloy film deposition. The greater width of reflections observed for the bcc α-Fe phase in alloy 4 as compared to that in alloys 1–3 is evidence of a decrease in the grain size and an increase in the level of stresses in the α-Fe crystal lattice. A further increase in the nitrogen concentration in the samples (alloys 5 and 6) leads to their complete amorphization during deposition.

The annealing of alloys 5 and 6 at 400°C leads to the formation of a bcc crystal phase (see table). The amount of this phase (estimated using the diffraction line intensity) in alloys 4–6 increases when the annealing temperature grows to 550°C. Thermal stability of the amorphous phase increases with the concentration of nitrogen in the alloy. The α-Fe bcc crystal lattice period in all alloys decreases with increasing annealing temperature (see table), which is indicative of a decrease in the concentration of dissolved elements. This is accompanied by a decrease in the concentration of defects in the α-Fe phase (manifested in decreasing stress level, increasing grain size, etc.), which is shown by a decrease in the X-ray refection broadening.

The ratio of widths of the {110} and {220} diffraction lines of the α-Fe phase in alloys 4 and 5 annealed at 550°C is approximately equal to the ratio of secants of their θ angles, which implies that the line broadening is entirely due to a small size of the coherent scattering domains [8]. Estimates of the grain size in these alloys yield 8–10 nm.

The results of magnetic measurements showed that all alloys in the initial (as-deposited) and annealed

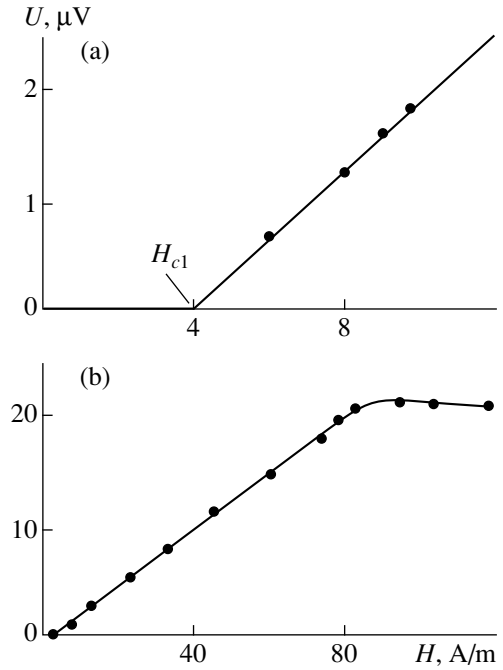

Fig. 1. Magnetization curves for alloy 5 (annealed at 400°C) measured by a compensation method in the region of (a) weak fields and (b) saturation.

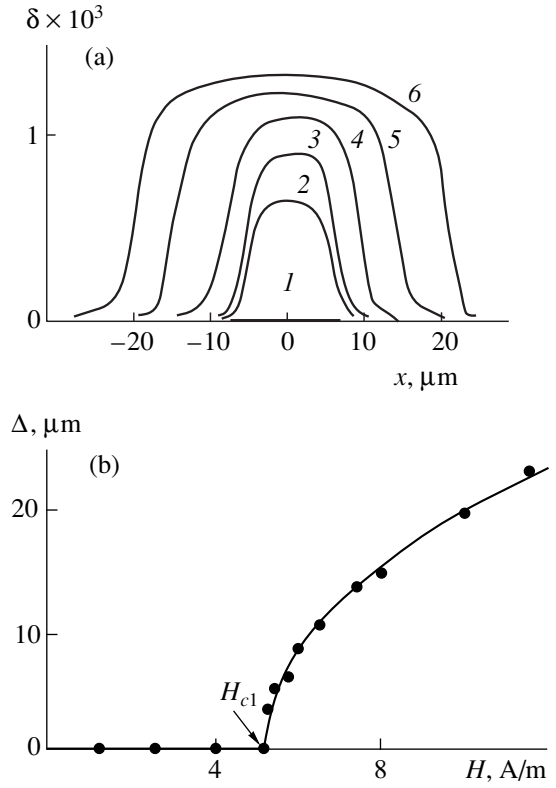

Fig. 2. The plots of (a) magnetooptical equatorial Kerr effect versus coordinate x for alloy 5 (annealed at 400°C) measured at various applied field strengths H = 5.4 (*1*), 5.5 (*2*), 5.7 (*3*), 6 (*4*), 7.5 (*5*), and 10 A/m (*6*) and (b) domain boundary oscillation amplitude Δ on the sample surface versus external magnetic field strength H.

states are ferromagnetic. The films possess a perpendicular magnetic anisotropy, as evidenced by a nonzero magnetization at $H \longrightarrow 0$. This anisotropy is apparently due to mechanical stresses in the film, which can be related either to the film-substrate interaction or to a columnar morphology of crystallites formed in the film during deposition and annealing. In the absence of the perpendicular anisotropy, the magnetization curve measured in a perpendicular field allows the saturation induction B_s to be determined using the formula $B_s = \mu_0 H_s$, where H_s is the saturation field strength. In some cases, the anisotropy can be taken into account by introducing a correction for the anisotropic field strength. The $B_s$values presented in the table were calculated with an allowance for this correction.

The annealing improves the magnetically soft material properties (see table). The best soft magnetic properties were obtained for a sample of alloy 5 annealed at 400°C. Figure 1 shows a plot of the signal U (proportional to the sample magnetization) versus the magnetic field strength. As is seen, the signal intensity is a linear function of the field strength for H below ≈80 A/m (down to ≈6 A/m). Extrapolation of the linear $U(H)$ plot to intersection with the H-axis gives a value (H_{c1}) interpreted as a coercive force of the domain boundaries: it is the displacement of these boundaries that accounts for the sample magnetization. Grounds for this interpretation are provided by the results of the magnetooptical measurements of the displacement of domain boundaries, Bloch lines, and Bloch points in the quasistationary magnetic field. The measurements were performed in model samples representing single-crystalline iron filaments possessing a perfect crystal structure [9, 10].

The behavior of magnetization in some thin-film samples, which was studied as a function of the field strength in the region of weak fields, showed that the magnetization of these alloys proceeds predominantly by displacement of the domain boundaries. The coercive force of these alloys is determined by the coercive force of the domain boundaries. The results of the magnetooptical measurements confirmed that the sample magnetization is related to the displacement of domain boundaries. Figure 2a presents a family of MEK profiles along the coordinate x measured along the sample surface in the direction perpendicular to the domain boundary. The Kerr effect is related to the domain boundary oscillations in the external alternating magnetic field. A decrease in the applied field strength leads to a decrease in amplitude of the domain boundary oscillations and, accordingly, in the size of the region where the MEK effect has a nonzero magnitude (Fig. 2a).

Figure 2b shows a plot of the amplitude of the domain boundary oscillations on the surface versus the field strength for a sample of alloy 5. The amplitude is determined by the size of the region where the MEK effect magnitude is nonzero. The field strength at which the domain boundary ceases to move is equal to the

coercive force of the domain boundary. Investigation of the magnetic topography of this alloy showed that there are three linear domain boundaries parallel to the long side of the sample, which divide the sample into four approximately equal domains. During the sample remagnetization in the applied magnetic field, the behavior of each domain boundary is the same along the whole length, which is evidence that the sample is highly homogeneous.

Thus, there is a good correlation between the values of the coercive force obtained from the bulk magnetization measurements and those estimated using the direct magnetooptical observations of the surface magnetization process. The coercive force values determined by two methods are approximately equal. It is concluded that remagnetization of the films proceeds by mechanism of the grain boundary displacement.

REFERENCES

1. G. Herzer, IEEE Trans. Magn. **26**, 1397 (1990).
2. O. A. Bannykh, E. N. Sheftel', D. E. Kaputkin, *et al.*, in *Abstracts of Papers of the 15th All-Russia School-Seminar "Novel Magnetic Materials for Microelectronics"* (URSS, Moscow, 1996), p. 70.
3. O. Kohmoto, IEEE Trans. Magn. **27** (4), 3640 (1991).
4. E. N. Sheftel', I. R. Polyukhova, and A. S. Mrktumov, Izv. Akad. Nauk SSSR, Met., No. 4, 134 (1986).
5. V. K. Grigorovich and E. N. Sheftel', *Dispersion Hardening of Refractory Metals* (Nauka, Moscow, 1980).
6. O. A. Bannykh, E. N. Sheftel', A. I. Krikunov, *et al.*, Izv. Ross. Akad. Nauk, Met., No. 2, 54 (2000).
7. *Phase Diagrams of Binary Metal Systems: Reference Book*, Ed. by N. P. Lyakishev (Mashinostroenie, Moscow, 1996).
8. S. S. Gorelik, L. N. Rastorguev, and Yu. A. Skakov, *X-ray Diffraction and Electron Optical Analysis* (Metallurgiya, Moscow, 1970).
9. V. E. Zubov, G. S. Krinchik, and S. N. Kuz'menko, Zh. Éksp. Teor. Fiz. **99** (2), 551 (1991) [Sov. Phys. JETP **72**, 307 (1991)].
10. V. E. Zubov, G. S. Krinchik, and A. D. Kudakov, Prib. Tekh. Éksp., No. 3, 206 (1988).

Translated by P. Pozdeev

Technical Physics Letters, Vol. 27, No. 3, 2001, pp. 180–182. Translated from Pis'ma v Zhurnal Tekhnicheskoĭ Fiziki, Vol. 27, No. 5, 2001, pp. 17–23.

One-Dimensional Quantum Transport in Lead Phthalocyanine Nanostructures

N. A. Poklonski, E. F. Kislyakov, D. I. Sagaĭdak, A. I. Siaglo, and G. G. Fedoruk

Belarussian State University, Minsk, Belarus

e-mail: poklonski@phys.bsu.unibel.by

Received October 3, 2000

Abstract—A model of the electron structure of a nanoobject comprising a stack of lead phthalocyanine (PbPc) molecules with stacking faults is proposed. The results of the molecular orbital (MO) calculation indicate that a 0.6*e* charge is transferred from Pb atom to the Pc macrocycle ring and show that the nanostructure can be considered as a metal-filled nanotube. The proposed model provides for the first time a quantitative interpretation of the electric switching effect previously observed in PbPc films. © *2001 MAIK "Nauka/Interperiodica".*

Metallophthalocyanines ($MC_{32}N_8H_{16}$, where M is a metal) constitute a well-studied [1] class of organic substances, which are close analogs of biologically significant porphyrins [2]. Nanostructures composed of lead phthalocyanine (PbPc) molecules, which may form in thin films of this compound, are interesting objects for the study of charge transfer in low-dimensional systems [3].

The PbPc molecule (Fig. 1a) represents a ring macrocycle stabilized by four peripheral benzene rings. The central Pb atom, coordinated to nitrogen atoms of the macrocycle, does not lie (unlike the central atoms in other metallophthalocyanines) in the ring plane, but occurs at a distance of about 0.1 nm from this plane. The PbPc molecules exhibit a funnel shape and may crystallize in a monoclinic phase [4], with the elementary part of this structure comprising a stack of such molecules (Fig. 1b). Separate lead atoms occurring on the axis of this stack are spaced by a distance of a = 0.373 nm, which is only slightly greater than the interatomic distance (0.348 nm) in the bulk metal lead. This atomic chain serves a conducting channel (quantum wire) that accounts for the metal-type conductivity of PbPc [5].

It was experimentally established [6, 7] that polycrystalline PbPc films with a thickness of ≈0.6 μm exhibit the switching effect, whereby the electric conductivity increases by almost eight orders in magnitude when the applied electric field strength reaches a critical value of $\approx 4 \times 10^4$ V/cm. Until now, this phenomenon was not given any quantitative interpretation.

We have theoretically studied the process of charge transfer (electric current) in a nanostructure of PbPc molecules placed between two identical metal electrodes (Fig. 2). Below, we propose a model of the electron structure of this system in which the electric switching effect is explained by migration of a stacking fault in the stack of PbPc molecules.

There are two limiting cases for the process of the charge transfer through the model nanostructure. If the resistance of the wire–electrode contact is markedly greater than the resistance quantum $2e^2/h$ (which corre-

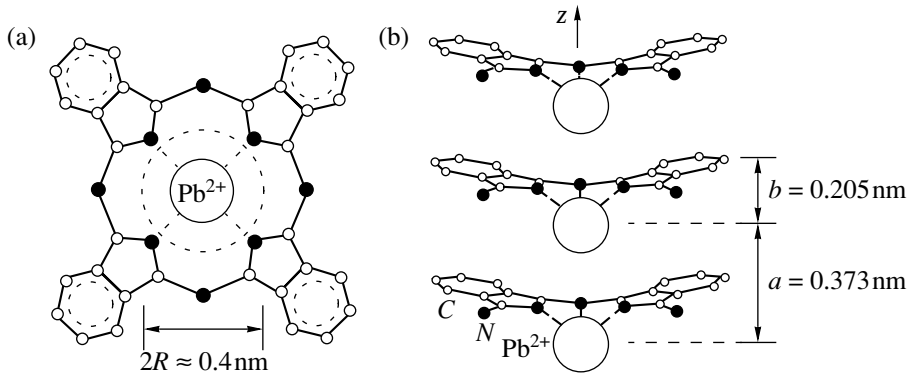

Fig. 1. Schematic diagrams showing (a) the structure of a lead phthalocyanine molecule ($2R \approx 0.4$ nm is the conducting channel diameter) and (b) a nanostructure of stacked PbPc molecules. Hydrogen atoms are not depicted.

1063-7850/01/2703-0180$21.00 © 2001 MAIK "Nauka/Interperiodica"

sponds to a high potential barrier at the boundary and a weak binding of the nanostructure to electrode), the charge transfer proceeds in the regime of the Coulomb blockade [8] or the resonance tunneling [9]. This is a two-stage process: in the first stage, a certain resonance state in the nanostructure is excited; in the second stage, this state exhibits a decay to yield a nonzero average current through the nanostructure for a nonzero potential difference between electrodes. We will consider another limiting case of the charge transfer—the so-called ballistic regime, in which the wire–electrode contact resistance is negligibly small.

The results of calculations of the PbPc molecular structure using a semiempirical molecular orbital (MO) method [10] (MOPAC 7.0 program package; PM3 parametrization) showed a considerable (–0.6*e*, where *e* is the electron charge modulus) charge transfer from Pb atom to the Pc macrocycle ring. The stack of PbPc molecules under consideration has a conducting channel radius of $R \approx 0.2$ nm (Fig. 1) and is similar to the previously studied carbon nanotube filled with an alkali metal [11]. The estimates analogous to those made in [11] showed that a system with this radius exhibits (in the approximation of noninteracting electrons) a single discrete level (miniband) of transverse electron motion inside the nanotube.

Since the stack of PbPc molecules is a one-dimensional quantum system, we may calculate the dc conductivity σ of this model using the Landauer formula for the single-channel conductivity at zero temperature [12]:

$$\sigma = \frac{2e^2}{h}T(E_F) = \frac{T(E_F)}{12.9\ \text{k}\Omega}, \qquad (1)$$

where $T(E_F)$ is the transmission coefficient of the stack for electrons with a kinetic energy equal to the Fermi energy E_F.

Let us consider a model nanostructure with a single stacking fault (Fig. 2a). The stacking fault is a cavity between two macrocycle rings of PbPc molecules, which contains no Pb atom. This defect has a length *d* determined by the nanostructure period *a* and the thickness *b* of the PbPc molecule. Taking into account the lead ion (Pb^{2+}) radius equal to 0.126 nm [13], the length of the stacking fault is $d = a + 2b - 2 \times 0.126$ nm = 0.531 nm.

In order to calculate the coefficient $T(E_F)$ of the electron transmission through the nanostructure, let us determine the height of the potential barrier U_0 created by the stacking fault. We will assume that the positive charge is uniformly distributed in the cross section inside the nanotube (conducting channel) in the regions far from the stacking fault. According to the results of our quantum-chemical calculations, the linear density of the negative charge on the surface of the channel is $\chi = -0.6e/a < 0$. This charge distribution corresponds to

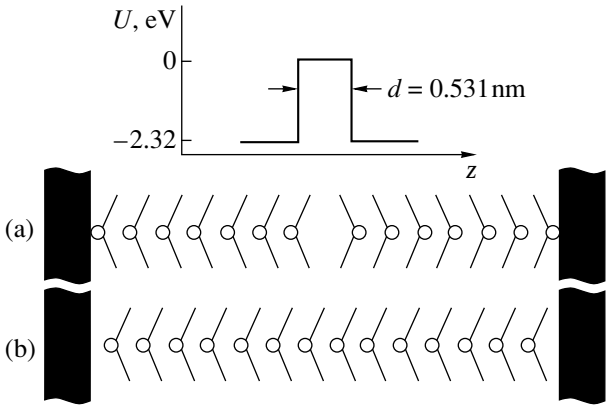

Fig. 2. Schematic diagrams showing a stack of PbPc molecules between two identical metal electrodes: (*a*) model with a stacking fault ("off" state); (*b*) model without defect ("on" state). $U(z)$ is the potential energy of a conduction electron in the system.

a parabolic dependence of the electrostatic potential φ on the distance *r* from the nanotube axis [14]:

$$\varphi = \frac{\chi}{4\pi\varepsilon_0}\left(\frac{r^2}{R^2} - 1\right), \qquad (2)$$

where ε_0 is the dielectric constant and *R* is the nanotube radius. According to formula (2), the potential at the point on the nanotube axis far from the stacking fault is $\varphi_0 = 0.6e/4\pi\varepsilon_0 a = 2.32$ V; since the nanotube as a whole is electrically neutral, the potential outside the channel is $\varphi(r \geq R) = 0$.

Since there are no electrons in the equilibrium state at the site of the stacking fault (cavity), the potential φ at the cavity center is assumed to be zero. Thus, the electron potential energy $U(z)$ varies along the nanotube axis from $-e\varphi_0$ (at a point far from the stacking fault) to zero inside the defect cavity (Fig. 2). Therefore, the conduction electrons meet a barrier with a height of $U_0 = e\varphi_0$ at the site of the stacking fault.

The Fermi energy of a one-dimensional electron system with a single miniband of transverse motion at zero temperature is [15]

$$E_F = \frac{\pi^2\hbar^2 n^2}{8m}, \qquad (3)$$

where *n* is the one-dimensional electron concentration, *m* is the longitudinal effective mass of a conduction electron inside the nanotube, and $\hbar = h/2\pi$ is the Planck constant. The atom of lead has four valence electrons, two of which occupy the first Brillouin zone (see [15]). In the second Brillouin zone, there are on average 1.4 electrons per Pb atom because 0.6 electron charge per atom are transferred to the nanotube surface. Thus, the one-dimensional electron concentration in the nanotube is $n = 1.4/a = 3.75 \times 10^9$ m^{-1}. For $m > 0.6m_0$ (m_0 is the rest mass of free electron), we obtain $E_F < U_0$.

We will approximate a stacking fault in the stack of PbPc molecules by a rectangular potential barrier with a width of $d = 0.531$ nm and a height $U_0 = 2.32$ eV. For the rectangular barrier, the transmission coefficient $T(E)$ for an electron with the kinetic energy $E < U_0$ is [16]

$$T(E) = \frac{4k_1^2k_2^2}{(k_1^2 + k_2^2)^2 \sinh^2(k_2 d) + 4k_1^2k_2^2}, \qquad (4)$$

where $k_1 = \hbar^{-1}\sqrt{2mE}$ and $k_2 = \hbar^{-1}\sqrt{2m(U_0 - E)}$. If the nanotube (i.e., the stack of PbPc molecules) contains no stacking faults, the potential φ is constant along the axis, the conduction electrons meet no potential barriers, and $T(E_F) = 1$.

The only free parameter in the proposed model is the effective mass m of conduction electrons. For $m \approx 5.7m_0$, Eqs. (3) and (4) indicate that a transition from the state with a singe stacking fault to the state without defects (Fig. 2) increases the transmission coefficient $T(E_F)$ from 10^{-8} to 1. This change is what accounts for an increase in the electric conductivity of PbPc by eight orders of magnitude reported in [6]. The large value of the effective electron mass is consistent with the notions about the conduction-electron-induced polarization of the phthalocyanine macrocycle ring, which may result in a one-dimensional quantum polaron formation [17]. Since the Fermi energy in our case is $E_F \approx 232$ meV, while the measurements reported in [6, 7] were performed at room temperature (corresponding to a thermal energy of ≈26 meV), the estimates provided by formula (1) remain essentially valid.

The results of our quantum-chemical MO calculations for PbPc molecules, which agree both with the estimates obtained by other researchers [6, 7] and with the experimental data [18], show that the barrier for the Pb^{2+} ion tunneling through the macrocycle ring of PbPc amounts to 2 eV, which corresponds to the critical field strength for the electrostatic switching effect [6, 7]. At a potential difference of 2 V between the electrodes, Pb^{2+} ions readily pass through the phthalocyanine ring. This is equivalent to the defect migration in the stack of PbPc molecules. When the stacking fault reaches the opposite electrode and disappears, the coefficient of electron transmission through the structure increases in a jumplike manner by eight orders of magnitude.

REFERENCES

1. *Phthalocyanines: Properties and Applications*, Ed. by C. C. Leznoff and A. B. P. Lever (VCH, New York, 1989–1996), Vols. 1–4.
2. *The Porphyrin Handbook*, Ed. by K. M. Kadish, K. M. Smith, and R. Guilard (Academic, San Diego, 2000), Vols. 1–10.
3. S. Roth, S. Blumentritt, M. Burghard, *et al.*, Synth. Met. **94** (1), 105 (1998).
4. K. Ukei, Acta Crystallogr., Sect. B: Struct. Crystallogr. Cryst. Chem. **B29** (11), 2290 (1973).
5. K. Ukei, K. Takamoto, and E. Kanda, Phys. Lett. A **45** (4), 345 (1973).
6. C. Hamann, H.-J. Höhne, F. Kersten, *et al.*, Phys. Status Solidi B **50** (1), K189 (1978).
7. Th. Frauenheim, C. Hamann, and M. Müller, Phys. Status Solidi A **86** (2), 735 (1984).
8. D. V. Averin and K. K. Likharev, J. Low Temp. Phys. **62** (3/4), 345 (1986).
9. *Tunneling Phenomena in Solids*, Ed. by E. Burstein and S. Lundquist (Plenum, New York, 1969; Mir, Moscow, 1973).
10. J. J. P. Stewart, J. Comput. Chem. **10** (2), 209 (1989).
11. N. A. Poklonski, E. F. Kislyakov, G. G. Fedoruk, and S. A. Vyrko, Fiz. Tverd. Tela (St. Petersburg) **42** (10), 1911 (2000) [Phys. Solid State **42**, 1966 (2000)].
12. J. T. Londergan, J. P. Carini, and D. P. Murdock, *Binding and Scattering in Two-Dimensional Systems: Applications to Quantum Wires, Waveguides and Photonic Crystals* (Springer-Verlag, Berlin, 1999).
13. *Physical Quantities: Handbook*, Ed. by I. S. Grigor'ev and E. Z. Meĭlikhov (Énergoatomizdat, Moscow, 1991), p. 235.
14. V. V. Batygin and I. N. Toptygin, *Problems in Electrodynamics* (Nauka, Moscow, 1970; Academic, London, 1964).
15. S. Kagoshima, H. Nagasawa, and T. Sambongi, *One-Dimensional Conductors* (Springer-Verlag, Berlin, 1988).
16. L. D. Landau and E. M. Lifshitz, *Course of Theoretical Physics*, Vol. 3: *Quantum Mechanics: Non-Relativistic Theory* (Nauka, Moscow, 1989, 4th ed.; Pergamon, New York, 1977, 3rd ed.).
17. A. O. Gogolin and A. S. Ioselevich, Pis'ma Zh. Éksp. Teor. Fiz. **53** (9), 456 (1991) [JETP Lett. **53**, 479 (1991)].
18. R. Strohmaier, C. Ludwig, J. Petersen, *et al.*, J. Vac. Sci. Technol. B **14** (2), 1079 (1996).

Translated by P. Pozdeev

Technical Physics Letters, Vol. 27, No. 3, 2001, pp. 183–186. Translated from Pis'ma v Zhurnal Tekhnicheskoĭ Fiziki, Vol. 27, No. 5, 2001, pp. 24–31.

The Recombination Instability of Current in a Nonlinear Regime in Gold-Compensated Germanium

I. K. Kamilov, N. S. Abakarova, Kh. O. Ibragimov, and K. M. Aliev

Institute of Physics, Dagestan Scientific Center, Russian Academy of Sciences, Makhachkala, Dagestan, Russia

e-mail: kamilov@datacom.ru

Received August 30, 2000

Abstract—We report on the first results of the experimental verification of a theoretical one-dimensional model describing the recombination instability of current in gold-compensated germanium in a two-parametric space. The experiment revealed various regimes of the system functioning in the voltage–emission parameter space, the formation of subdomains, and the order–disorder transitions via intermittency or by a nonstandard evolution scenario. © *2001 MAIK "Nauka/Interperiodica".*

This study was devoted to experimental verification of the one-dimensional theoretical model of Oshio and Yahata [1, 2] developed for a gold-doped *n*-Ge, according to which the recombination instability in the semiconductor exposed to a strong electric field leads to the current instability development and gives rise to the current oscillations. The model allows for the formation of a high-field domain in the system and takes into account both temporal and spatial evolution of this domain related to variation of the applied voltage V and the electron emission coefficient β (i.e., in the voltage–emission space of parameters). Depending on a particular region in this two-parametric space, the system exhibits three various regimes of functioning (ohmic, quenched, and transit-time modes), features the formation of subdomains, and exhibits some other new properties not observed in typical nonlinear systems. The same properties can be manifested in a nonlinear regime in the Gunn effect (having very important applications in semiconductor devices) [3, 4], since the initial model equations are very much alike.

The recombination instability of current was originally reported by Stafeev [5], Konstantinov *et al.* [6, 7], Bonch-Bruevich [8], Karpova and Kalashnikov [9] and studied in sufficient detail in a typical linear system, represented by the cold-compensated *n*-Ge, in the 16–35 K temperature interval. A number of papers were devoted to the study of this instability in other materials doped with Ni and Mn [9–14].

We have observed for the first time the recombination instability of current in *p*-Ge(Au) at 77 K and thoroughly studied the one-dimensional theoretical model proposed in [1, 2] in a wide region of the two-parametric space (V, β). The experiments were conducted at 77 K using a voltage-controlled pulsed regime with the pulse duration of up to 500 μs. Based on the measured current–voltage (I–V) characteristics and time series of the current oscillations, we constructed the corresponding phase portraits, bifurcation diagrams, and power spectra. Data on the time series of the current oscillations were fed into a computer upon digitization with an analog-to-digital (ADC) converter operated at a sampling frequency of up to 200 MHz. The automated experimental setup allowed the control parameters to be smoothly varied in a wide region of the two-parametric space. The emission coefficient was varied by exposure of the sample to a 100-W incandescent lamp and/or by the nonequilibrium charge carrier injection via contacts.

The samples were prepared using *p*-Ge doped with antimony and compensated with gold. The material had a deep-level impurity concentration of 2×10^{15} cm^{-3}, a carrier mobility of 7×10^3 cm^2/(V s), and a resistivity of 2.8×10^5 Ω cm at 77 K. The samples were cut in the form of rectangular bars with a length of 3–8 mm and a 1-mm^2 cross section. A good injection of nonequilibrium carriers was provided by the indium–gallium (In–0.5% Ga) and tin–antimony (Sn–7% Sb) contacts deposited onto opposite edges of the samples.

Depending on the emission coefficient, the I–V curves exhibited ohmic or superlinear initial regions, followed either by the current saturation or by the N-shape behavior with current oscillations of large amplitude and the current pulse modulation coefficient of up to 90%. An increase in the applied voltage led either to a sharp growth in the current or to the S-shape current–voltage characteristic. Figure 1 shows a typical I–V curve observed for a light-induced nonequilibrium carrier production. The current oscillations observed in the sample can be explained according to theory and experiment [6–14] by the periodic appearance, motion, and degradation of a high-electric-field domain at the contact. Investigation of the field strength distribution along the sample showed that in *p*-Ge(Au), in contrast to *n*-Ge(Au), the high-field domain is always formed at the anode and moves toward the cathode. The electric

1063-7850/01/2703-0183$21.00

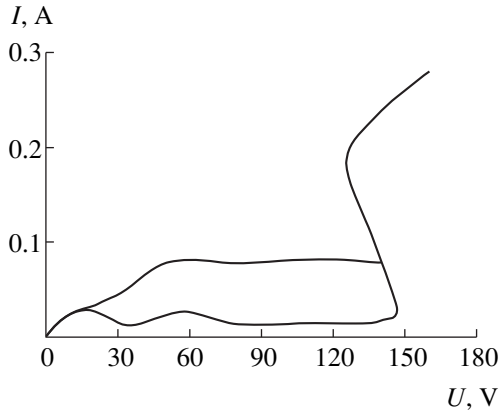

Fig. 1. Current–voltage characteristic of a *p*-Ge(Au) sample measured at 77 K.

field strength at the anode reached up to 2.8 kV/cm, while the mean field strength in the sample was 300 V/cm.

Figure 2 shows the time series of current oscillations, phase portraits, and power spectra measured at a preset illumination level and various applied voltages (significant from the standpoint of comparison with the theoretical model) The situation depicted in Fig. 2(*1*) corresponds a large emission coefficient β, whereby the appearing domain cannot retain its shape, ceases to grow, and vanishes before reaching the cathode. According to the model [1], the residual domain starts growing again and the cycle is repeated. This high-frequency mode is referred to as "quenched" (although, in our opinion, the term "pulsating" would be more adequate to the real situation observed).

The transition from quenched to transit-time mode proceeded, depending on the control parameters, by two pathways. The first is via intermittency, whereby the amplitude of small quenched-mode oscillations either (i) slowly increases to be followed by a sudden appearance of a peak with large amplitude or (ii) decreases and the oscillations become less regular, while the peaks of large amplitude arise more frequently. The laminar phase of intermittency was represented by the quenched-mode oscillations, while the turbulent outbursts represented the transit-time oscillation mode. On the second pathway, realized for certain values of the parameters, the system exhibited a jumplike change in the spatial wave structure as depicted in Fig. 2(*2*). Note that the transverse Hall probes situated near the middle of the sample at a distance of 3 mm from both the cathode and anode detected no quenched-mode oscillations, while any peak of large amplitude (corresponding to a turbulent outburst) appeared synchronously with the current oscillations.

As the applied voltage was increased, the traveling domain grew to a size that was sufficiently large to provide for the domain survival until reaching the cathode. In this case, the system featured an oscillatory behavior with a frequency determined by the time required for the domain to travel from anode to cathode as depicted in Fig. 2(*3*). In the theoretical model [1], this situation is referred to as the transit-time mode of the traveling domains. In addition, the model stipulates the appearance of subdomains provided that the system parameters are selected appropriately. Figure 2(*4*–*6*) illustrates the cases when one, two, three, and more subdomains appear in the system. The frequency of appearance of fundamental domains decreases and the gaps between these domains are filled with subdomains, which is accompanied by an increase in noise component intensity. We have registered the cases when the number of subdomains in a sample exhibited a change, while the system parameters during the measurement were maintained constant, as depicted in Fig. 2(*6*).

The further increase in the applied voltage resulted in a jumplike transition leading to self-organization in the system, whereby the sample again displayed a one-domain behavior as depicted in Fig. 2(*7*). The main peak of the newly appearing one-domain mode always had a frequency exceeding that of the preceding one-domain mode. This was related to an increase in the domain velocity, which was due to the carrier drift velocity growing with the applied voltage. For a given level of illumination intensity, we have observed three sequential order–disorder transitions in the entire range of applied voltages (up to the *S*-switching point).

For intermediate values of the parameters in the parametric space region studied, the system exhibited chaotic states corresponding to intermittency, probably, due to the interaction of various oscillation modes. The formation of subdomains and the corresponding oscillations with the relative periods 2, 3, 4, 6, and 8 do not obey the known standard scenarios for transition to a chaotic state (such as the Feigenbaum period doubling [15]) and cannot be explained in terms of the corresponding universal operators and constants typical of the usual deterministic chaos. However, when the system left the chaotic state and passed to self-organization, it was possible to observe a reverse cascade of period-doubling bifurcations using a very fine adjustment of the system parameters within a certain region of the parametric space.

The so-called "ohmic" model regime [1] could be experimentally observed in two cases: first, for a very high rate of nonequilibrium charge carrier production by illumination or injection and, second, when the electric field strength (at a given rate of the nonequilibrium charge carrier production) was insufficient to ensure that the trapping on deep levels would prevail over the emission process. An analysis of the experimental data indicated that a preset regime of the system functioning (e.g., in a two-domain mode) can be maintained within a rather large region of the parametric space, provided that both the illumination intensity and the applied electric field strength are increased simultaneously. Immediately before the *S*-switching (catastrophe point)

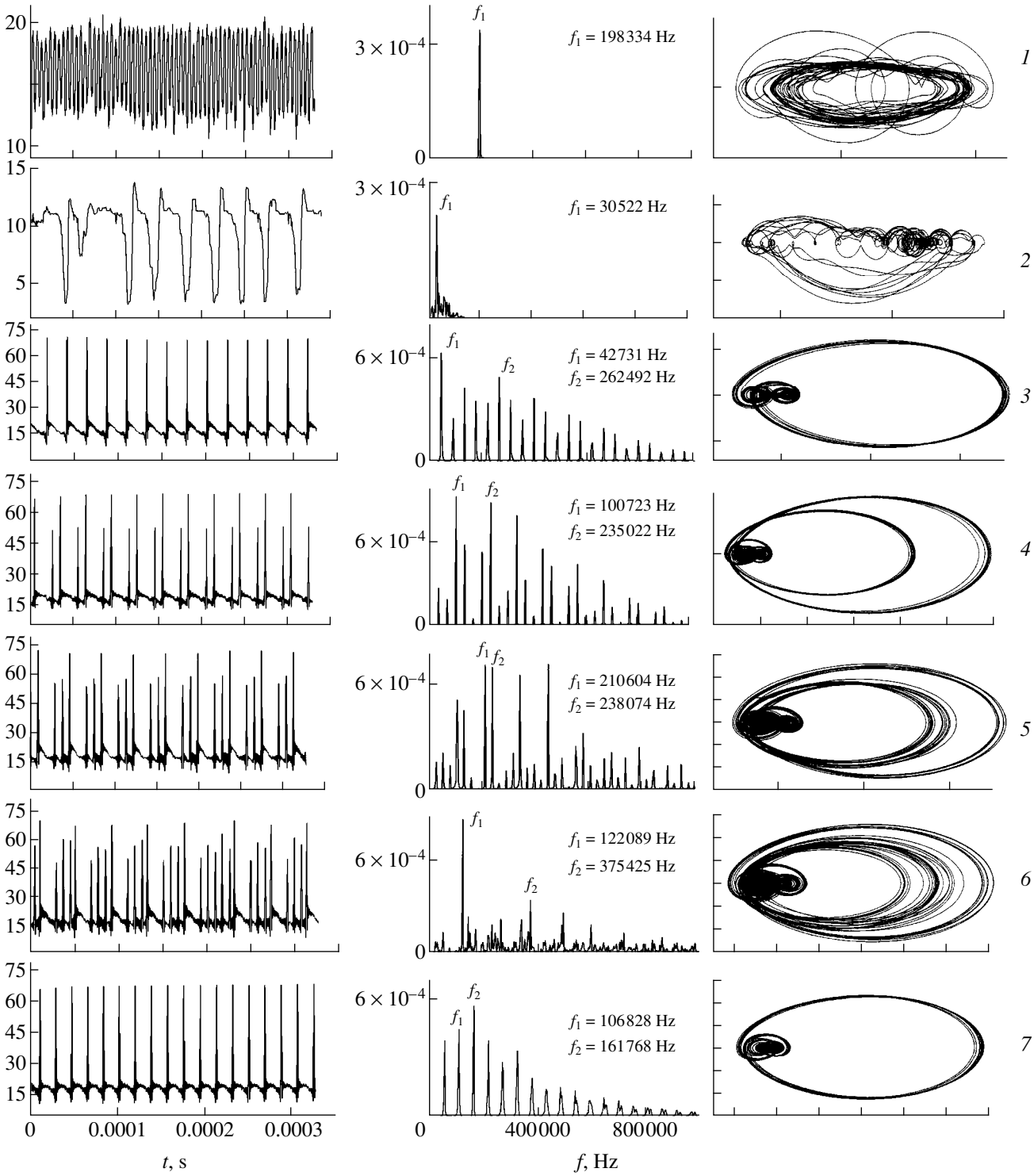

Fig. 2. The patterns of current oscillations in a *p*-Ge(Au) sample and the corresponding power spectra and phase portraits (first to third columns, respectively) measured for various values of the applied voltage (V): (*1*) 16; (*2*) 20; (*3*) 98; (*4*) 105; (*5*) 120; (*6*) 140; (*7*) 142.

the sample exhibited disordered domain formation, which resembled the intermittency phenomena observed in usual determinate systems. The lifetime and number of domains in the system prior to switching are hardly controllable and extremely sensitive to changes in both the electric field strength and the emission coefficient.

In conclusion, it should be noted that the experimental data for *p*-Ge(Au) presented above completely confirm the theoretical model developed by Oshio and

Yahata [1]. We observed three regimes of the system functioning, corresponding to the ohmic, quenched, and transit-time modes of the current oscillation. It was established that the system features one, two, and more subdomain states and exhibits several order–disorder transitions, which proceed via intermittency or by a nonstandard scenario of transition to chaos.

Acknowledgments. This study was supported by the Russian Foundation for Basic Research, project no. 00-02-17329.

REFERENCES

1. K. Oshio and H. Yahata, J. Phys. Soc. Jpn. **65** (5), 1490 (1996).
2. K. Oshio and H. Yahata, J. Phys. Soc. Jpn. **67** (7), 2538 (1998).
3. K. Oshio and H. Yahata, J. Phys. Soc. Jpn. **62** (10), 3639 (1993).
4. K. Oshio and H. Yahata, J. Phys. Soc. Jpn. **64** (5), 1823 (1995).
5. V. I. Stafeev, Fiz. Tverd. Tela (Leningrad) **5** (11), 3095 (1963) [Sov. Phys. Solid State **5**, 2267 (1964)].
6. O. V. Konstantinov and V. I. Perel', Fiz. Tverd. Tela (Leningrad) **6** (11), 3364 (1964) [Sov. Phys. Solid State **6**, 2691 (1965)].
7. O. V. Konstantinov and G. V. Tsarenkov, Fiz. Tverd. Tela (Leningrad) **8** (6), 1867 (1966) [Sov. Phys. Solid State **8**, 1479 (1966)].
8. V. L. Bonch-Bruevich, Fiz. Tverd. Tela (Leningrad) **8** (6), 1753 (1966) [Sov. Phys. Solid State **8**, 1397 (1966)].
9. I. V. Karpova and S. G. Kalashnikov, Pis'ma Zh. Éksp. Teor. Fiz. **6** (12), 954 (1967) [JETP Lett. **6**, 369 (1967)].
10. I. A. Kurova and M. Vrana, Fiz. Tekh. Poluprovodn. (Leningrad) **1** (7), 1095 (1967) [Sov. Phys. Semicond. **1**, 917 (1968)].
11. B. K. Ridley and R. G. Pratt, J. Phys. Chem. Solids **26** (1), 21 (1965).
12. I. V. Varlamov, V. V. Osipov, É. A. Poltoratskiĭ, and A. E. Rzhanov, Fiz. Tekh. Poluprovodn. (Leningrad) **4** (11), 2195 (1970) [Sov. Phys. Semicond. **4**, 1885 (1970)].
13. I. V. Karpova, V. A. Sablikov, and S. M. Syrovegin, Fiz. Tekh. Poluprovodn. (Leningrad) **2** (4), 609 (1968) [Sov. Phys. Semicond. **2**, 509 (1968)]; Fiz. Tekh. Poluprovodn. (Leningrad) **16** (9), 1601 (1982) [Sov. Phys. Semicond. **16**, 1023 (1982)].
14. S. Bumeliene, J. Požela, and A. Tamaševičius, Phys. Status Solidi B **134**, K71 (1986).
15. M. J. Feigenbaum, Los Alamos Sci. **1** (1), 4 (1980).

Translated by P. Pozdeev

Technical Physics Letters, Vol. 27, No. 3, 2001, pp. 187–188. Translated from Pis'ma v Zhurnal Tekhnicheskoĭ Fiziki, Vol. 27, No. 5, 2001, pp. 32–35.

The Effect of Mechanical Activation on the Exoelectron Emission Properties of Activated Charcoal

V. A. Klyuev, O. A. Kutuzova, E. S. Revina, and Yu. P. Toporov

Institute of Physical Chemistry, Russian Academy of Sciences, Moscow, 117071 Russia

Received September 21, 2000

Abstract—The results of experiments indicate that the mechanical activation of a material leads to an increase in the total exoelectron emission current and in the number of emission peaks excited by heating the activated sample. © *2001 MAIK "Nauka/Interperiodica".*

In recent years, the mechanochemical treatments (including mechanical activation) of materials find increasing application as a method of modification of their properties [1, 2]. Here, directed modification of the properties is possible only provided that optimum regimes and durations of the mechanical activation process are selected [3].

However, selecting the optimum regimes is complicated by difficulties in estimating the degree of activation of a given material. As is known [4, 5], the mechanical activation (MA) of a material results from accumulation of various defects in the material structure. Boldyrev [5] emphasized the importance of studying defects in mechanically activated materials because "it is the defect formation, rather than dispersion and the related appearance of new surfaces, that is the main factor accounting for a change in the reactivity of solids" [upon the mechanical activation]. Presently, the MA-induced defects are studied by a number of methods. In particular, disorders in the crystal lattice are determined by X-ray diffraction. The other widely used techniques include IR, RF, NMR, EPR, and Mössbauer spectroscopies [5]. Unfortunately, application of these methods is frequently restricted by the complexity of the instrumentation employed.

The purpose of this study was to assess the possibility of estimating the degree of mechanical activation using the exoelectron emission technique. To this end, we have studied the influence of MA on the parameters of thermostimulated exoelectron emission.

Experimental part. The experiments were performed with activated charcoal (AC) of the FAS-2 type prepared from furfurol. This choice is explained by the fact that the effects of MA upon the adsorption properties and microporous structure of AC are thoroughly studied [6].

The MA processing of AC samples was effected in a planetary-centrifuge activator of the FGO-2U type with steel balls (ShKh-15 grade stainless steel; ball diameter, 8 mm). The specific energy deposition in the MA process was ~5 kW/m^3. The activator is designed so that the drum with a material is immersed into flowing water with a temperature maintained by a thermostat at 10°C. For comparison, we studied both on the activated charcoal samples and the same charcoal crushed manually in an a agate mortar; the latter sample was considered as initial (nonactivated). The exoemission measurements were performed on tablets pressed from the initial and activated charcoal powders.

The thermostimulated exoelectron emission (TSEE) was measured by a conventional method, with the electrons detected by a channeltron (KEU) operating in the single pulse count mode. The AC samples in the form of tablets with a diameter of 10 mm and a thickness of 2 mm were preactivated by exposure to a corona-discharge plasma in air. The curves of the TSEE current versus sample temperature (TSEE spectra or "glow curves") were measured in a vacuum of 10^{-4} Torr at a constant sample heating rate of 10 K/min.

Results. The results of investigation of the TSEE from the initial and activated (MA-processed for 10 min) AC samples are presented in the figure. As seen, the TSEE spectrum of a nonactivated FAS-2 sample exhibits a single emission peak at 215°C with a

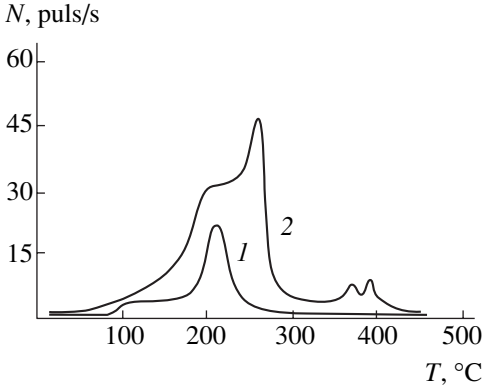

Typical spectra of the thermostimulated exoelectron emission from a charcoal of the FAS-2 type measured in the (*1*) initial state and (*2*) mechanically activated state.

small rise beginning at 100°C. The glow curve of the MA-processed sample is more complicated: the peak at 215°C is complemented by a greater peak at 260°C and two smaller peaks at 375 and 385°C. Note a sharp increase both in the peak amplitude and in the total emission current.

As is known [7], the number of peaks in the TSEE glow curve corresponds to the number of various types of the electron emission centers (i.e., of the defect types), the peak amplitude being proportional to the relative concentration of the corresponding centers (defects). Therefore, a comparison of the curves depicted in the figure clearly demonstrates that MA leads to an increase in the concentration of defects present in the initial state and to the appearance of defects of a new type.

It should be noted that previous investigations of the effect of MA on the properties of FAS-2 [6] showed that a 10-min processing results in a stable change in the adsorption properties, which is related to modification of the existing defect structure and the formation of additional adsorption centers (leading, in particular, to a increase in the water vapor adsorption at low relative pressures). Therefore, the results of our TSEE measurements are completely consistent with the data obtained previously [6] by the adsorption and X-ray diffraction techniques.

Thus, the experimental data obtained indicate that the TSEE method can be very useful and informative in evaluating the degree of mechanical activation of a solid and determining the optimum activation regimes.

REFERENCES

1. E. G. Avvakumov, *Mechanical Methods of Activation of Chemical Processes* (Nauka, Novosibirsk, 1986).
2. V. V. Boldyrev, *Mechanochemical Synthesis in Inorganic Chemistry* (Nauka, Novosibirsk, 1991), pp. 3–32.
3. T. M. Khrenkova, *Mechanochemical Activation of Coals* (Nedra, Moscow, 1993).
4. P. Yu. Butyagin, Usp. Khim. **37**, 898 (1968); **40**, 1935 (1972).
5. V. V. Boldyrev, *Experimental Methods in Mechanochemistry of Solid Inorganic Substances* (Nauka, Novosibirsk, 1983).
6. R. Sh. Vartapetyan, A. M. Voloshchuk, G. M. Plavnik, *et al.*, Zh. Fiz. Khim. **69** (10), 1831 (1995).
7. V. S. Kortov, F. I. Slesarev, and V. V. Rogov, *Exoelectron Control of the Surface Finish of Articles upon Processing* (Naukova Dumka, Kiev, 1986).

Translated by P. Pozdeev

Technical Physics Letters, Vol. 27, No. 3, 2001, pp. 189–192. Translated from Pis'ma v Zhurnal Tekhnicheskoĭ Fiziki, Vol. 27, No. 5, 2001, pp. 36–41.

The Polymorphism of Niobium Pentoxide and the Properties of Alkali Metal Niobates for Ferroelectric Piezoceramics

E. M. Kuznetsova, L. A. Reznichenko, O. N. Razumovskaya, and L. A. Shilkina

Institute of Physics, Rostov State University, Rostov-on-Don, Russia

e-mail: esmit@krinc.ru

Received September 20, 2000

Abstract—The polymorphous modifications of niobium pentoxide used in the synthesis of alkali metal niobate powders and ceramics markedly affect the properties of the final products. It is demonstrated that the transition of Nb_2O_5 from two-phase to single-phase state upon a thermal treatment results in a shift of the phase equilibria in the Nb_2O_5-based solid solutions, which acquire a more perfect crystal structure and exhibit an extremal variation of their electrical properties. These results should be taken into account in the synthesis and development of new ferroelectric piezoceramics for practical applications. *© 2001 MAIK "Nauka/Interperiodica".*

Ferroelectric piezoceramics (FPCs) based on alkali metal niobates possess a unique combination of physical properties, which accounts for their wide use in quantum electronics, electrooptics, microwave piezotechnology, etc. [1]. The base component for these materials is niobium pentoxide Nb_2O_5. Commercial Nb_2O_5 always has a multiphase structure, with the dominating component representing the α_1 modification. Neither the percentage phase composition nor the parameters of coexisting phases are restricted by the existing State Standard for niobium pentoxide, so that these characteristics of Nb_2O_5 vary from one batch to another even for the material obtained from the same source. This instability of the crystalline structure of Nb_2O_5 certainly affects the final properties of FPCs and reduces their reproducibility in the case of large-scale production.

With a view to establishing a relationship between the properties of niobate-based FPCs and the polymorphous state of Nb_2O_5, we have studied the samples of three commercial batches of this compound, as well as the powdered solid solutions of alkali metal niobates and ceramics synthesized using Nb_2O_5 from these batches.

The three batches of Nb_2O_5 (commercial "NBO-PT" grade) selected for these experiments were characterized (according to the results of our X-ray diffraction measurements) by the η phase content reaching 65% (batch 47), 80% (batch 70), and 85% (batch 48) relative to the main α_1 phase.[1] The original experimental data on the X-ray diffraction determination of the phase composition of initial (non-heat-treated) Nb_2O_5 samples are presented in the table. These data show a good agreement with the lattice parameters reported for α_1- and η-Nb_2O_5 [2]. Taking into account that the α_1 modification is stable in the 1000–1400°C temperature interval, we may suggest that η phase represents a low-temperature modification of Nb_2O_5.

In order to exclude the effect of the η-Nb_2O_5 phase on the properties of FPCs, we annealed the samples of all batches at various temperatures T_a in the interval from 950 to 1250°C. It was found that an increase in T_a led to a decrease in the content of η phase until its complete vanishing upon the annealing at 1120°C (batch 70), 1150°C (batch 48), and 1170°C (batch 47). Heat-treated above 1180°C, the samples of all three Nb_2O_5 batches studied contain only the α_1 modification (Fig. 1). This "purification" of Nb_2O_5 from the η phase is accompanied by increasing perfection of the main (α_1) phase, as evidenced by narrowing of the corresponding diffraction lines.

We also studied by X-ray diffraction the synthesized powders and ceramics of the solid solution (SS) system $(Na_{1-x}Li_x)NbO_3$ with $x = 0.1$ (SS-1) and 0.13 (SS-2) obtained upon firing the samples prepared using all Nb_2O_5 batches. It was found that the parameters, volumes, and deformations of the unit cells in these structures remained virtually the same (deviations from the initial values did not exceed 1.5%). However, considerable changes were observed for the characteristics determining the phase equilibria in solid solutions and their crystal structure perfection. This was manifested by decrease in the relative con-

[1] The ratio of the η and α_1 phase concentrations was estimated by the ratio of intensities of the corresponding strong (110) X-ray diffraction reflections for the coexisting modifications ($I_{110\eta}/I_{110\alpha_1}$).

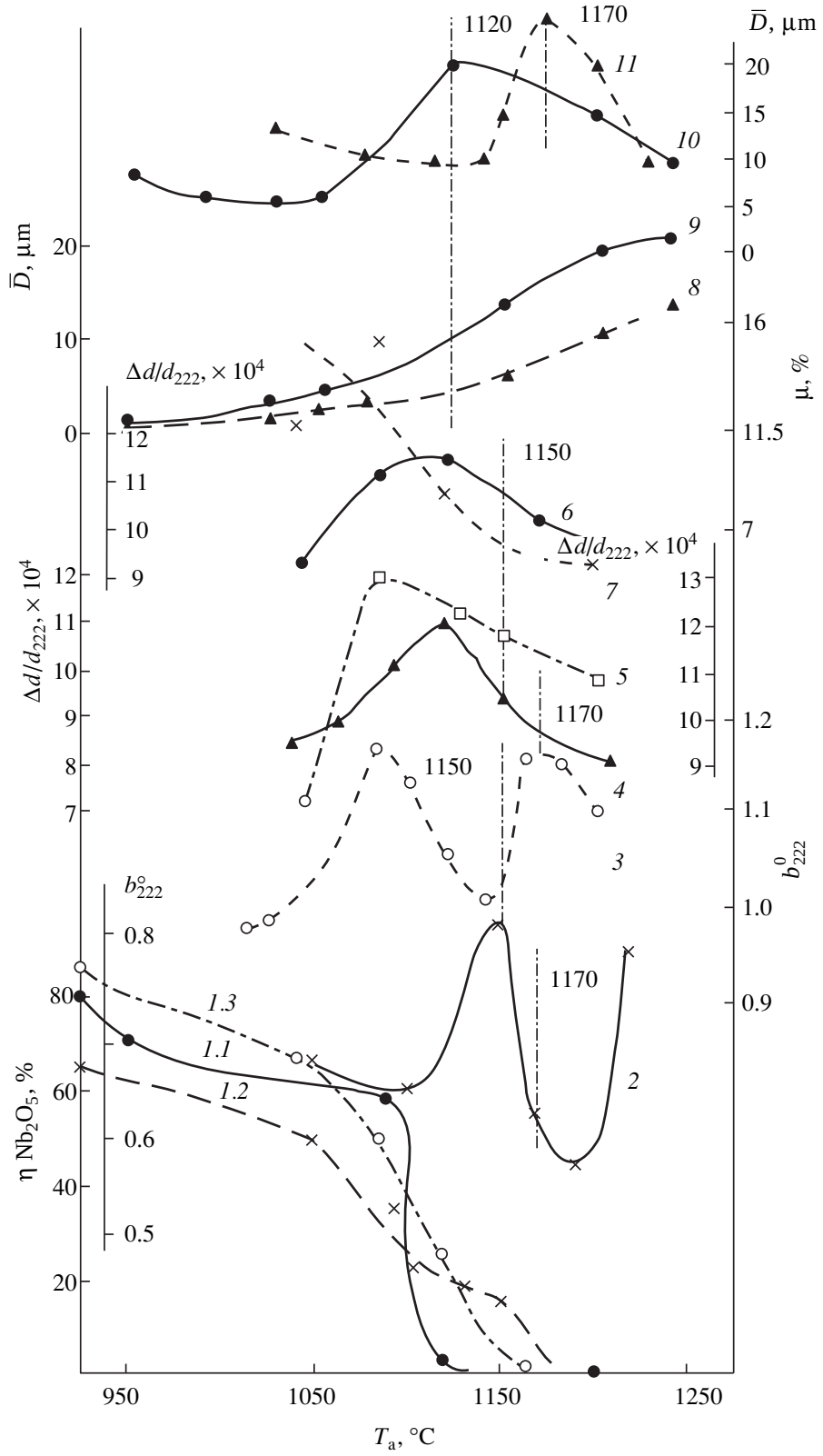

Fig. 1. Effect of the annealing temperature T_a on the crystal structure and microstructure of Nb_2O_5 and related solid solutions: (*1.1–1.3*) percentage content of η-Nb_2O_5 phase in Nb_2O_5 batches 70, 47, and 48, respectively; (*2*, *3*) X-ray diffraction reflection halfwidth b_{222} for SS-1 powder (synthesized from Nb_2O_5 batch 47) and SS-2 powder (b. 48), respectively; (*4–6*) microdeformations $\Delta d/d_{222}$ of SS-1 powder (b. 47), SS-1 powder (b. 48), and SS-2 powder (b. 48), respectively; (*7*) percentage content μ of the *Rh* phase in SS-2; (*8–11*) grain size *D* in SS-2 powder (b. 70), Nb_2O_5 batch 70, SS-2 ceramics (b. 47), and SS-2 ceramics (b. 47).

X-ray diffraction data for Nb_2O_5 samples from three commercial batches measured before thermal treatment (original data)

Batch	Symmetry of α_1 and η phases	Unit cell parameters							
		α_1 modification				η modification			
		a, Å	*b*, Å	*c*, Å	β	*a*, Å	*b*, Å	*c*, Å	β
47	Monoclinic	21.11	3.809	19.35	119°58′	28.58	3.817	17.52	119°48′
48	Monoclinic	21.06	3.806	19.32	119°42′	28.55	3.820	17.47	124°42′
70	Monoclinic	21.29	3.828	19.46	120°43′	28.65	3.821	17.44	124°13′

tent μ of one of the phases[2] coexisting in SS-2, in the integral width b_{222} of the (222) diffraction reflection, and in the level of microdeformations $(\Delta d/d)_{222}$. The anomalous behavior of these characteristics observed far from the $\alpha_1 + \eta \longrightarrow \alpha_1$ phase transition in Nb_2O_5 is probably related to the onset of instability of the η phase (Fig. 1).

Another fact to be noted is the extremal growth of the average grain size ($\bar{D}$) observed for the samples of ceramics in the region of annealing temperatures T_a (Fig. 1). This observation can be explained as follows. An increase in T_a leads to a sharp grain coarsening in Nb_2O_5 and, accordingly, in the synthesized ceramic powders. Occurring far from the phase transition, this process leads to a decrease in activity of the synthesized powder with respect to the recrystallization on sintering. As a result, the $\bar{D}$ value in the ceramics tends to decrease. In contrast, maximum $\bar{D}$ values at T_a in the vicinity of the phase transition in Nb_2O_5 are apparently related, by analogy with the Hedval effect (increased reactivity of solids during or upon polymorphous transformations), to an intensification of the diffusion processes related to a high mobility of the crystal lattice components in the course of its reconstruction. Additional evidence for this interpretation is provided by the fact that the samples treated at T_a in the vicinity of the phase transition in Nb_2O_5 are characterized by minimum values of the temperature of the rapid densification onset in SS powders during sintering and the optimum sintering temperatures T_s of the solid solutions.

This behavior of the structural and microstructural characteristics of $(Na_{1-x}Li_x)NbO_3$ solid solutions determines the nonmonotonic variation of their dielectric, piezoelectric, and mechanical properties (Fig. 2), which exhibit extrema in the vicinity of the polymorphous phase transition temperature in Nb_2O_5. Figure 2 shows the pattern of changes in the dielectric permittiv-

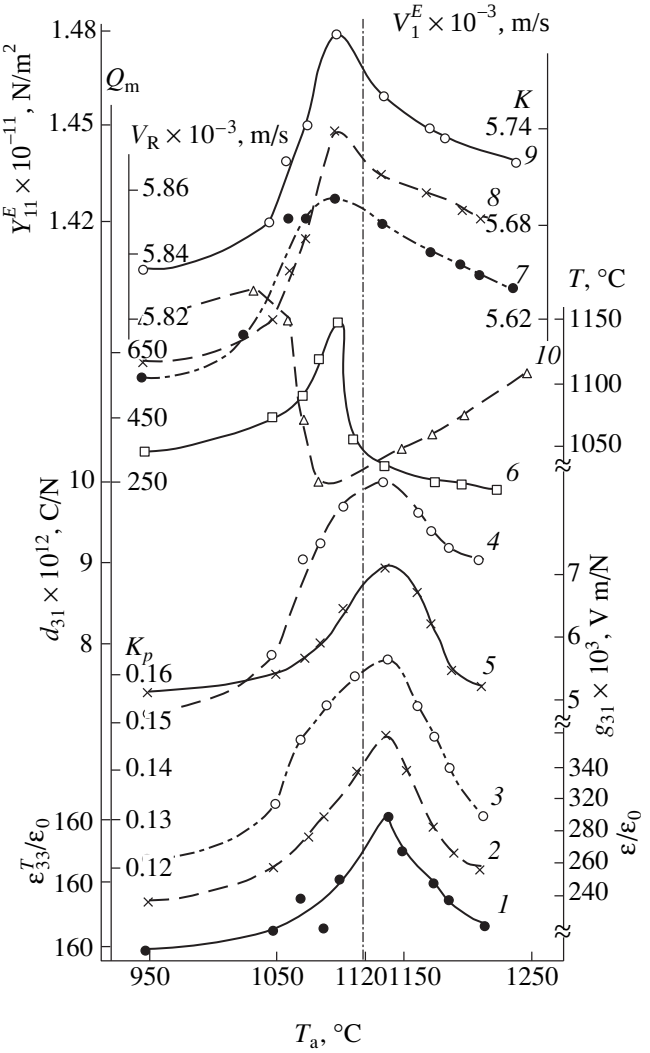

Fig. 2. Effect of the Nb_2O_5 annealing temperature T_a on the electrical and mechanical properties of synthesized solid solutions: (*1*) $\varepsilon_{33}^T/\varepsilon_0$; (*2*) $\varepsilon/\varepsilon_0$; (*3*) K_p; (*4*) d_{31}; (*5*) g_{31}; (*6*) Q_m; (*7*) V_R; (*8*) V_1^E; (*9*) Y_{11}^E; and (*10*) T_s.

[2] According to the phase diagram of the $(Na_{1-x}Li_x)NbO_3$ solid solution system, SS-2 comprises a mixture of the rhombohedral (*Rh*) and orthorhombic (*R*) phases [3]. Since the multiplets belonging to these phases in the X-ray diffraction pattern strongly overlap and cannot be unambiguously resolved, the percentage content of *Rh* was evaluated as $\mu = (I_{211}^{Rh}/\sum I_{N=6}^{Rh+R}) \times 100\%$, where I_{211}^{Rh} is the integral intensity of the (211) reflection of the *Rh* phase and $\sum I_{N=6}^{Rh+R}$ is the total integral intensity of the multiplet with $N = h^2 + k^2 + l^2 = 6$.

ity before ($\varepsilon/\varepsilon_0$) and after ($\varepsilon_{33}^T/\varepsilon_0$) electric polarization, the electromechanical coupling coefficient (K_p), the piezoelectric modulus (d_{31}), piezoelectric sensitivity (g_{31}), mechanical quality factor (Q_m), the velocity of sound (V_R, V_I^E), and the Young modulus (Y_{11}^E). This pattern resembles variation of the same parameters observed in the vicinity of the concentration ferroelectric–ferroelectric (morphotropic) transitions. The only difference is that the response of niobate ceramics to a structural rearrangement is observed essentially in the "second generation," since the phase transition took place in the initial reagent.

Thus, we have demonstrated that the polymorphous phase state of $Nb2O_5$ significantly influences the characteristics of alkali metal niobate solid solution powders and determines the extremal variation of the properties of synthesized ceramics, which must be taken into account in development of the Nb-containing ferroelectric piezoceramics.

Acknowledgments. The work was partly supported by the Russian Foundation for Basic Research, project no. 99-02-17575.

REFERENCES

1. E. G. Fesenko, A. Ya. Dantsiger, L. A. Reznichenko, *et al.*, Zh. Tekh. Fiz. **52** (11), 2262 (1982) [Sov. Phys. Tech. Phys. **27**, 1389 (1982)].
2. *Powder Diffraction File. Inorganic Section* (ICPDS, Swarthmore, 1948–1977), Set. 16–57, 20–804.
3. L. A. Reznichenko and L. A. Shilkina, Izv. Akad. Nauk SSSR, Ser. Fiz. **39** (5), 1118 (1975).

Translated by P. Pozdeev

Technical Physics Letters, Vol. 27, No. 3, 2001, pp. 193–194. Translated from Pis'ma v Zhurnal Tekhnicheskoĭ Fiziki, Vol. 27, No. 5, 2001, pp. 42–45.

The Role of Radiative Damping in Shaping of the Cyclotron Resonance Line in a Two-Dimensional Electron System

V. V. Popov and T. V. Teperik

Institute of Radio Engineering and Electronics (Saratov Division), Russian Academy of Sciences, Saratov, Russia

e-mail: popov@ire.san.ru

Received September 29, 2000

Abstract—It is shown that the broadening of a cyclotron resonance line in a two-dimensional (2D) electron system relative to the inverse scattering time of electrons is connected with the radiative damping accompanying the cyclotron motion of electrons. Using the radiative damping concept, a simple and physically informative formula describing the cyclotron resonance curve shape in a 2D electron system was obtained. © *2001 MAIK "Nauka/Interperiodica".*

It is known that the cyclotron resonance in a two-dimensional (2D) electron system has some specific features that distinguish this effect from the corresponding bulk resonance in semiconductors. In particular, the width of the cyclotron resonance line in a 2D system may be several times larger than the inverse scattering time of electrons in the 2D system; the resonance amplitude becomes saturated when the inverse scattering time decreases [1]. It is also known that, for a low-intensity cyclotron resonance (so-called small-signal approximation), the variation in the transmittance of the electromagnetic wave passing through a 2D electron system is proportional to the real part of the high-frequency ohmic conductance of the 2D system [2, 3]. In the latter case, the width of the cyclotron resonance line coincides with the inverse scattering time of electrons in the 2D system.

A correct and rather simple theoretical description of the shape of the cyclotron resonance line in a 2D system for an arbitrary signal level can be obtained from the solution of the Maxwell equations with boundary conditions accounting for the response of the 2D system [4]. However, this solution does not reveal physical reasons of the line broadening and the saturation of the cyclotron resonance line intensity in a 2D system at large signal levels.

In this letter, we demonstrate that the aforementioned specific features of the cyclotron resonance in a 2D electron system are caused by the radiative damping accompanying the cyclotron motion of electrons. Using the radiative damping concept, a simple and physically transparent formula is derived for description of the shape of the cyclotron resonance line in a 2D system.

Let a 2D electron system occur at the interface of two media with permittivities ε_1 and ε_2. The constant magnetic field $\mathbf{B_0}$ is directed from medium *1* to medium *2*. Consider a linearly polarized electromagnetic wave normally incident from medium *1* onto the surface of the 2D electron system. To alleviate the consideration, we decompose the linearly polarized wave into two partial waves with left- and right-hand circular polarizations. Solving the Maxwell equations with boundary conditions on the interface of media *1* and *2*, which account for the response of a magnetoactive 2D electron system, we obtain the following equations for the complex transmission coefficients t_+ and t_- of the left-hand and right-hand circularly polarized waves, respectively [4]:

$$t_\pm = \frac{E_\pm^{(t)}}{E_\pm^{(i)}} = \frac{2\sqrt{\varepsilon_1}}{\sqrt{\varepsilon_1} + \sqrt{\varepsilon_2} + \frac{4\pi}{c}\sigma_\pm}, \qquad (1)$$

where $E_\pm^{(i)}$ and $E_\pm^{(t)}$ are the amplitudes of electric fields of incident and transmitted partial waves with the left- and right-hand circular polarization;

$$\sigma_\pm = \frac{e^2 N_s}{m^*}\frac{1}{\nu - i(\omega \mp \omega_c)}$$

are the complex conductances of the 2D electron system for electric fields of the left- and right-hand circular polarizations, respectively; ω is the circular frequency of the wave; $\omega_c = |e|B_0/m^*$ is the cyclotron frequency; and e, m^*, N_s, and $\nu = 1/\tau$ are the electron charge and effective mass, the surface electron concentration, and the inverse scattering time of electrons, respectively.

The total power transmission coefficient for a linearly polarized wave is determined by the formula

$$T = (T_+ + T_-)/2,$$

1063-7850/01/2703-0193$21.00

where

$$T_{\pm} = \frac{1}{2}\sqrt{\frac{\varepsilon_2}{\varepsilon_1}}|t_{\pm}|^2.$$

Note that a similar formula derived in [4] is missing the multiplier $\sqrt{\varepsilon_2/\varepsilon_1}$. As a result, the final expression for T derived in that paper contains a wrong coefficient. Correct expressions for $T_{\pm}$ are as follows:

$$T_{\pm} = \frac{4\sqrt{\varepsilon_1\varepsilon_2}}{(\sqrt{\varepsilon_1}+\sqrt{\varepsilon_2})^2}\frac{\nu^2+(\omega\mp\omega_c)^2}{(\omega\mp\omega_c)^2+(\nu+\gamma_r)^2}, \qquad (2)$$

where

$$\gamma_r = \frac{4\pi}{c}\frac{e^2N_s}{m^*(\sqrt{\varepsilon_1}+\sqrt{\varepsilon_2})}$$

is essentially the radiative damping of the free cyclotron motion of electrons in the 2D system [5].

In experiments, one usually measures the relative variation of the transmission coefficient,

$$\frac{\Delta T}{T} = 1-\frac{T(X)}{T(X_0)},$$

where parameters X and X_0 are two different values of either the external magnetic field or the electron concentration in the 2D system. The shape of the resonance curve for coefficient $\Delta T/T$ is independent of the chosen type of these parameters. For definiteness, we will use the following expression for the relative variation of the transmission coefficient:

$$\frac{\Delta T}{T} = 1-\frac{T(N_s)}{T(N_s=0)}.$$

Evidently, $T(N_s = 0) = T_{\pm}(N_s = 0) = 4\sqrt{\varepsilon_1\varepsilon_2}/(\sqrt{\varepsilon_1}+\sqrt{\varepsilon_2})$. Therefore, we obtain

$$\frac{\Delta T}{T} = 1-\frac{T_+(N_s)+T_-(N_s)}{2T(N_s=0)}.$$

For a sufficiently large quality factor of the cyclotron resonance, which corresponds to $\nu, \gamma_r \ll \omega$, we obtain from (2) that $T_-(N_s)/T_-(N_s = 0) \simeq 1$. Then, we may write

$$\frac{\Delta T}{T} = \frac{1}{2}\left[1-\frac{T_+(N_s)}{T(N_s=0)}\right].$$

Substituting explicit expressions for $T_+(N_s)$ and $T_+(N_s = 0)$, we obtain

$$\frac{\Delta T}{T} = \frac{1}{2}\gamma_r\frac{2\nu+\gamma_r}{(\omega\mp\omega_c)^2+(\nu+\gamma_r)^2}. \qquad (3)$$

According to formula (3), the cyclotron resonance in the 2D system is described by a Lorentzian line profile with the resonance amplitude

$$\left(\frac{\Delta T}{T}\right)_{\max} = \frac{1}{2}\gamma_r\frac{2\nu+\gamma_r}{(\nu+\gamma_r)^2}. \qquad (4)$$

The full width of the resonance curve at half maximum (FWHM) is $\Delta\omega = 2(\nu + \gamma_r)$. Thus, the width of the resonance curve is finite even in the absence of electron scattering in the 2D system. The presence of radiative damping broadens the resonance curve. At the same time, the radiative damping plays the role of a parameter accounting for the coupling between an external electromagnetic wave and electrons in the 2D system because, according to formula (4), the amplitude of the cyclotron resonance is proportional to γ_r. At $\nu \longrightarrow 0$, the height of the resonance line saturates on a level of $(\Delta T/T)_{\max} = 0.5$.

The small-signal approximation corresponds to low values of the coupling parameter $\gamma_r \ll \nu$. In this case, the width of the resonance curve is only determined by the inverse scattering time of electrons in the 2D system, $\Delta\omega \simeq 2\nu$.

Acknowledgments. This work was supported by the Federal Program "Integration of Higher Education and Fundamental Science in 1997–2000" (project No. 696.3) and by the Russian Foundation for Basic Research (project 00-02-16440).

REFERENCES

1. E. Batke, D. Heitmann, and C. W. Tu, Phys. Rev. B **34** (10), 6951 (1986).
2. G. Abstreiter, J. P. Kotthaus, J. P. Koch, and G. Dorda, Phys. Rev. B **14** (6), 2480 (1976).
3. U. Merkt, M. Horst, T. Evelbauer, and J. P. Kotthaus, Phys. Rev. B **34** (10), 7234 (1986).
4. K. W. Chiu, T. K. Lee, and J. J. Quinn, Surf. Sci. **58**, 182 (1976).
5. O. R. Matov, O. F. Meshkov, O. V. Polishchuk, and V. V. Popov, Zh. Éksp. Teor. Fiz. **109** (3), 876 (1996) [JETP **82**, 471 (1996)].

Translated by A. Kondrat'ev

Technical Physics Letters, Vol. 27, No. 3, 2001, pp. 195–196. Translated from Pis'ma v Zhurnal Tekhnicheskoĭ Fiziki, Vol. 27, No. 5, 2001, pp. 46–49.

The Tunneling Capture of Electrons Modifies the Width of the Electric Field Strength Interval Featuring Negative Differential Conductivity

Z. S. Kachlishvili and N. K. Metreveli

Tbilisi State University, Tbilisi, Georgia

e-mail: faculty@tsi.ge

Received July 28, 2000

Abstract—In order to provide for the stable operation of active elements, it is important to select an optimum width of the interval of the electric field strengths corresponding to negative values of the differential conductivity. The effects of both the internal factors and the applied magnetic field on this interval width were theoretically studied for *n*-Ge. The optimum intervals of the electric and magnetic field strengths were determined, which provide for most reliable operation of the active elements. © *2001 MAIK "Nauka/Interperiodica".*

An important condition for a stable operation of the active elements working in the regime of negative differential conductivity (NDC) is the constant width of the electric field strengths featuring this regime. An increase in the width of this interval, of course provided that a sufficiently sharp dependence of the charge carrier mobility and/or concentration on the field strength is retained, would increase the reliability of system operation. Therefore, it is an important task to reveal and study the internal and external factors affecting the above interval width. We have studied this problem for *n*-Ge under the conditions of NDC related to nonlinear carrier concentration in the system.

As is well known, the nonlinear charge carrier concentration in *n*-Ge doped with gold or copper is related to the tunneling capture of hot electrons by negatively charged metal ions. The electron capture coefficient is conventionally calculated in terms of the capture probability originally determined by Bonch-Bruevich [1]. However, Abakumov *et al.* [2] showed that, to be captured by this mechanism, electrons must decrease their energy upon tunneling by emitting phonons. An allowance for this circumstance leads to additional factor in the Bonch-Bruevich electron capture cross section [2]:

$$\sigma(W) \sim \exp\left(-\frac{2\tau_1}{\hbar}\right)W, \qquad (1)$$

where W is the kinetic energy that has to be lost by electron to be captured and τ_1 is the characteristic tunneling time.

With this additional factor taken into account in various approximations [2–4], it was demonstrated that the Bonch-Bruevich model is quite adequate in relatively weak fields; as the electric field strength increases, the $\sigma(W)$ factor given by Eq. (1) becomes substantial. Here, questions naturally arise as to whether this factor affects the interval of the electric field strengths featuring NDC, how to account for this influence, and what the possible effect of external magnetic fields is. Below, we report on the results of our theoretical study of these questions for *n*-Ge in crossed electric and magnetic fields within the framework of the quasielastic electron scattering approximation.

The free electron concentration in the system is described by a conventional relationship [5] using a nonequilibrium distribution function

$$f_0(x) = A\exp\left(-\frac{\eta^{\zeta}x^{\xi}}{\alpha\xi}\right), \quad \xi > 0, \qquad (2)$$

where $\zeta = 0$ and $\xi = \xi_1 = 1 - \frac{t+s}{2}$ for a weak electric field; $\zeta = 1$ and $\xi = \xi_2 = 1 + \frac{t-s}{2}$ for a strong electric field; t and s are the exponents in the electron mean free path dependence on the momentum and energy, respectively;

$$l = l_0 x^{\frac{1+t}{2}}, \quad \tilde{l} = \tilde{l}_0 x^{\frac{1+s}{2}}, \quad \alpha \equiv \left(\frac{E}{E_0}\right)^2, \quad \eta \equiv \left(\frac{H}{H_0}\right)^2,$$

$$E_0 \equiv \sqrt{3}\frac{k_0 T}{e(l_0\tilde{l}_0)^{1/2}}, \quad H_0 \equiv \frac{(2mc^2 k_0 T)^{1/2}}{el_0};$$

and A is the normalization coefficient.

The numerical calculations were performed by the saddle-point method for $\xi = 1$, but the results are qualitatively valid for $\xi \neq 1$ as well. Consideration of this case covers a rather broad spectrum of real scattering

mechanisms [6] and markedly simplifies the analysis of results.

According to the results of calculations, $n \propto \Delta^{-1}$, where

$$\Delta = \Delta_0 \frac{\left(\frac{\alpha}{\eta^\zeta}\right)^{-3/2}}{\left(\gamma_0 + \frac{\eta^\zeta}{\alpha}\right)^{5/6}} \exp\left\{-3\left(\frac{\gamma}{2}\right)^{2/3}\left(\gamma_0 + \frac{\eta^\zeta}{\alpha}\right)^{1/3}\right\}, \quad (3)$$

$$\gamma \equiv \frac{2\pi z e^2}{\varepsilon \hbar v_T}, \quad \gamma_0 = \frac{2\tau_1}{\hbar} kT,$$

z is the charge of repulsing center (expressed in the units of electron charge), ε is the dielectric permittivity, v_T is the thermal velocity, and

$$\Delta_0 \equiv \frac{\sqrt{\pi}}{2\Gamma\left(\frac{3}{2}\right)}(1+\gamma_0)^{5/6} \exp\left\{3\left(\frac{\gamma}{2}\right)^{2/3}(1+\gamma_0)^{1/3}\right\}. \quad (3a)$$

As can be seen, the electron concentration decreases with increasing electric field strength $\left(\frac{\partial}{\partial\alpha}\left(\frac{\Delta}{\Delta_0}\right) > 0\right)$ and reaches a minimum at

$$\left(\frac{\alpha}{\eta^\zeta}\right)_{\min 1} = \frac{2}{3}\left(\frac{\gamma}{\gamma_0}\right). \quad (4)$$

In this case, the factor described by Eq. (1) dominates and $\gamma_0 \gg \frac{\eta^\zeta}{\alpha}$.

Comparing Eq. (4) to the analogous value for the conditions when the factor (1) can be ignored ($\gamma_0 \ll \frac{\eta^\zeta}{\alpha}$) and taking into account that $\gamma \gg 1$ for the case under consideration, we obtain

$$\frac{\left(\frac{\alpha}{\eta^\zeta}\right)_{\min 1}}{\left(\frac{\alpha}{\eta^\zeta}\right)_{\min 2}} \sim \frac{2}{\left(\frac{\gamma}{2}\right)^{4/3}} \ll 1. \quad (5)$$

The estimate refers to $T \sim 20$ K and employs the relationship $\gamma_0 \sim \frac{T}{10^3}$ [3].

Summarizing the obtained results, we may conclude the following:

(i) Equation (3) shows that the electron tunneling capture factor given by Eq. (1) dominates in the case of strong electric and weak magnetic fields;

(ii) The Bonch-Bruevich approximation is valid in the case of weak electric and strong magnetic fields;

(iii) Factor (1) decreases the electric field strength corresponding to minimum of the free electron concentration;

(iv) Taking into account that the NDC sign changes to opposite at the electric field strength corresponding to minimum of the free electron concentration, we may ascertain that operation under the conditions of weak electric and strong magnetic fields $\left(\frac{E}{E_0} < \left(\frac{\eta^\zeta}{\gamma_0}\right)^{1/2}\right)$, where the term proportional to γ_0 can be ignored, increases reliability of the active elements. However, if the field dependence of the carrier mobility compensates for a decrease in the free electron concentration, the NDC is retained in the interval of field strengths where the term with γ_0 dominates $\left(\frac{E}{E_0} > \left(\frac{\eta^\zeta}{\gamma_0}\right)^{1/2}\right)$, which is favored by weak magnetic fields).

REFERENCES

1. V. L. Bonch-Bruevich, Fiz. Tverd. Tela (Leningrad) **6** (7), 2047 (1964) [Sov. Phys. Solid State **6**, 1615 (1965)].
2. V. G. Abakumov, V. Karpus, V. I. Perel', and I. N. Yasievich, Fiz. Tekh. Poluprovodn. (Leningrad) **22** (2), 262 (1988) [Sov. Phys. Semicond. **22**, 159 (1988)].
3. Kh. Z. Kachlishvili, Z. S. Kachlishvili, and F. G. Chumburidze, Fiz. Tekh. Poluprovodn. (St. Petersburg) **31** (8), 944 (1997) [Semiconductors **31**, 804 (1997)].
4. Z. S. Kachlishvili, Kh. Z. Kachlishvili, and F. G. Chumburidze, Fiz. Tekh. Poluprovodn. (St. Petersburg) **31** (2), 204 (1997) [Semiconductors **31**, 161 (1997)].
5. V. L. Bonch-Bruevich, I. P. Zvyagin, and A. G. Mironov, *Domain Electrical Instabilities in Semiconductors* (Nauka, Moscow, 1972; Consultants Bureau, New York, 1975).
6. Z. S. Kachlishvili, Phys. Status Solidi A **33**, 15 (1976).

Translated by P. Pozdeev

Technical Physics Letters, Vol. 27, No. 3, 2001, pp. 197–199. Translated from Pis'ma v Zhurnal Tekhnicheskoĭ Fiziki, Vol. 27, No. 5, 2001, pp. 50–56.

Special Features in the Synthesis and Properties of Thin Y–Ba–Cu–O High-Temperature Superconductor Films Free of Secondary Phases

A. K. Vorobiev, N. V. Vostokov, S. V. Gaponov, Yu. N. Drozdov, E. B. Klyuenkov, and Yu. N. Nozdrin

Institute for Physics of Microstructures, Russian Academy of Sciences, Nizhni Novgorod, Russia

e-mail: vorobyev@ipm.sci-nnov.ru

Received October 13, 2000

Abstract—Data on the structure and transport properties of thin Y–Ba–Cu–O (YBCO) high-temperature superconductor films obtained by magnetron sputtering of a stoichiometric target in a system with a 90° off-axis geometry are reported. It is shown that the films prepared under these conditions are free of copper-rich secondary phases and are characterized by the surface roughness height below 10 nm. The films possess a perfect structure and exhibit high superconducting properties: *c*-axis misorientation in microblocks FWHM(005)YBCO = 0.4–0.5°; zero-resistance temperature T_{co} = 89 K; critical (pinning) current density j_p = 1.5–2 MA/cm^2 (77 K). © *2001 MAIK "Nauka/Interperiodica".*

It was demonstrated [1–4] that thin films of high-temperature superconductors of the Y–Ba–Cu–O (YBCO) system possessing best transport properties (zero-resistance temperature $T_{co} > 90$ K; critical current density $j_c > 2$ MA/cm^2 at 77 K; microwave surface resistance $R_s < 1.0$ mΩ at 77 K and 10 GHz) are obtained provided that the deposit is strongly (up to 100%) enriched with copper and yttrium. These conditions favor the formation of a heterogeneous system comprising a film of the stoichiometric 1–2–3 phase with distributed particles of CuO and Y_2O_3 secondary phases. The secondary-phase CuO particles are characterized by a hemispherical shape, a characteristic size of 0.5 μm, and a concentration of 10^8 cm^{-2}. Unfortunately, the presence of these CuO particles presents a serious problem from the standpoint of obtaining devices with multilayer structures. In addition, the CuO particles significantly contribute to the microwave losses [5] and, hence, detrimentally affect the parameters of microwave devices.

The YBCO films with compositions corresponding to stoichiometric integral cation ratio (1–2–3) contain no secondary-phase particles but exhibit somewhat lower transport properties ($T_{co} < 88$ K; $j_c < 2$ MA/cm^2 at 77 K; $R_s > 2$ mΩ). This effect is observed irrespective of the method used for the YBCO film fabrication (laser, magnetron, electron-beam sputtering, metalorganic chemical vapor deposition). It was suggested that deterioration of the transport properties of stoichiometric YBCO films is related to a cation disorder in the unit cell (Ba–Y substitution [1] and the formation of Cu vacancies [4]).

Therefore, the problem of growing single-phase YBCO films possessing high electric parameters is still of considerable importance. Below, we present data on the synthesis and properties of thin YBCO films containing no copper-rich secondary phases.

Previously [6–9], we have thoroughly studied processes responsible for the cation composition of YBCO films grown *in situ* in an inverted cylindrical magnetron sputtering (ICMS) system [6–9]. The mass transfer in the target volume, selective reevaporation, and preferential desorption of YBCO components from the substrate and surrounding parts of the working unit result in that the films obtained in the ICMS system are enriched with copper and yttrium (within the range of compositions corresponding to the atomic ratios Cu/Ba = 2–3.5 and Cu/Y = 2.6–4).

In order to exclude the factors hindering reproduction of the target composition in the YBCO film (deposit), we have designed and constructed a special magnetron sputtering system with a 90° off-axis geometry based on a planar magnetron configuration analogous to that described in [10]. This design allows the sputtering process to be performed using sufficiently thin targets, thus improving the heat transfer conditions and excluding mass transfer in the target volume. In addition, the target–substrate space of the modified system contains no structural parts that might accumulate the sputtered material and become the secondary sources of YBCO components.

Figure 1 shows a schematic diagram of the magnetron sputtering system used in this work. We employed a disk target with the stoichiometric $YBa_2Cu_3O_7$ composition (KIB-1 grade, State Standard TU 48-0531-390-88;

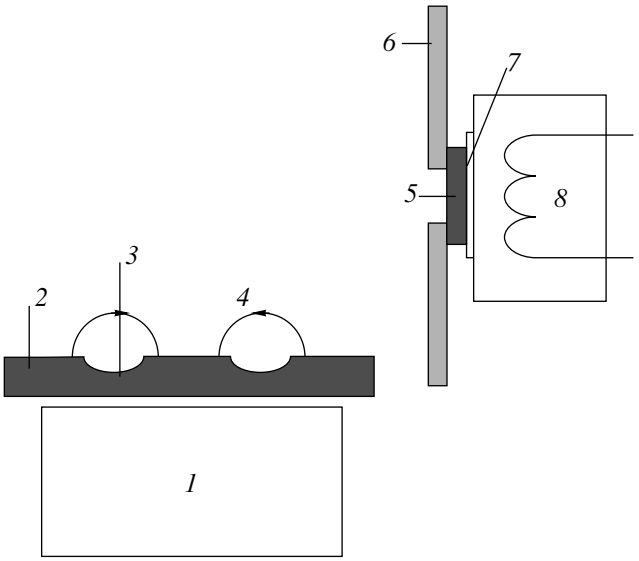

Fig. 1. A schematic diagram of the magnetron sputtering system with a 90° off-axis geometry: (*1*) cathode magnetron unit; (*2*) target; (*3*) target erosion zone; (*4*) magnetic induction lines; (*5*) substrate; (*6*) quartz shield; (*7*) In–Ga eutectic; (*8*) substrate heater.

diameter, 60mm; thickness, 3 mm) manufactured on the GIREDMET Experimental Plant (Pyshma). The erosion zone diameter on the target surface is ~25 mm. The sputtered material deposited onto substrates heated by contact with an In–Ga eutectic. A distinguishing feature of the system design is the quartz shield *6* blocking the fluxes of YBCO components reevaporated from peripheral parts of the heater. The shield was maintained at a temperature 200–250°C below that of the substrate.

The YBCO films studied in this work were grown *in situ* under the following conditions: $NdGaO_3$ substrates, 10×10 mm^2; substrate temperature, 680°C; working gas (Ar : O_2 1 : 1 mixture) pressure, 20 Pa; target voltage, 155 V; discharge current, 400 mA. After termination of the deposition cycle, the working chamber was filled with oxygen at a pressure of 1 atm. The deposition rate was ~120 nm/h; the sample film thickness was ~100 nm. We have prepared and studied a series of five samples, which were characterized with respect to their surface morphology, microstructure, and the electrical and magnetic properties.

The film surface relief was studied with an atomic force microscope (AFM) of the Solver-P4 type (NT-MDT Company, Zelenograd, Russia) operating in a contact mode. Figure 2a shows the AFM image of a typical surface relief, clearly illustrating a microblock structure (with a block size of ~0.5 μm). Characteristic of the YBCO films. The arrow marker indicates an *a*-oriented YBCO domain, a small number of which is usually present in YBCO films grown on $NdGaO_3$ substrates [11]. It is important to note that no any inclusions of copper-rich secondary phases are observed in the image. According to the AFM data, the film surface roughness height is <10 nm. For comparison, Fig. 2b shows the image of an YBCO film prepared previously in the ICMS system [12], which reveals hemispherical particles of a secondary CuO phase with an average size of ~0.2 μm.

The microstructure of YBCO films was analyzed on a DRON-4 diffractometer using CuK_α radiation. The instrument was equipped with a GP-3 goniometer attachment modified for the study of single crystal layers. The *c*-axis misorientation in mosaic microblocks was characterized by the FWHM(005)YBCO value representing the full width at half maximum of the rocking curve of the (005)YBCO reflection. In all samples, the FWHM(005)YBCO values fell within 0.39°–0.47°, which corresponds to high-quality YBCO films.

The temperatures corresponding to the onset ($T_{c\,on}$) and end (T_{co}) of the superconducting transition, as well as the parameter γ (the ratio of sample resistances at 300 and 100 K) for the YBCO films were determined from the temperature dependence of the sample resistance measured by a compensation method at a dc current of 100 μA. The sample temperature was measured to within ±0.5 K by a temperature sensor of the TPK 20.1 type. The T_{co} value was determined at a point where the electric field strength was equal to 1 μV/cm. In high-quality YBCO films, the value of γ characterizing the quality of the intergranular contacts [13] should vary within 2.7–3.0. All the YBCO films in the series studied had $T_{c\,on} = 91$ K, $T_{co} = 89$ K, and $\gamma = 2.7$.

The magnetic properties of YBCO films were studied using a method described in [14]. According to this technique, the magnetic induction distribution in a sample upon switching off the external field was measured with a scanning InSb-based Hall transducer. The pinning current j_p was calculated using the maximum magnetic induction value within the framework of the critical state model [15]. In the series of samples studied, the j_p values varied within 1.5–2.0 MA/cm^2 at 77 K (for one of the samples, we obtained $j_p = 2.0 \times 10^7$ A/cm^2 at 4.2 K).

Based on the results described above, we can make the following conclusions. The magnetron sputtering system with a 90° off-axis geometry apparently ensures a sufficiently precise coincidence of the film and target compositions, which implies that sputtering of a stoichiometric YBCO target leads to the growth of YBCO films with the stoichiometric 1–2–3 integral cation ratio. These YBCO films contain no inclusions of copper-rich secondary phases. The electrical parameters of the YBCO films obtained in our experiments ($T_{c\,on} =$ 91 K, $T_{co} = 89$ K; $\gamma = 2.7$; $j_p = 1.5$–2.0 MA/cm^2 at 77 K and $j_p = 2.0 \times 10^7$ A/cm^2 at 4.2 K) are higher than the values reported by other researchers for the stoichiometric YBCO films. We may suggest that the growth of

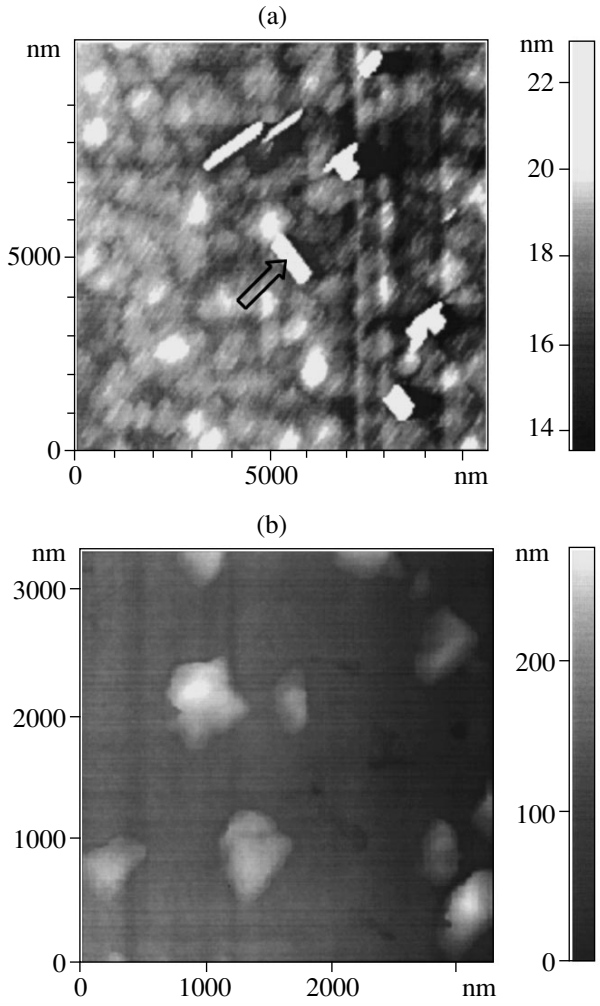

Fig. 2. AFM images of the surface of YBCO films grown in a magnetron sputtering system (a) with a 90° off-axis geometry (arrow indicates an *a*-oriented YBCO domain) and (b) with inverted cylindrical geometry [12].

YBCO films under conditions realized in the system employed is characterized by inhibited processes of the cation disordering. We are planning experiments with targets of variable composition, which would allow us to study the effect of cation composition on the properties of YBCO films and elucidate the mechanisms of this influence. The YBCO films obtained using this magnetron sputtering technology can be used for creating high-quality microwave devices and multilayer film structures for high-T_c magnetometers.

Acknowledgments. This study was performed within the framework of the Federal Program "Investigations and Developments in Priority Directions of Science and Civilian Technologies" (project no. 107-3(00)-P) and additionally supported by the Federal Program "Fundamental Research and Higher Education" and by the Center for Scanning Probe Microscopy at the Nizhni Novgorod State University.

REFERENCES

1. B. Schulte, M. Maul, P. Häussler, *et al.*, Appl. Phys. Lett. **62** (6), 633 (1993).
2. J. Hudner, O. Thomas, E. Mossang, *et al.*, J. Appl. Phys. **74** (7), 4631 (1993).
3. N. G. Chew, J. A. Edwards, R. G. Humphreys, *et al.*, IEEE Trans. Appl. Supercond. **5** (2), 1167 (1995).
4. T. Yoshitake, W. Hattori, and S. Tahara, IEEE Trans. Appl. Supercond. **9** (2), 3058 (1999).
5. J. Z. Liu, Y. J. Tian, L. Li, *et al.*, J. Appl. Phys. **77** (3), 1165 (1995).
6. Y. N. Drozdov, S. V. Gaponov, S. A. Gusev, *et al.*, in *Extended Abstract Book of the ISEC'97, 1997*, Vol. 2, p. 49.
7. A. K. Vorob'ev, S. V. Gaponov, M. N. Drozdov, *et al.*, Pis'ma Zh. Tekh. Fiz. **24** (24), 13 (1998) [Tech. Phys. Lett. **24**, 952 (1998)].
8. M. N. Drozdov, S. V. Gaponov, S. A. Gusev, *et al.*, IEEE Trans. Appl. Supercond. **9** (2), 2371 (1999).
9. A. K. Vorob'ev, S. V. Gaponov, M. N. Drozdov, *et al.*, Fiz. Tverd. Tela (St. Petersburg) **42** (4), 589 (2000) [Phys. Solid State **42**, 603 (2000)].
10. R. A. Rao, Q. Gan, C. B. Eom, *et al.*, Appl. Phys. Lett. **69** (25), 3911 (1996).
11. Julia M. Philips, J. Appl. Phys. **79** (4), 1829 (1996).
12. A. K. Vorobiev, Y. N. Drozdov, S. A. Gusev, *et al.*, Supercond. Sci. Technol. **12**, 908 (1999).
13. E. J. Cukauskas, L. H. Allen, G. K. Sherrill, *et al.*, J. Appl. Phys. **74** (11), 6780 (1993).
14. Yu. N. Nozdrin, A. S. Mel'nikov, I. D. Tokman, *et al.*, IEEE Trans. Appl. Supercond. **9** (2), 1602 (1999).
15. P. N. Mikheenko and Yu. E. Kuzovlev, Physica C (Amsterdam) **24**, 229 (1993).

Translated by P. Pozdeev

Technical Physics Letters, Vol. 27, No. 3, 2001, pp. 200–201. Translated from Pis'ma v Zhurnal Tekhnicheskoĭ Fiziki, Vol. 27, No. 5, 2001, pp. 57–60.

The Effect of Oxygen Precipitates on the Recombination Characteristics of Silicon

S. V. Bulyarskiĭ, A. S. Ambrozevich, V. V. Svetukhin, and T. A. Dzhabrailov

Ul'yanovsk State University, Ul'yanovsk, Russia

Received October 12, 2000

Abstract—The recombination characteristics of silicon single crystals containing oxygen precipitates were studied. It is demonstrated that the reverse-bias current–voltage characteristics can be improved by annealing the samples at 950°C. © *2001 MAIK "Nauka/Interperiodica".*

One of the numerous technologies employed in modern microelectronics is based on the internal gettering process [1, 2], according to which the Czochralski-grown single-crystal silicon wafers are annealed at high temperatures. The annealing results in the appearance of oxygen precipitates, which is accompanied by the formation of dislocation loops. The dislocation loops produce internal stresses and serve as the effective sinks for some technological impurities (e.g., Fe, Mn, Cu) strongly affecting the charge carrier lifetime—an important characteristic of the material. The purpose of this study was to evaluate the effect of oxygen precipitates on the recombination characteristics of silicon. We have studied the Czochralski-grown single-crystal silicon wafers (KEF grade, 8 Ω cm) with an initial oxygen content of 1.4×10^{18} cm^{-3}. The interstitial oxygen concentration was determined by measuring the IR absorption intensity at 1106 cm^{-1}.

In order to determine the effect of oxygen precipitates on the recombination characteristics of silicon, the single-crystal samples were annealed at T = 950°C for various times up to 30 h. As a result of the thermal treatment, the samples are featuring oxygen precipitation that can be monitored by measuring a decrease in the interstitial oxygen concentration at the expense of the precipitate formation. The silicon wafers annealed for various times, as well as the initial material, were used to prepare the Schottky diodes. These diodes were characterized by method of thermostimulated capacitance (TSC) spectroscopy.

The TSC spectra were measured using the following procedure. First, a direct-bias voltage (0.5 V) was applied to the sample and it was cooled down to 77 K in liquid nitrogen. Then a 3-V reverse bias was applied and the sample was heated at a constant rate to room temperature. Figure 1 shows the TSC spectra obtained by processing the experimental data using the method described in [3]. The spectra reveal the presence of deep trapping centers, which were characterized by the activation energies, concentrations, and electron trapping cross sections. These data are summarized in the table. The initial (unannealed) silicon samples contained trapping centers of the vacancy–oxygen (E_c – 0.18 eV) and vacancy–phosphorus (E_c – 0.44 eV) complex type. The thermal treatment (annealing) leads to a decrease in concentration of the vacancy–oxygen complexes. This result can be related to the fact that these complexes are involved in the oxygen precipitation. The vacancy–phosphorus complexes completely vanish upon annealing. Apparently, this complex may either decompose or transform into a complex of different type. The annealed samples exhibit deep trapping centers of a new type occurring at the middle of the forbidden band (E_t = 0.55 eV). These centers are probably related to the oxygen precipitates, which is confirmed by a relatively high value of the trapping coefficient.

Parameters of deep centers in silicon before and after annealing for 15 h at 950°C

T_m, K	E_t, eV	C, cm^{-3} s	N_t, cm^{-3}
Before annealing			
93	0.18	1.5×10^{-10}	9.5×10^{14}
121	0.21	6.9×10^{-12}	5.6×10^{14}
137	0.23	2.5×10^{-12}	1.1×10^{15}
153	0.25	1.1×10^{-12}	1.9×10^{15}
178	0.30	1.4×10^{-12}	3.3×10^{15}
199	0.40	5.6×10^{-11}	4.5×10^{15}
217	0.44	5.6×10^{-11}	6.5×10^{15}
After annealing			
96	0.18	6.7×10^{-11}	5.1×10^{14}
153	0.19	9.0×10^{-15}	5.2×10^{15}
173	0.30	2.8×10^{-12}	2.4×10^{15}
196	0.40	8.4×10^{-11}	4.4×10^{15}
216	0.55	2.9×10^{-9}	4.6×10^{14}

1063-7850/01/2703-0200$21.00

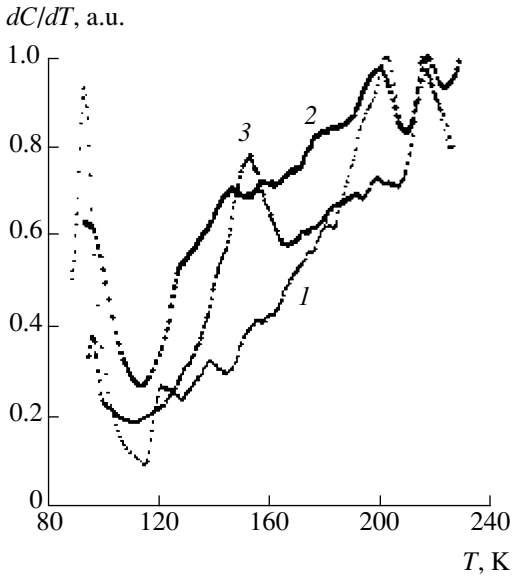

Fig. 1. TSC spectra of silicon samples (*1*) before and (*2*, *3*) after annealing at 950°C for (*2*) 5 h and (*3*) 10 h.

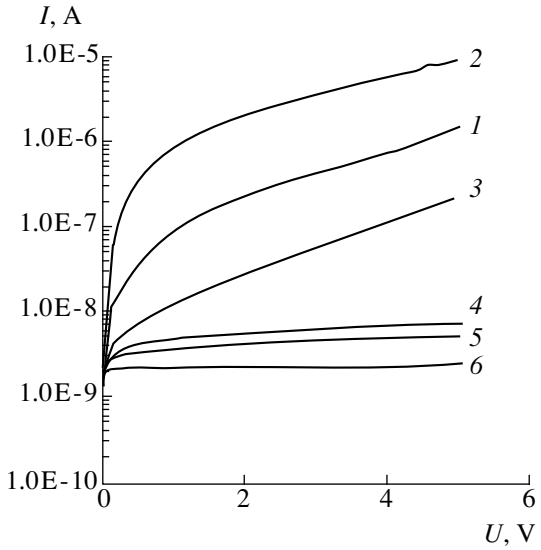

Fig. 2. Reverse-bias current–voltage characteristics of Schottky diodes (*1*) before and (*2*–*6*) after annealing at 950°C for (*2*) 5, (*3*) 10, (*4*) 15, (*5*) 20, and (*6*) 30 h.

Figure 2 shows the reverse-bias current–voltage characteristics measured for the initial and annealed samples. The thermal treatment resulted in a decrease of the reverse saturation current. This result is related to a decrease in concentration of the deep levels affecting the recombination characteristics of silicon.

We have also studied the reverse-bias current–voltage characteristics of Schottky diodes preliminarily treated at 1100°C. These samples are characterized by an increase of the reverse saturation current, which is apparently related to the fact that the annealing at 1100°C leads to the formation of stacking faults in the crystal volume. These defects could be observed on cleaved samples pretreated with a selective Sirtle etchant and examined in a microscope. No such defects were observed in the samples treated at 950°C.

REFERENCES

1. R. A. Graven, Mater. Res. Soc. Symp. Proc. **36**, 159 (1985).
2. A. Borghesi, B. Pivac, A. Sassella, *et al.*, J. Appl. Phys. **77**, 4169 (1995).
3. S. V. Bulyarskiĭ and N. S. Grushko, *Generation-Recombination Processes in Active Elements* (Mosk. Gos. Univ., Moscow, 1995).

Translated by P. Pozdeev

Technical Physics Letters, Vol. 27, No. 3, 2001, pp. 202–203. Translated from Pis'ma v Zhurnal Tekhnicheskoĭ Fiziki, Vol. 27, No. 5, 2001, pp. 61–65.

A Mechanism of the Fréedericksz Surface Dynamic Effect

A. V. Koval'chuk

Institute of Physics, National Academy of Sciences of Ukraine, Kiev, Ukraine

e-mail: akoval@iop.kiev.ua

Received July 22, 2000

Abstract—It is shown that the period of low-frequency relaxation processes involved in the local reorientation of molecules in a plane-oriented nematic liquid crystal is determined both by relaxation of a weakly deformed director upon switching off the applied field and by redistribution of the voltage drop between the bulk and the near-electrode region (electric double layer). The maximum deformation of the director takes place in the surface layer with a thickness equal to the Debye screening length. *© 2001 MAIK "Nauka/Interperiodica".*

As was originally demonstrated in [1], the onset of the low-frequency dispersion of ε' and ε" in a plane-oriented nematic liquid crystal (LC) is due to a local change in the orientation of molecules under the action of an external electric field. It was suggested that the change in the orientation of molecules in the surface layer is determined by redistribution of the electric field strength between the bulk and the electric double layer as well as inside the electric double layer.

However, it is still unclear what is the mechanism of the local reorientation of molecules and how the relaxation time τ depends on the parameters of the substance and the measuring cell. It was expected that most important information concerning the mechanism of the Fréedericksz surface dynamic effect could be obtained by studying dependence of the τ value on the sample thickness d and on the probing signal amplitude. This dependence was analyzed using the data obtained previously [1, 2] and the new experimental results. The experimental methods were the same as those described in [1, 2].

As seen from the experimental data summarized in the table, dependence of the relaxation time on the sample thickness in the interval of d = 3–22 μm obeys the relationship $\tau \sim d^2$. As is known [3], the same law is obtained from theoretical analysis of the process of LC director reorientation upon switching off the applied field. In this case, the relaxation to the initial state is controlled by the balance of elastic and viscous moments

$$K_{22}\frac{d^2\Theta}{dz^2} = \gamma\frac{d\Theta}{dt}, \qquad (1)$$

where K_{22} is the Frank elastic modulus, Θ is the angle of the director orientation relative to the substrate surface, and γ is the viscosity. A solution to Eq. (1) has the form of a series of harmonics

$$\tau_n = \frac{\gamma d^2}{\pi^2 K_{22}(2n+1)^2}, \qquad (2)$$

where n is the harmonic order.

As seen from Eq. (2), a minimum change in the configuration corresponds to the zero-order harmonic (n = 0). The values of τ_0 listed in the table refer to a mixed LC of the RKS 1282 type (γ = 0.012 P; $K_{22} = 1.1 \times 10^{-11}$ N). As seen the τ and τ_0 values are quite comparable (taking into account that most simple relationships were chosen for this analysis) and virtually coincide for d = 3.3 μm. The fact that τ and τ_0 values are of the same order in magnitude indicates that local changes of the orientation of molecules are determined by a frequency corresponding to the least deformed director configuration for the whole sample. A deformation at this frequency takes place in the very first stage of the process of reorientation and can be called the deformation precursor. The hypothesis that the

Parameters of the low-frequency relaxation processes involved in the local variation of the orientation of molecules in a mixed LC of the RKS 1282 type (probing signal amplitude, 0.5 V; temperature, 294 K; H_C is the critical magnetic field strength for the Fréedericksz effect)

d, μm	H/H_C	τ, ms	τ_0, ms	W, μm
3.3	0	1.4	1.2	0.25
7.2	0	17	5.7	0.32
7.2	0.1	15		0.31
12	0	101	15.8	0.26
12	0.17	81		0.18
22	0	172	53.2	0.20

1063-7850/01/2703-0202$21.00 © 2001 MAIK "Nauka/Interperiodica"

relaxation time τ for the local Fréedericksz effect is determined by the time of director relaxation upon switching off the applied field is confirmed by the fact that τ is independent of the probing signal amplitude [2].

We have also studied the near-electrode relaxation processes in the samples exposed to a magnetic field with a strength H at which the LC director exhibits significant deviations from planar orientation. In this case, we also observed the relaxation processes corresponding to the local Fréedericksz effect. As seen from the table, the τ value decreases upon application of the magnetic field. In a sufficiently strong magnetic field, the director configuration deviates from strictly planar. Therefore, relatively small changes in the parameters indicate that τ_0 is weakly dependent on the initial director configuration; this conclusion is also confirmed by the data reported in [1].

The model proposed above does not take into account an important experimental fact, according to which τ is proportional to the sample resistivity ρ [1]. As was noted in [1], the relationship $\tau \sim \rho$ is related to the process of the electric field (or voltage drop) redistribution in the sample. Therefore, the τ value (albeit still determined by the relaxation of weakly deformed director) must correspond to the time of the field redistribution in the near-electrode region. The higher the sample conductivity, the smaller the field redistribution time, and the higher the harmonic order in formula (2) corresponding to the period of local changes in the orientation of molecules.

A typical temperature variation of τ is illustrated in the figure by data for a liquid crystal of the 8TsB type. As seen, τ (as well as most of the other parameters) is characterized by a certain activation energy significantly depending on the type of the mesophase surrounding the sample. It is important to note that a local reorientation of molecules may also proceed in an isotropic phase featuring no bulk orientation ordering. Evidently, an isotropic phase (even in a surface region) may exhibit an insignificant order in the orientation of molecules. This fact also confirms the proposed mechanism of relaxation of a weakly oriented director.

Until now, the mechanism of the local Fréedericksz effect was analyzed in terms of the relaxation time τ. However, for the general pattern, it is also of importance to know the factors determining the thickness W of the subsurface region where the most pronounced change in the orientation of molecules takes place. As seen from the table, W (in contrast to τ) is almost independent of the thickness d. This implies that the W value depends on the bulk properties of the liquid crystal studied. Since W is a characteristic of the electric double layer, it is natural to compare this value to the Debye screening length given by the formula

$$W_D = \left(\frac{\varepsilon_\perp \varepsilon_0 kT}{e^2 n_i}\right)^{1/2}, \qquad (3)$$

where $\varepsilon_\perp$ is the dielectric permittivity for a planar orientation, ε_0 is the permittivity of vacuum, k is the Boltzmann constant, e is the electron charge, and n_i is the ion concentration. For a 5TsB liquid crystal studied previously ($T = 294$ K; $\varepsilon_\perp = 5.2$; $n_i = 2.3 \times 10^{20}$ m^{-3}) [1], the Debye screening length is $W_D = 0.18$ μm, which is almost equal to $W = 0.21$ μm.

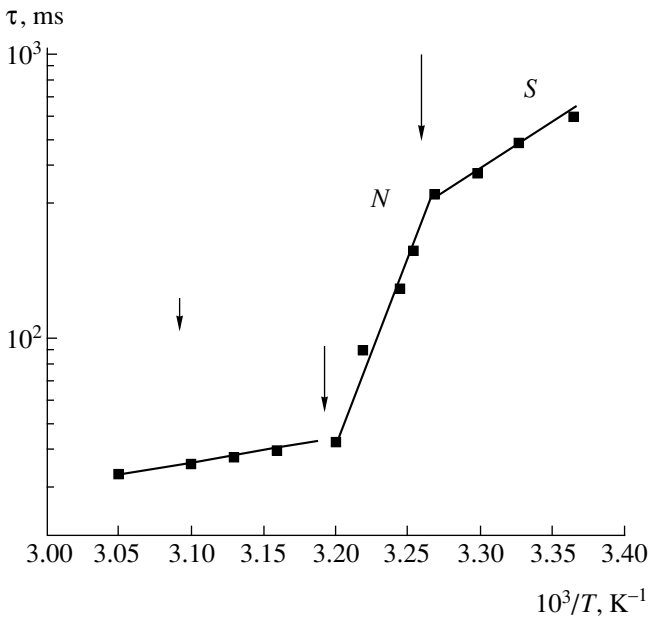

The plot of relaxation time τ versus inverse temperature for an 8TsB liquid crystal sample with a thickness of 18 μm. Arrows indicate the temperatures of phase transitions.

Thus, an ac voltage with an amplitude below the threshold value applied to plane-oriented nematic liquid crystal gives rise to local changes in the orientation of molecules in a near-electrode layer with a thickness equal to the Debye screening length. The frequency of these local changes (oscillations) is determined by one of the harmonics of relaxation of the weakly deformed director, which corresponds to the characteristic time of the field redistribution between the bulk and near-electrode regions of the sample.

Acknowledgments. The work was supported by the STCU grant no. 637.

REFERENCES

1. A. V. Koval'chuk, Pis'ma Zh. Tekh. Fiz. **26** (13), 41 (2000) [Tech. Phys. Lett. **26**, 559 (2000)].
2. O. V. Koval'chuk, Ukr. Fiz. Zh. **41** (10), 991 (1996).
3. L. M. Blinov, *Electrooptical and Magnetooptical Properties of Liquid Crystals* (Nauka, Moscow, 1978; Wiley, New York, 1983).

Translated by P. Pozdeev

Technical Physics Letters, Vol. 27, No. 3, 2001, pp. 204–206. Translated from Pis'ma v Zhurnal Tekhnicheskoĭ Fiziki, Vol. 27, No. 5, 2001, pp. 66–71.

Charging Capacity of a Sharp *p–n* Junction in a Variband Semiconductor

B. S. Sokolovskiĭ

Lviv State University, Lviv, Ukraine

Received July 3, 2000

Abstract—The barrier capacitance of a sharp *p–n* junction in a variband semiconductor with coordinate-independent bandgap gradient and electron affinity was calculated. It is shown that the square inverse barrier capacitance is a linear function of the applied voltage and that the cutoff voltage may significantly exceed the contact potential difference. © *2001 MAIK "Nauka/Interperiodica".*

Variband structures based on semiconductor solid solutions (primarily, of the $A^{III}B^{V}$ type) are widely used in semiconductor electronics, for example, in high-efficiency solar energy converters, selective and wideband photodetectors, tunable lasers with low threshold current, etc. [1, 2]. In recent years, growing attention of researchers has been devoted to Si–Ge variband heterojunctions, which are promising structures for creating fast- response integrated circuits [3]. In view of the increasing use of variband heterojunctions, it is important to develop new methods for determining the parameters of these structures and justify the applicability of techniques, such as the capacitance–voltage measurements, conventionally used for the characterization of homoband *p–n* structures.

The results of the capacitance–voltage (*C–V*) measurements for *p–n* junctions formed in a variband semiconductor are usually interpreted (see, e.g., [4, 5]) using relationships originally derived for the homoband *p–n* junctions [6]. This approach can be justified when the variband region is situated inside a space charge region, in which the electric field strength is zero [7]. In the general case, the correct description must take into account a possible effect of the variband region (extending outside the space charge region and giving rise to an electric field in the quasineutral base regions [8, 9]) on the *C–V* characteristics of the variband *p–n* structures. Thus, calculation of the charging capacity of a sharp *p–n* junction created in a variband semiconductor presents an important task.

A spatial distribution of the electrostatic potential φ in the space charge region ($-d_n \le x \le d_p$) of a sharp *p–n* junction built into a variband semiconductor is described within the framework of a model of completely depleted contact layer:

$$\frac{d^2\varphi}{dx^2} = -\frac{e}{\varepsilon\varepsilon_0}[N_d\theta(-x) - N_a\theta(x)], \quad (1)$$

where ε is the dielectric permittivity of the variband semiconductor, which will be assumed independent of the coordinate; ε_0 is the dielectric constant; N_a and N_d are the acceptor and donor concentrations in the *p* and *n* regions of the structure, respectively; θ is the unit function ($\theta(z) = 0$ for $z < 0$, $\theta(z) = 1$ for $z \ge 0$).

In order to formulate the boundary conditions for Eq. (1), we will take into account that the Fermi level position E_F in the *p* and *n* regions of a variband *p–n* structure is determined by the following relationships [8]:

$$E_F = -e\varphi - E_g - \chi + \xi_p, \quad (2)$$

$$E_F = -e\varphi - \chi + \xi_n, \quad (3)$$

where χ is the electron affinity; E_g is the forbidden band width; and ξ_p and ξ_n are the chemical potentials of electrons and holes in the *p* and *n* regions of the variband structure, respectively. In the case of a homogeneous doping, ξ_p and ξ_n in the quasineutral regions are independent of the coordinate. This implies that the Fermi level is parallel to edges of the energy bands of majority carriers [8–10]. In this case, Eqs. (2) and (3) readily yield expressions for the electric field strength in the base regions of the variband *p–n* structure and, in particular, the conditions on the boundaries of the space charge region:

$$\left.\frac{d\varphi}{dx}\right|_{x=-d_n} = -\frac{1}{e}\left.\frac{d\chi}{dx}\right|_{x=-d_n}, \quad (4)$$

$$\left.\frac{d\varphi}{dx}\right|_{x=d_p} = -\frac{1}{e}\left.\left(\frac{d\chi}{dx} + \frac{dE_g}{dx}\right)\right|_{x=d_p}. \quad (5)$$

In what follows, we will restrict the consideration to the case of a variband semiconductor with $E_g(x)$ and $\chi(x)$ described by linear functions of the coordinate. Introducing the notation

$$\alpha = \frac{1}{e}\frac{dE_g}{dx}, \quad \beta = \frac{1}{e}\frac{d\chi}{dx}, \quad (6)$$

taking $\varphi = 0$ for $x = 0$, and using Eqs. (1), (4), and (5) we obtain

$$\varphi(x) = -\frac{eN_d}{2\varepsilon\varepsilon_0}x_2 - \left(\frac{eN_d d_n}{\varepsilon\varepsilon_0} + \beta\right)x \quad \text{at} \quad -d_n \le x \le 0, \tag{7}$$

$$\varphi(x) = \frac{eN_a}{2\varepsilon\varepsilon_0}x^2 - \left(\frac{eN_a d_p}{\varepsilon\varepsilon_0} + \alpha + \beta\right)x \quad \text{at} \quad 0 \le x \le d_p. \tag{8}$$

The total voltage drop $\varphi(-d_n) - \varphi(-d_p)$ across the *p–n* junction is a sum of the source voltage U ($U < 0$ for reverse bias) and the contact potential difference U_c. The contact potential difference is equal to the difference of the thermoelectron work functions per unit charge at the boundaries of the space charge region:

$$U_c = U_{c0} + \alpha d_{p0} + \beta(d_{n0} + d_{p0}), \tag{9}$$

where $U_{c0} = (kT/e)\ln(N_a N_d / n_{i0}^2)$; n_{i0} is the intrinsic carrier concentration at $x = 0$; and d_{n0}, d_{p0} are the d_n, d_p values for $U = 0$. Using Eqs. (7)–(9), we obtain

$$U_c - U = U_n + U_p = \frac{eN_d}{2\varepsilon\varepsilon_0}d_n^2 + \frac{eN_a}{2\varepsilon\varepsilon_0}d_p^2 + \alpha d_p + \beta(d_n + d_p), \tag{10}$$

where $U_n = \varphi(-d_n)$ and $U_p = -\varphi(d_p)$ are the voltage drops across the parts of the space charge region situated in the *p* and *n* regions, respectively.

Using the condition of continuity for the electric field strength at $x = 0$, we obtain a relationship between thicknesses d_n and d_p of the space charge layers:

$$d_n N_d = d_p N_a + \frac{\varepsilon\varepsilon_0}{e}\alpha. \tag{11}$$

As is seen from this relationship, the space charges $q_n = eN_d d_n$ and $q_p = eN_a d_p$ in the regions adjacent to a metallurgical boundary of the *p–n* junction are not equal (in contrast to the case of a homoband structure) in absolute values; electroneutrality of the whole system is provided by space charges localized at the contacts [9].

Expressions (10) and (11) yield

$$d_p = \frac{\varepsilon\varepsilon_0}{eN_a}\left[\sqrt{\frac{2e\bar{N}}{\varepsilon\varepsilon_0}(U_c + U_\nabla - U)} - \alpha - \beta\right], \tag{12}$$

$$d_n = \frac{\varepsilon\varepsilon_0}{eN_d}\left[\sqrt{\frac{2e\bar{N}}{\varepsilon\varepsilon_0}(U_c + U_\nabla - U)} - \beta\right], \tag{13}$$

where

$$\bar{N} = \frac{N_a N_d}{N_a + N_d}, \quad U_\nabla = \frac{\varepsilon\varepsilon_0}{2e}\left[\frac{(\alpha+\beta)^2}{N_a} + \frac{\alpha^2}{N_d}\right]. \tag{14}$$

Using Eqs. (9), (12), and (13), we obtain the following expression for the contact potential difference of a variband *p–n* junction:

$$U_c = U_{c0} - 2U_\nabla + \frac{eK^2\bar{N}}{\varepsilon\varepsilon_0} + K\sqrt{\frac{2e\bar{N}}{\varepsilon\varepsilon_0}\left(U_{c0} - U_\nabla + \frac{eK^2\bar{N}}{2\varepsilon\varepsilon_0}\right)}, \tag{15}$$

where $K = (\varepsilon\varepsilon_0/e)[(\alpha+\beta)/N_a + \beta/N_d]$.

It follows from Eqs. (12)–(15) that the effect of internal electric fields (arising in the quasineutral base regions as a result of the spatial inhomogeneity of E_g and χ) on the size of the space charge regions determining the "geometric" capacitance of the *p–n* structure depends on the orientation of these fields. When the vectors of the internal electric fields are directed toward the metallurgical boundary (which takes place for $\alpha + \beta < 0$ in the *p* region and for $\beta < 0$ in the *n* region), the space charge region expands in both parts of the *p–n* structure because the majority charge carriers are pushed by the field out of the base regions.

In the opposite case (i.e., for $\alpha + \beta > 0$ in the *p* region and for $\beta > 0$ in the *n* region), the d_n and d_p values decrease because the internal electric fields counteract the spatial redistribution of charge carriers. Apparently, the case when the signs of $\alpha + \beta$ and β are opposite corresponds to antiphase modulation of the space charge region dimensions in the *p* and *n* parts of the base, whereby the space charge region decreases on one side of the metallurgical boundary of the *p–n* junction and increases on the other side of this boundary.

Once the dependence of the d_n and d_p values on the applied voltage is known, we may calculate the capacitance per unit area for the *p–n* junction considered as a combination of capacitances of the space charge layers in the *p* and *n* regions connected in series:

$$\frac{1}{C} = \frac{dU_n}{dq_n} + \frac{dU_p}{d|q_p|}. \tag{16}$$

Taking into account Eqs. (7), (8), and (10), this expression can be rewritten as

$$\frac{1}{C} = \frac{d_n + d_p}{\varepsilon\varepsilon_0} + \frac{1}{eN_a}(\alpha + \beta) + \frac{1}{eN_d}\beta, \tag{17}$$

which shows that the capacitance of the variband structure contains, in addition to the usual "geometric" terms, the contributions due to internal electric fields in the base regions. Substituting expressions (12) and (13) into Eq. (17), we obtain a formula for the capacitance of a sharp *p–n* junction in a variband semiconductor:

$$C = \left[\frac{2}{e\varepsilon\varepsilon_0\bar{N}}(U_c + U_\nabla - U)\right]^{-1/2}. \tag{18}$$

Note that, in a particular case of $\alpha = \beta = 0$, this formula converts into a well-known expression for the capacitance of a homoband *p–n* junction [6].

Formula (18) shows that the square inverse barrier capacitance of a sharp variband *p–n* junction is a linear function of the applied voltage. The slope of this dependence is determined by the same expression as that for a sharp *p–n* junction with homogeneous base regions [6]. On the other hand, there is an important difference between the cases of sharp homo- and variband *p–n* junctions: the presence of internal electric fields in the quasineutral base regions leads to a decrease in the barrier capacitance of the *p–n* junction, which is manifested by a decrease in the cutoff voltage on the *C–V* characteristic.

Taking into account that the term U_∇ depends on the E_g and χ gradients as described by expressions (14), we may conclude that the cutoff voltage significantly exceeds the contact potential difference when the variation of E_g and χ within the Debye screening length is markedly greater than kT (i.e., when the E_g and ξ gradients are sufficiently large). Taking for example $\varepsilon = 10$, $N_a = N_d = 10^{17}$ cm^{-3}, and $\alpha = \beta = 10^2$ eV/cm, we obtain $U_\nabla = 1.4 \times 10^{-6}$ V, while $\alpha = \beta = 5 \times 10^4$ eV/cm yields $U_\nabla = 0.35$ V. Apparently, the relative excess of the cutoff voltage over the contact potential difference for the given N_a, N_d, α, and β values is more significantly manifested for a smaller bandgap width at the metallurgical boundary of the *p–n* junction.

In conclusion, it should be noted that the above expression for the barrier capacitance of a variband *p–n* junction indicates a principal possibility to use the *C–V* characteristic for determining the electron affinity gradient—an important parameter of variband semiconductors which, in contrast to the bandgap width gradient, cannot be determined from the results of luminescent or photoelectric measurements [11].

REFERENCES

1. Zh. I. Alferov, Fiz. Tekh. Poluprovodn. (St. Petersburg) **32** (1), 3 (1998) [Semiconductors **32**, 1 (1998)].
2. V. M. Andreev, Fiz. Tekh. Poluprovodn. (St. Petersburg) **33** (9), 1035 (1999) [Semiconductors **33**, 942 (1999)].
3. H. G. Grimmeiss, Fiz. Tekh. Poluprovodn. (St. Petersburg) **33** (9), 1032 (1999) [Semiconductors **33**, 939 (1999)].
4. A. N. Imenkov, T. P. Lideĭkis, B. V. Tsarenkov, *et al.*, Fiz. Tekh. Poluprovodn. (Leningrad) **10** (7), 1260 (1976) [Sov. Phys. Semicond. **10**, 748 (1976)].
5. V. I. Stafeev, E. S. Banin, T. F. Terekhovich, *et al.*, Fiz. Tekh. Poluprovodn. (Leningrad) **12** (9), 1723 (1978) [Sov. Phys. Semicond. **12**, 1020 (1978)].
6. S. Sze, *Physics of Semiconductor Devices* (Wiley, New York, 1981; Mir, Moscow, 1984), Vol. 1.
7. B. Halil and K. C. Kao, Int. J. Electron. **33** (1), 33 (1972).
8. O. V. Konstantinov and G. V. Tsarenkov, Fiz. Tekh. Poluprovodn. (Leningrad) **10** (4), 720 (1976) [Sov. Phys. Semicond. **10**, 427 (1976)].
9. B. S. Sokolovskiĭ, Ukr. Fiz. Zh. **39** (3–4), 327 (1994).
10. B. S. Sokolovskii, Phys. Status Solidi A **163** (2), 425 (1997).
11. G. P. Peka, V. F. Kovalenko, and A. N. Smolyar, *Variband Semiconductors* (Vyshcha Shkola, Kiev, 1989).

Translated by P. Pozdeev

Technical Physics Letters, Vol. 27, No. 3, 2001, pp. 207–208. Translated from Pis'ma v Zhurnal Tekhnicheskoĭ Fiziki, Vol. 27, No. 5, 2001, pp. 72–75.

Correlated Electron Tunneling during the Field Electron Emission

V. I. Maslov

St. Petersburg State University of Telecommunications, St. Petersburg, Russia

Received September 28, 2000

Abstract—Elementary events of correlated electron tunneling from very small regions of a hollow metal emitter were detected. The most significant microscopic and macroscopic parameters favoring the appearance of multiparticle tunneling effects are considered. © *2001 MAIK "Nauka/Interperiodica".*

Previously, we have performed a correct systematic investigation of the field electron emission (FEE) in order to determine the distribution of elementary emission events with respect to multiplicity, that is, the FEE statistics [1, 2]. It was established with high precision (99.9%) that the FEE process in tungsten and niobium exhibits a one-electron character in the temperature interval from 4.2 to 300 K.

In recent years, considerable attention in the emission electronics and the physics of tunneling phenomena has been drawn to the problem of "point" emission sources [3, 4]. Therefore, obtaining new data on the correlation effects in FEE by direct experimental techniques is one of the most urgent tasks. In this context, we have performed a series of experiments to study the FEE statistics with an allowance for the dimensional effects.

In these experiments, the FEE statistics was gained from separate areas of the emitter surface with linear dimensions on the order of 25 Å, which is much smaller as compared to the previous studies, where the minimum size was 100 Å. The FEE projector magnification and the size of the emitter surface area studied were determined by measuring the distance between (112) and (121) faces on the anode, which corresponds to the point tip radius. The FEE measurements were performed as described elsewhere [2, 5] using tungsten and niobium point emitters prepared by electrochemical etching.

Processing and analysis of the experimental data showed the presence of time- and space-correlated groups of electrons tunneling into vacuum from the metal emitter surface. The multiparticle emission events were observed for an atomically clean cathode surface, the state of which was monitored using a cathode-luminescent glass situated on the anode. An electron beam emitted from (110) and (122) faces and their environment passed through a probing hole. The electron flux density (measured with a semiconductor detector) was varied from 100 to 3000 electrons per second. The measurements were carried out in a temperature range from 4.2 to 300 K at a residual gas pressure not exceeding 5×10^{-7} Pa. The detection method employed was sufficiently sensitive to reveal the groups including two, three, and four electrons.

Figure 1a shows a typical spectrum of multielectron emission statistics for a niobium at $T = 300$ K measured with an electron flux of 1400 s^{-1} using a diaphragm with a diameter of 25 μm. The relative fractions of a two-electron flux was 0.04, and that of the free-electron flux was 0.7×10^{-3} (which more than one order of magnitude greater than the Poisson superposition frequency). The sample temperature variation did not significantly modify the FEE statistics: the spectrum shape remained generally the same even when niobium passed to the superconducting state ($T = 4.2$ K). This is probably explained by the coherent length for niobium (4×10^{-6} cm) being large as compared to the probed area size.

The results of control experiments using a diaphragm with a diameter of 200 μm were similar to those reported previously [1, 2]. Figure 1b shows a typical spectrum of the FEE statistics measured under these conditions, in which the second peak intensity corresponds (within the experimental error) to the Poisson superposition frequency. The shapes of the curves presented in Figs. 1a and 1b are significantly different: the second peak in Fig. 1b has the form of a "step" typical of superpositions in a stationary regime, while the second peak in Fig. 1a has a nearly Gaussian shape. The difference can be explained by the fact that the correlation time for a group of two electrons is shorter than the working pulse duration in the spectrometer tract. The intensity of multiparticle emission drops (as a rule, by the geometric law) with increasing multiplicity of the elementary event.

For correct interpretation of the experimental results, it should be borne in mind that a fourfold decrease in the diaphragm diameter leads to a 16-fold decrease in the area studied, whereas the FEE current density increases 16 times under the same parameters of signal detection. Therefore, we must take into

1063-7850/01/2703-0207$21.00 © 2001 MAIK "Nauka/Interperiodica"

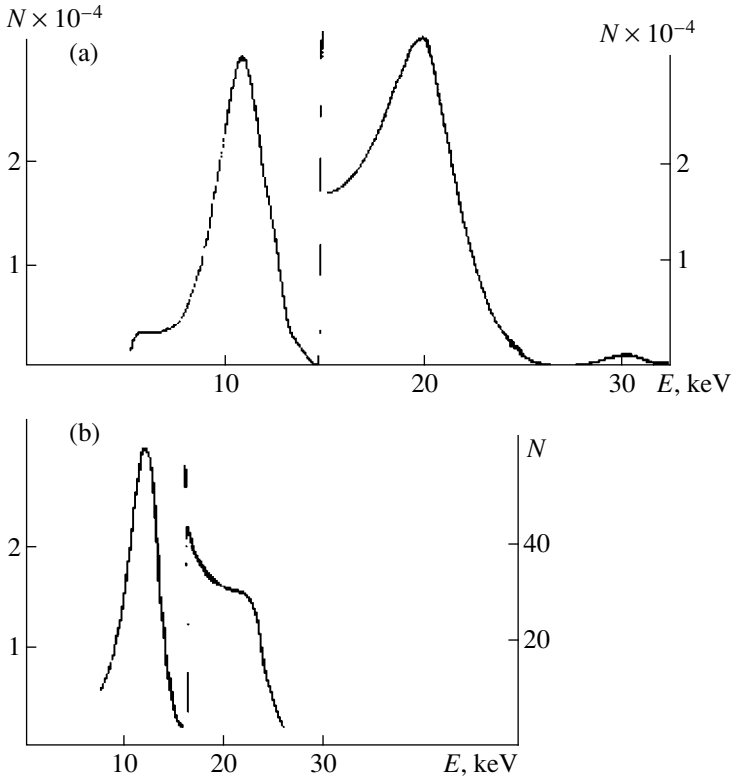

Fig. 1. The experimental spectra of FEE statistics in niobium measured using diaphragms with a diameter of (a) 25 μm and (b) 200 μm.

account both the dimensional effects and the phenomena depending on the FEE current density [5, 6]. For example, a fourfold decrease in the diaphragm diameter must increase the probability of observing the correlated emission effects in cooperative processes with a quadratic dependence on the current by two orders of magnitude. However, no such dependence on the current density was observed in our experiments. It should be noted that these results do not contradict the data reported in [7] where the FEE statistics was studied for much greater current densities and the time resolution was decreased in inverse proportion to the growing current density.

In considering the dimensional effects, it is necessary to take into account that the electron flux passing through a small hole (such as that used in our experiments) loses a considerable fraction of electrons emitted from the probed area with large initial tangential velocities. On the contrary, the relative fraction of electrons emitted with large tangential velocities from adjacent areas increases, which may lead to an optimum relationship between the area size and correlation length. This conclusion may be of special importance for our experiments, where the area size probed (25 Å) is approximately equal to the scattering circle diameter [8].

Thus, the hypothesis concerning manifestations of the coherent properties during the field electron emission is still working. A more consistent interpretation of the experimental data requires additional investigations.

REFERENCES

1. G. N. Furseĭ, N. V. Egorov, and A. V. Kocheryzhenkov, Pis'ma Zh. Tekh. Fiz. **7** (13), 798 (1981) [Sov. Tech. Phys. Lett. **7**, 343 (1981)].
2. G. N. Fursey, A. V. Kocheryzhenkov, and V. I. Maslov, Surf. Sci. **246**, 365 (1991).
3. H.-W. Fink, W. Stocker, and H. Schmid, Phys. Rev. Lett. **65** (10), 1204 (1990).
4. B. I. Vasichev and Yu. L. Rybakov, Zh. Tekh. Fiz. **59** (5), 56 (1989) [Sov. Phys. Tech. Phys. **34**, 532 (1989)].
5. V. I. Maslov, G. N. Furseĭ, A. V. Kocheryzhenkov, and N. P. Afanas'eva, Prib. Tekh. Éksp., No. 5, 133 (1987).
6. J. W. Cadzuk and E. W. Plummer, Phys. Rev. Lett. **26** (2), 92 (1971).
7. V. I. Maslov, G. N. Furseĭ, and A. V. Kocheryzhenkov, Zh. Tekh. Fiz. **59** (10), 164 (1989) [Sov. Phys. Tech. Phys. **34**, 1192 (1989)].
8. M. I. Elinson and G. F. Vasil'ev, *Autoelectron Emission* (Moscow, 1958), p. 272.

Translated by P. Pozdeev

Technical Physics Letters, Vol. 27, No. 3, 2001, pp. 209–210. Translated from Pis'ma v Zhurnal Tekhnicheskoĭ Fiziki, Vol. 27, No. 5, 2001, pp. 76–80.

The Clusterization Parameters of Neon, Argon, Krypton, and Xenon Calculated Using Their *P–V* Diagrams

P. E. L'vov and V. V. Svetukhin

Ul'yanovsk State University, Ul'yanovsk, Russia

Received July 13, 2000

Abstract—The parameters of clusterization for neon, argon, krypton, and xenon were calculated based on a thermodynamic analysis of the corresponding *P–V* diagrams. The calculated clusterization parameters agree well with experimental values of the evaporation heat. © *2001 MAIK "Nauka/Interperiodica".*

Introduction. In recent years, considerable attention of researchers has been paid to the process of cluster formation [1, 2]. The main task of determining the energy of atoms in a cluster is usually solved by method of molecular dynamics [3]. Previously [4], we derived an equation of state for a real gas with an allowance for the clusterization process. Using this equation of state, it is possible to calculate the clusterization parameters for real gases proceeding from analysis of the experimental phase diagrams.

In this paper, the clusterization parameters for neon, argon, krypton, and xenon are calculated based on a thermodynamic analysis of the corresponding experimental isothermal *P–V* diagrams. In contrast to the approach used in [4], we will also take into account the entropy factor and a relationship between the cluster surface energy and the interparticle interaction energy established in [5].

Principal computational formulas. Let us consider a lattice model of a gas featuring the cluster formation process. The system volume is modeled by the lattice with a large number of cells, where each cell is capable of accommodating only one particle. The free energy of such a system can be expressed as follows [4]:

$$F = \sum_i g_i N_i - kT \ln\left[\frac{N!}{(N-N')!\Pi_i N_i!(i!)^{N_i}} \prod_i P_i^{N_i}\right], \quad (1)$$

where N_i is the number of clusters composed of i particles, g_i is the energy of a cluster containing i particles, N is the total number of cells in the lattice, and N' is the total number of particles in the system. Note that not all rearrangements of particles in the lattice lead to the cluster formation, which is reflected by the cluster formation probabilities P_i in Eq. (1). Assuming that $N \gg N'$, the probability of formation of a cluster containing i particles can be taken equal to $P_i = 1/N^{i-1}$ (the clusters may form anywhere over the whole system).

Upon minimizing the free energy (1) with an allowance for the particle number conservation

$$N' = \sum_{i=1}^{N'} iN_i, \quad (2)$$

we arrive at the following expression for the number of clusters containing i particles [4]:

$$N_i = \frac{1}{i!N^{i-1}} \exp\left\{-\frac{g_i + \lambda i}{kT}\right\}, \quad N_1 = \exp\left\{-\frac{\lambda i}{kT}\right\}, \quad (3)$$

where λ is the Lagrange factor depending on the temperature and volume of the system, which is determined by solving Eq. (2). Using an expression for the free energy derived in [4] for $N \gg N'$, we obtain the following equation of state for the ideal gas with an allowance for the clusterization effect:

$$p = kT\frac{\sum_i N_i}{V}, \quad (4)$$

where V is the total volume of the system. Assuming that the clusters are closely packed, the energy of a cluster containing i particles at the zero energy can be written as [5]

$$g_i = -hi + \sigma i^{2/3}, \quad (5)$$

where h is the temperature-independent energy of an atom in the cluster, which is determine by the chemical bonds of this atom to the neighboring particles, while the second term reflects the presence of unsaturated (dangling) bonds on the cluster surface. Previously [5], it was demonstrated that close-packed clusters of inert gas atoms are characterized by $\sigma = 1.33h$.

Since the experimental *P–V* diagrams correspond to rather high temperatures, expression (5) should be modified by adding an entropy term related to the vibrations of atoms in the cluster. Assuming that the surface atoms in the cluster possess the same varia-

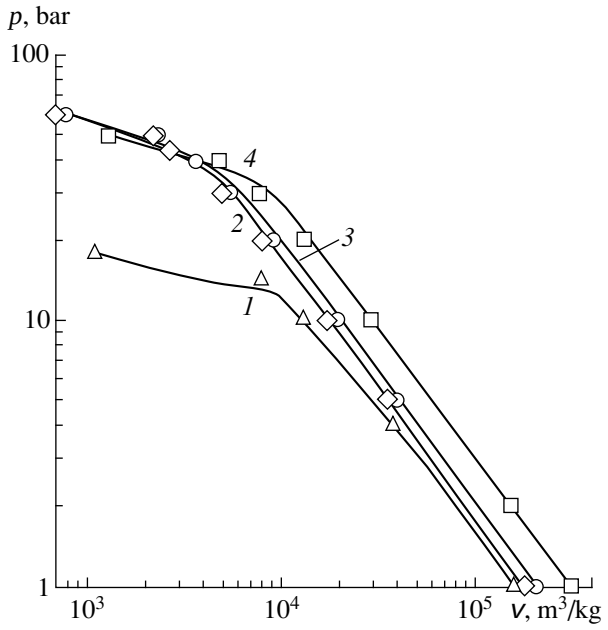

Fig. 1. Isotherms of inert gases: (*1*) Ne (T = 40 K); (*2*) Ar (T = 150 K); (*3*) Kr (T = 210 K); (*4*) Xe (T = 290 K); open symbols represent the experimental points [6], solid curves show the results of calculations.

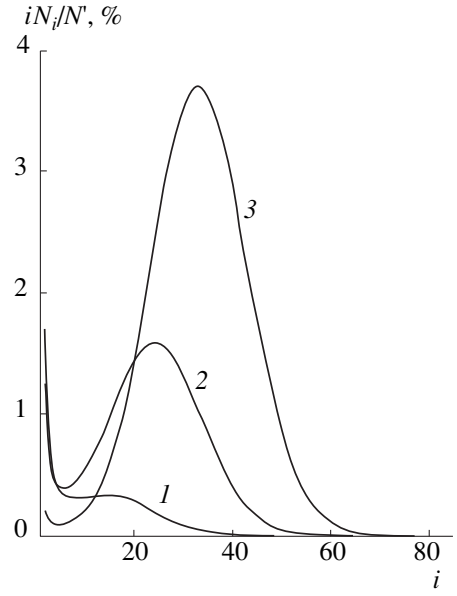

Fig. 2. Plots of the relative fraction of particles involved into clusters versus the cluster size (number of particles in the cluster) constructed for neon using various values of the specific gas volume v_{gas} = 38330 (*1*); 13110 (*2*); 7876 m^3/kg (*3*).

tional entropy s as the bulk ones, we obtain the following formula for the cluster energy

$$g_i = -(h - sT)i + 1.33hi^{2/3}, \quad i \gg 1. \qquad (6)$$

The number of cells in the system can be evaluated using the relationship [4]

$$N = \frac{v_{gas}}{v_{liq}} N', \qquad (7)$$

where v_{gas} and v_{liq} are the specific volumes of the liquid and gas phases, respectively.

Calculation of the clusterization parameters for Ne, Ar, Kr, and Xe. The inert gases were modeled by Eqs. (2), (3), (4), and (6), with the parameters h and s selected so as to provide for the best fit to the experimental data [6].

Typical results of modeling the isothermal phase diagrams of the systems studied are illustrated in Fig. 1. As seen, the theoretical curves describe the experimental patterns well. The calculated values of the clusterization parameters h and s, as well as the average evaporation heats ε_{av} per particle determined using the data from [3], are presented in the table. As seen from this table, there is a good agreement between the enthalpy h and the evaporation heat.

Clusterization parameters of inert gases

Gas	h, meV	s, k	ε_{av}, meV
Ne	23	–15.0	18
Ar	76	–15.3	68
Kr	100	–20.1	94
Xe	135	–15.5	131

Figure 2 shows plots of the relative fraction of particles involved into clusters versus the cluster size (number of particles in the cluster) constructed for neon using various values of the specific gas volume. The cluster size distributions obtained for the other gases also exhibited maxima in the regions of heavy fractions. The condition $i \gg 1$ is evidently obeyed in all cases, which confirms the validity of Eq. (6) for the free energy of a cluster.

Acknowledgments. This work was supported by the Russian Foundation for Basic Research, project nos. 00-01-00209 and 00-01-00283.

REFERENCES

1. B. M. Smirnov, Usp. Fiz. Nauk **167** (10), 1169 (1997) [Phys. Usp. **40**, 1117 (1997)].
2. Yu. B. Lozovik and E. A. Rakoch, Zh. Éksp. Teor. Fiz. **116** (6), 1903 (1999) [JETP **89**, 1089 (1999)].
3. B. M. Smirnov, Usp. Fiz. Nauk **162** (1), 119 (1992) [Sov. Phys. Usp. **35**, 37 (1992)].
4. P. E. L'vov and V. V. Svetukhin, Khim. Fiz. **13** (2), 93 (1999).
5. B. M. Smirnov, Usp. Fiz. Nauk **162** (12), 97 (1992) [Sov. Phys. Usp. **35**, 1052 (1992)].
6. *Thermophysical Properties of Ne, Ar, Kr, Xe* (Moscow, 1976).

Translated by P. Pozdeev

Technical Physics Letters, Vol. 27, No. 3, 2001, pp. 211–213. Translated from Pis'ma v Zhurnal Tekhnicheskoĭ Fiziki, Vol. 27, No. 5, 2001, pp. 81–86.

The Synthesis of a Biocomposite Based on Nickel Titanium and Hydroxyapatite under Selective Laser Sintering Conditions

I. V. Shishkovsky, E. Yu. Tarasova, L. V. Zhuravel', and A. L. Petrov

Lebedev Physical Institute (Samara Branch), Russian Academy of Sciences, Samara, Russia

e-mail: shiv@fian.samara.ru

Received September 29, 2000

Abstract—The conditions of synthesis of a nickel titanium based biocomposite material with hydroxyapatite added to the initial Ni–Ti powder mixture were studied. The material was obtained by a method based on the combination of laser-controlled selective sintering and self-propagating high-temperature synthesis. The data of X-ray diffraction and electron microscopy indicate that the high-rate laser heating induces the interaction of hydroxyapatite with nickel titanium, which results in the formation of additional intermetallic phases ($NiTi_2$, Ni_3Ti). © *2001 MAIK "Nauka/Interperiodica".*

Nickel titanium (NiTi) is a promising implant material for medical applications, which is due to a unique combination of properties (inherent even in the porous NiTi) including the shape memory effect, biocompatibility, high specific strength, and corrosion resistance [1]. Traditionally, NiTi is obtained either by multiple remelting in a vacuum-arc furnace or by self-propagating high-temperature synthesis (SHS) [2]. However, direct use of these methods for NiTi synthesis in medical implantology encounters considerable difficulties because of a cumbersome and multistage technological scheme involved in the fabrication of functional implants, which must possess preset individual shapes and dimensions.

A promising approach is offered by the Rapid Prototyping (or Solid Free Form Fabrication) technology based on the synthesis of material copies of three-dimensional (3D) objects (physical model and prototype parts) using their virtual models constructed by 3D computer-aided design (CAD) methods. This approach was already successfully used for the synthesis of implant models from UV-laser-cured oligomers by method of laser stereolithography based on the computer-aided processing of the X-ray, NMR, or ultrasonic tomography data [3]. It was suggested that the biocompatibility of these (generally, well tolerated by the living organism) oligomer models can be improved by doping the initial material or by coating the final articles with calcium phosphate–based compound—calcium hydroxyapatite $Ca_5(PO_4)_3OH$—which is well known and widely used in medicine for facilitating implantation and stabilizing the tissue osteogenesis [4].

Previously [5], we have succeeded for the first time with providing for an SHS reaction precisely within the laser spot during the layered selective laser sintering (SLS) process in Ni–Al and Ni–Ti powder systems for the intermetallic phase formation. The SLS process is one of the methods suited for the Rapid Prototyping technology, which can be used for the obtaining of both models and functional 3D articles from reactive powder mixtures. In particular, we have demonstrated [6] the possibility of NiTi synthesis by the SLS of powders in a protective Ar atmosphere, which opens wide prospects for the medical implantology.

In this work, we have used the X-ray diffraction and electron microscopy methods to study the conditions for NiTi synthesis by laser-controlled combined SLS–SHS process in a Ni–Ti powder mixture with hydroxyapatite additives. The process of furnace sintering in the pre-synthesized NiTi powder with hydroxyapatite was studied in [7]. It was found that a 2-h sintering at 800–1150°C led to the appearance of the products of hydroxyapatite decomposition in the form of calcium phosphates $Ca_4P_2O_9$ and $Ca_3(PO_4)_2$ and a number of other products including P_2O_5, CaO, $CaTiO_3$, Ti_3P, $NiTi_2$, Ni_3Ti, etc. Note that the former compounds retain biocompatibility (which requires that the Ca/P ratio would fall within 1.55–2.2 [4]), while the latter compounds are indicative of the interaction of hydroxyapatite (or the related decomposition products) with NiTi, which is accompanied by conversion of the latter. Our aim was to study how the hydroxyapatite additive and its decomposition products affect the SHS process of NiTi formation under the high-rate laser heating conditions.

The X-ray diffraction measurements were carried out on a DRON-2 diffractometer using Cu$K\alpha$ radiation. The electron-microscopic investigations were performed in an EMV-100V instrument operated at an accelerating voltage of 75 kV. The SLS process was

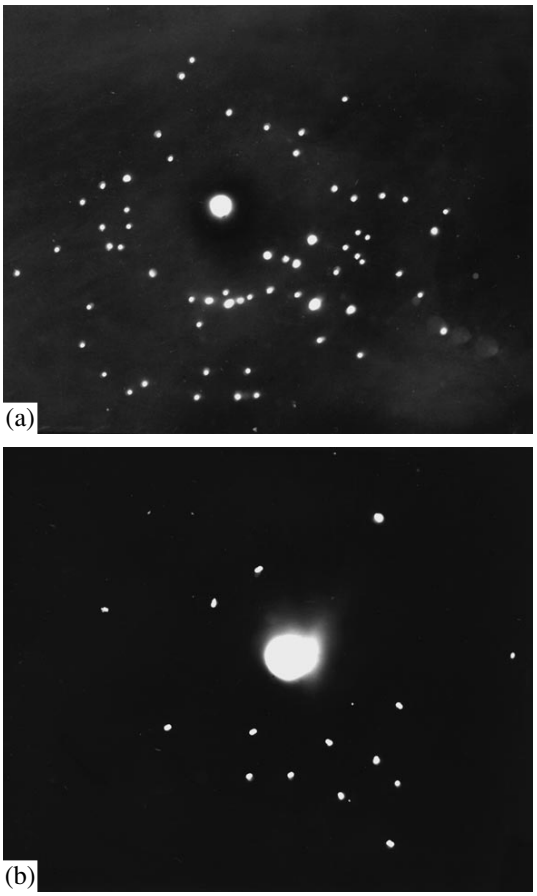

Fig. 1. Electron diffraction patterns from replicas of laser-sintered monolayers in regimes (a) 2 and (b) 3 (see table).

conducted in a protective Ar atmosphere as described in [5]. The experiments were carried out in a KVANT-60 setup (cw–YAG–Nd laser) using optimum laser action regimes for the Ni–Ti powder processing established previously [6].

Nickel titanium was synthesized from a mixture of powdered titanium (PTKh grade) and 55.06 wt % of powdered nickel (PGSR4 grade, State Standard GOST 9722-79 (%): 2.8–3.8 B, 0.6–1.0 C, 3.0–4.5 Si, 15–18 Cr, ≤5.0 Fe, 0.04 P, 0.04 S, balance Ni). Powdered hydroxyapatite (Gidroksiapol-GAP85d grade, Pharmacopoeial Clause VFS 42-2378-94) was added at a relative amount of 1/4 (w/w) to the Ni–Ti (PGSR4 + PTKh) mixture. Note that, while the Ni/Ti ratio in the system was strictly determined by stoichiometry of the final compound (NiTi), no data were available on the amount of hydroxyapatite necessary for realization of its pharmacological properties. For the comparison of data on the NiTi synthesis and on the effect of hydroxyapatite, we also studied the laser-controlled SLS–SHS process in a mixture of commercial NiTi powder (PN55T45 grade) with hydroxyapatite (4 : 1) and in the aforementioned compositions without hydroxyapatite additives.

The SLS process was effected in a free-poured volume of powder, which was markedly greater as compared to the thicknesses of sintered layers. The results of the X-ray diffraction analysis using the most intense reflections from the sintered material are summarized in the table for various laser radiant powers R (the scanning rate $v = 3.1$ cm/s and the laser spot size $d \sim 50$ μm were constant) and different powder mixtures. The table also gives data on the thickness D of sintered layers. An asterisk indicates the phases with overlapping reflections.

As is seen from data presented in the table, the high-rate laser heating (in contrast to the furnace processing) [7] is not accompanied by the formation of phases such as $Ca_4P_2O_9$, $Ca_3(PO_4)_2$, P_2O_5, CaO, $CaTiO_3$, Ti_3P, etc. This implies that hydroxyapatite exhibits no strong decomposition, while the $Ca(H_2PO_4)_2$ and $CaHPO_4$ phases are known to retain the pharmacological properties of hydroxyapatite [4]. Oxygen and phosphorus liberated during heating react with NiTi to form $NiTiO_3$ and NiP_2. The presence of hydroxyapatite as such detrimentally affects the conditions of NiTi synthesis (cf. regime 6 versus 1 and 2 in the table). The process in a hydroxyapatite mixture with commercial NiTi powder (regimes 3 and 4) proceeds under conditions favoring the synthesis of other

Phase compositions (by X-ray diffraction data) of the products obtained by the laser-controlled SLS–SHS process in powdered mixtures of Ti (PTKh grade), Ni (PGSR4 grade), NiTi (PN55T45 grade) and hydroxyapatite (HAP)

Regime	Initial powder composition	P, W	D, mm	Product phase composition
1	PGSR4 + PTKh + HAP	23	2.0	33% HAP, 23% Ni_2P(*Ni_5P_2), 16% Ni_3Ti, 14% $CaHPO_4$, 14% $NiTi_2$
2	PGSR4 + PTKh + HAP	13	1.8	34% HAP, 14% Ni_3Ti, 14% NiTi, 22% $NiTi_2$, 17% TiO_2
3	PN55T45 + HAP	23	2.8	9.5% HAP, 18% $NiTiO_3$(?Ni_3Ti), 8% NiTi, 56% $NiTi_2$, 8.5% Ni_2Ti_4O
4	PN55T45 + HAP	13	1.4	40% $NiTi_2$, 16% $Ca(H_2PO_4)_2$, 13% $NiTiO_3$(*Ni_3Ti), 15% $CaHPO_4$, 13% NiP_2
5	PN55T45	13	Layers break	46% $NiTi_2$, 29% $NiTiO_3$(*Ni_3Ti), 25% Ni_3Ti(*NiTi)
6	PGSR4 + PTKh	13		50% NiTi, 29% Ni, 21% Ti

intermetallic phases ($NiTi_2$, Ni_3Ti); the higher the laser power, the more favorable are these conditions.

The electron-microscopic investigation of a thin layer of the sintered powder composition deposited onto a structureless carbon replica made it possible to determine the percentage phase composition of the sintered material with greater precision. Figures 1a and 1b show the electron diffraction patterns for the samples sintered in regimes 2 and 3 (see table). An analysis of these results confirmed the general conclusions based on the X-ray diffraction data. In Fig. 1a, the interplanar spacings correspond predominantly to hydroxyapatite and the $CaHPO_4$, $NiTiO_3$, $NiTi_2$, and Ni_3Ti phases, while Fig. 1b confirmed the presence of hydroxyapatite, $NiTi_2$, and Ni_3Ti phases. Taking into account the experimental results reported in [7], we may suggest that the furnace processing of these sintered articles would not alter this situation.

Thus, we have demonstrated the possibility of synthesis of a biocompatible composite based on nickel titanium by method of laser-controlled combined SLS–SHS processing of a Ni–Ti powder mixture with hydroxyapatite additives. The yield of nickel titanium from the selective laser-controlled reaction in a Ni–Ti–hydroxyapatite powder mixture is higher than the yield of a process involving laser sintering of nickel titanium with hydroxyapatite.

REFERENCES

1. V. É. Gyunter, V. V. Kotenko, V. K. Polenichkin, and V. I. Itin, Izv. Vyssh. Uchebn. Zaved., Fiz., No. 5, 127 (1985).
2. V. N. Itin and Yu. S. Naĭborodenko, *High-Temperature Synthesis of Intermetallic Compounds* (Tomsk Univ., Tomsk, 1989).
3. E. N. Antonov, A. V. Evseev, M. A. Markov, *et al.*, Opt. Tekh. **13** (1), 55 (1998).
4. S. Langstaff, M. Bayer, T. J. N. Smith, *et al.*, Biomaterials **20**, 1727 (1999).
5. I. V. Shishkovsky, A. G. Makarenko, and A. L. Petrov, Fiz. Goreniya Vzryva **35** (2), 59 (1999).
6. I. V. Shishkovsky, D. M. Gureev, and A. L. Petrov, Izv. Ross. Akad. Nauk, Ser. Fiz. **63** (10), 2077 (1999).
7. N. A. Shevchenko, V. I. Itin, A. A. Tukhfatullin, *et al.*, Pis'ma Zh. Tekh. Fiz. **24** (24), 41 (1998) [Tech. Phys. Lett. **24**, 964 (1998)].

Translated by P. Pozdeev

Technical Physics Letters, Vol. 27, No. 3, 2001, pp. 214–216. Translated from Pis'ma v Zhurnal Tekhnicheskoĭ Fiziki, Vol. 27, No. 5, 2001, pp. 87–94.

Nondestructive Laser-Induced Plasma Formation at a Target Surface

M. A. Yakovlev

Moscow State Technical University, Moscow, Russia

e-mail: yakovlev@mx.bmstu.ru

Received in final form September 21, 2000

Abstract—The parameters of ultrashort laser pulses and the thermal characteristics of a metal target were determined, which provide that the laser-induced plasma formation at the target surface does not lead to damage of the metal surface. The results of calculations are compared to experimental data. © *2001 MAIK "Nauka/Interperiodica".*

Problems related to the interaction of ultrashort high-power laser pulses with metal targets attract the considerable attention of researchers engaged in the development of high-speed laser technologies, where the laser processing involves an extremely rapid energy introduction into a target substance (pico- and femtosecond time scale). The character of this interaction is largely determined, besides the spectral characteristics, by the intensity and duration of laser pulses. As was noted in [1], the absorption of laser radiation results in violation of the thermodynamic equilibrium between the electron gas and crystal lattice at the metal target surface. Since the heat capacity of the degenerate electron gas is very small, the electron temperature follows the laser pulse shape virtually without delay. The lattice heating proceeds at a markedly slower rate because of a considerable difference between electron and ion masses. For a laser radiant power density of $I_{em} \sim 10^{14}$ W/m^2, the time of lattice heating for various metals varies within ~1–100 ps [2, 3], which implies that the energy deposited with a subpicosecond laser pulse is stored in the electron subsystem, while the lattice is heated to a markedly lower temperature.

An important problem consists in determining the conditions for which the ultrashort laser pulse action, while changing the physical properties of a material, does not lead to destruction of the target, that is, for which it does not stimulate developed evaporation (ablation) processes. It was demonstrated [2, 4] that there is a threshold value of the energy density F_{abl} of an ultrashort laser pulse (the pulse duration τ_p must be much shorter compared to τ_{el}, the time of relaxation of the electron and lattice temperatures) that leads to the onset of material ablation after termination of the laser pulse action.

Previously [6, 7], we studied the possibility of breakdown in a dense inert gas layer near a metal surface under the action of ultrashort laser pulses in the absence of vapors of the target material. It was demonstrated that, due to the ionizing effect of the surface thermoelectron layer [7], the near-surface gas layer may exhibit a breakdown even during a picosecond laser pulse, provided that the laser pulse intensity and the gas pressure obey definite conditions. However, the subsequent state of the target surface was not considered.

The purpose of this study was to determine the conditions under which ultrashort laser pulses can produce ionization of a dense inert gas layer without destruction of the target surface upon termination of the laser pulse action. These conditions can be formulated as $\tilde{I}_{em}(P)\tau_s \le F_{\text{abl}}$, where $\tilde{I}_{em}(P)$ is the threshold laser intensity necessary to produce a breakdown of the gas at a pressure P and τ_s is the time of formation of a near-surface plasma with a critical density ensuring complete screening of the target surface.

In order to solve the above task, it is necessary to consider (in more detail than in [7]) a physical mechanism of the surface thermoelectron layer formation and to determine the laser radiation parameters and the target material characteristics for which this surface electron layer (SEL) can significantly influence the laser-affected surface processes. The main factor determining the SEL formation at a metal target surface under the action of ultrashort laser pulses is a considerable difference between the electron and lattice (~eV) temperatures, which leads to a a sharp increase in the thermoemission current and the formation of a sufficiently extended negative space charge region near the target [8].

As is known, the electric double layer exists at a metal surface even under conditions of the thermodynamic equilibrium between the electron and lattice subsystems. However, the electron gas under these conditions is degenerate and the electron density very rapidly decays with the distance from the surface: $n_e \propto z^{-2}\exp(-\beta z)$, where β^{-1} is a value on the order of an average interelectron distance in a metal [9]. This circumstance allows us to consider the degenerate SEL

1063-7850/01/2703-0214$21.00

thickness as insignificant and to ignore the effect of this layer on the laser radiation transmission to the metal. With a rapid drop in the electron density, the degree of degeneracy decreases and (for the Fermi energy $E_F(n_e)$ on the order of kT) the electron system passes to the classical sate. The further decrease in the electron density obeys a more sloping law [7]:

$$n_e(z) = n_0\left(1 + \frac{z}{\sqrt{2}D}\right)^{-2}, \quad (1)$$

where $D = (\varepsilon_0 kT/e^2 n_0)^{1/2}$ is the Debye screening radius and n_0 is the boundary electron density determined from the degeneracy condition $E_F(n_0) \simeq kT$, which yields $n_0 \propto T^{3/2}$. Thus, a growth of the electron temperature is accompanied by the increase in the size of SEL where the electron density decreases as descried by expression (1). At the same time, the boundary electron density n_0 increases as well and, on reaching the electron temperatures on the order of E_F, all electrons in the SEL pass to the classical state. In this state, the electron distribution obeys Eq. (1) and the n_0 value is on the order of electron density in a metal. Therefore, an intense nonequilibrium heating of the electron component in a metal may result in the formation of a sufficiently thick and dense layer of seeding electrons.

Let us determine the parameters of a pulsed laser radiation for which a sufficiently dense nondegenerate SEL may form without destruction (ablation) of the metal target surface. Equations determining variation of the electron and lattice temperatures in a metal target under the action of a pulsed laser radiation can be written, by analogy with [2], in a one-dimensional form for the region $z < 0$ (metal):

$$C_e\frac{\partial T_e}{\partial t} = \frac{\partial}{\partial z}\left[\chi_e\frac{\partial T_e}{\partial z}\right] - \alpha(T_e - T_l) + Q,$$
$$C_l\frac{\partial T_l}{\partial t} = \frac{\partial}{\partial z}\left[\chi_l\frac{\partial T_l}{\partial z}\right] + \alpha(T_e - T_l), \quad (2)$$

where Q is the volume flux of energy supplied to the electron subsystem with the absorbed laser radiation; T_e and T_l are the electron and crystal lattice temperatures in the metal; C_e, C_l and χ_e, χ_l are the electron and lattice heat capacities and thermal conductivities, respectively; and α is the coefficient of heat exchange between electrons and lattice (for typical metals, $\alpha \sim 10^{16}$ W/(m^3 K) [2]).

According to [2], $Q \approx I_{em}/l$, where I_{em} is the laser pulse intensity and $l \sim \max[\delta, \sqrt{\chi\tau_p}]$ is the thickness of a metal layer heated during the laser pulse action (δ is the skin layer thickness and χ is the electron temperature conductivity). For a picosecond laser pulse, $l \sim 10^{-7}$ m; this implies that, during the laser pulse action, a difference between the electron subsystem and lattice temperatures according to Eq. (2) reaches $\Delta T \approx I_{em}/\alpha_l l$. Thus, a minimum intensity of the picosecond laser pulse necessary to remove degeneracy from the heated

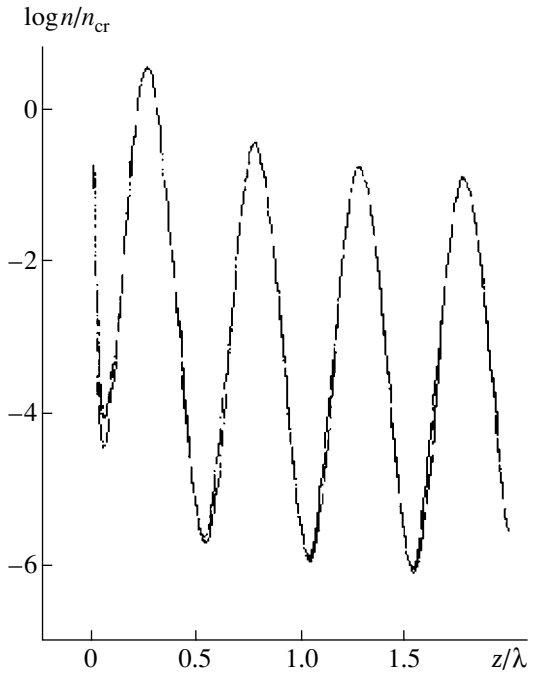

Fig. 1. Spatial distribution of the near-surface plasma density at the moment of complete target screening.

electron gas layer is $I_{em}^{\min} \approx \alpha_l l T_F \sim 10^{14}$ W/m^2 (T_F is the temperature of degeneracy of the electron subsystem).

According to [8], the action of picosecond laser pulses with the intensity $I_{em} \geq 3 \times 10^{13}$ W/m^2 upon the surface of typical metals is characterized by a thermoemission intensity exceeding the photoemission level. This implies that the SEL formation by a laser pulse with this intensity is caused by the thermoemission during $\tilde{\tau}_s \approx D/v_T \sim 10^{-14}$–$10^{-13}$ s, where v_T is the thermal velocity of electrons. In addition, it should be noted that the character of thermoemission under these conditions significantly differs from that of thermoemission from an electrode in a closed circuit. Indeed, the thermoemission in the case under consideration proceeds from an isolated metal surface, leaving an uncompensated positive charge on the surface and forming a negative space charge near this surface, which affects the thermoemission current. The interplay of these factors markedly complicates description of the process of SEL formation. However, taking into account that the time of formation of the space charge distribution ($\tilde{\tau}_s$) is much smaller than the picosecond laser pulse duration (τ_p), the charge distribution in SEL during the laser pulse action can be considered as stationary and characterized by the corresponding electron layer temperature.

The upper limiting intensity $I_{em}^{\max}$ corresponds to a subthreshold level leading to the onset of the target material melting and ablation. In the presence of sufficiently dense gas atmosphere at the metal target surface, the ionizing effect of SEL leads to the formation

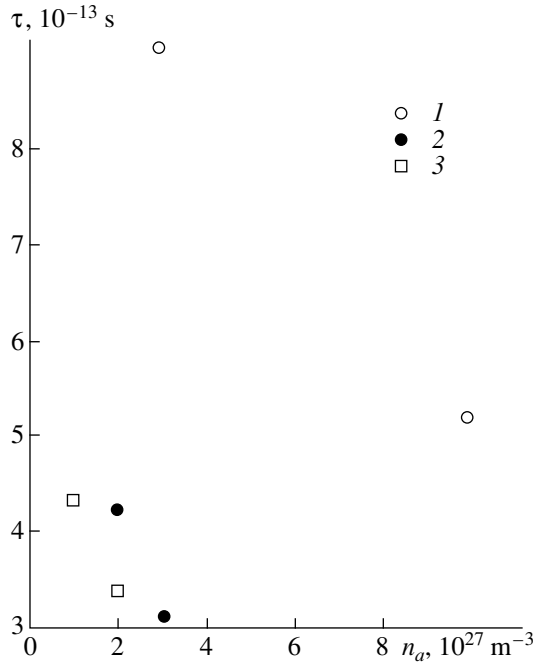

Fig. 2. A plot of the breakdown time versus near-surface gas concentration for $I_{em} = 1.1 \times 10^{16}$ (*1*), 2.5×10^{16} (*2*), and 4.4×10^{16} W/m^2 (*3*).

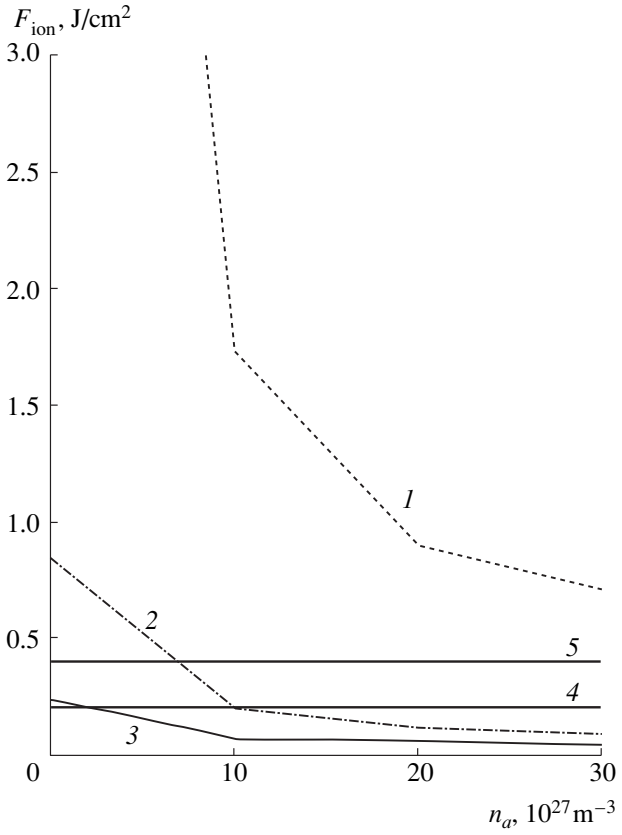

Fig. 3. Plots of the ionization threshold versus near-surface gas concentration for $I_{em} = 0.28 \times 10^{16}$ (*1*), 1.1×10^{16} (*2*), 2.5×10^{16} W/m^2 (*3*), $I_{em} = F_{abl}$ [3] (*4*), and $I_{em} = F_{abl}$ [5] (*5*).

of a near-surface layer of weakly ionized nonideal plasma during a picosecond laser pulse [6]. Figure 1 shows a typical spatial distribution of the near-surface plasma density at the moment of complete target screening ($\tau_s \approx 1.0$ ps for $I_{em} = 1.1 \times 10^{16}$ W/m^2 and $n_a = 3 \times 10^{27}$ m^{-3}). Figure 2 presents a plot of the breakdown time versus the near-surface gas concentration $\tau_I = \tau_I(I_{em}, n_a)(\tau_s \sim \tau_I)$.

Using the above results, it is possible to evaluate a threshold vale of the laser pulse ionization energy density $F_{ion} = I_{em}\tau_s$. A minimum value of the ionization threshold is $F_{ion} \approx 0.1$ J/cm^2 for $I_{em} = 2.5 \times 10^{16}$ W/m^2 and $n_a = 3 \times 10^{27}$ m^{-3} (Fig. 3). Under the conditions studied, this value can be lower than the ablation threshold [4, 2]. Experimental values of the ablation threshold at atmospheric pressure fall within $F_{abl} = 0.2$–0.5 J/cm^2 [3, 5]. As the near-surface gas pressure increases to 200–300 atm, the ablation threshold grows as well. Therefore, a regime with $F_{ion} < F_{abl}$ is possible, which implies that the dense near-surface gas layer can be ionized without damaging the condensed target surface.

It should be noted that a part of the laser radiation energy absorbed in the near-surface plasma (the temperature of the electron plasma component is ~10^4 K) and reirradiated toward the target surface is much smaller compared to the laser pulse energy. Taking this energy into consideration in determining the energy supplied by the laser pulse to the target does not affect the results of calculations.

Acknowledgments. The author is grateful to A.A. Rukhadze, A.M. Ignatov, and A.A. Samokhin for fruitful discussions and valuable remarks.

REFERENCES

1. S. I. Anisimov, A. M. Bonch-Bruevich, M. A. El'yashevich, *et al.*, Zh. Tekh. Fiz. **36**, 1273 (1966) [Sov. Phys. Tech. Phys. **11**, 945 (1966)].
2. S. I. Anisimov and B. Rethfeld, Izv. Akad. Nauk, Ser. Fiz. **61**, 1642 (1997).
3. D. Riley, A. J. Langley, P. F. Taday, *et al.*, J. Phys. D **31**, 515 (1998).
4. Yu. V. Afanas'ev, N. N. Demchenko, *et al.*, Izv. Akad. Nauk, Ser. Fiz. **63**, 667 (1999).
5. K. Sokolowski-Tinten, J. Bialkowski, A. Cavallery, *et al.*, Phys. Rev. Lett. **81**, 224 (1998).
6. A. V. Ivlev, M. A. Yakovlev, and A. N. Bordenyuk, Zh. Tekh. Fiz. **68** (8), 42 (1998) [Tech. Phys. **43**, 921 (1998)].
7. A. V. Ivlev, K. B. Pavlov, and M. A. Yakovlev, Zh. Tekh. Fiz. **64** (9), 50 (1994) [Tech. Phys. **39**, 888 (1994)].
8. S. I. Anisimov, B. L. Kapeliovich, and T. L. Perel'man, Zh. Éksp. Teor. Fiz. **66**, 776 (1974) [Sov. Phys. JETP **39**, 375 (1974)].
9. A. K. Gupta and K. S. Singwi, Phys. Rev. B **15**, 1801 (1977).

Translated by P. Pozdeev

Technical Physics Letters, Vol. 27, No. 3, 2001, pp. 217–219. Translated from Pis'ma v Zhurnal Tekhnicheskoĭ Fiziki, Vol. 27, No. 6, 2001, pp. 1–6.

On the Problem of the Existence of a Singular Stationary Profile for the Charged Surface of a Conducting Liquid

N. M. Zubarev

Institute of Electrophysics, Ural Division, Russian Academy of Sciences, Yekaterinburg, Russia

e-mail: nick@ami.uran.ru

Received August 30, 2000

Abstract—We will prove that, within the framework of planar geometry, no equilibrium configuration of a free charged surface of a conducting liquid can exist ensuring unlimited local amplification of the applied electric field. © *2001 MAIK "Nauka/Interperiodica".*

Both experimental data [1] and the results of numerical modeling [2, 3] indicate that the surface of a conducting liquid (e.g., molten metal) in a sufficiently strong electric field exhibits the formation of cusps in a finite time. These results pose an interesting question concerning the possibility of an equilibrium singular configuration existing for the free charged equipotential surface of a conducting liquid. A particular singular solution of a problem on the stationary boundary profile of such a liquid is offered by the Taylor cone [1]. However, the condition of force balance for the Taylor cone is broken at a singular point (apex), from which it follows that this solution provides only a possible asymptotic shape of the surface at a considerable distance from the apex.

Below we will demonstrate that, within the framework of planar geometry, no equilibrium configuration of a free charged surface of a conducting liquid can exist such that the induced electric field strength would be significantly greater than that of the external electric field E_0. The algorithm leading to this conclusion is as follows: assuming that the equilibrium cusp formation is possible, we will obtain a general solution to the equations describing the corresponding equilibrium surface shape, after which we will demonstrate that this solution cannot be physically realized.

A stationary profile of the surface of a conducting liquid (described by the unknown function η) is determined from the condition of force balance at the liquid boundary:

$$E^2/(8\pi) + \alpha K = E_0^2/(8\pi) + \rho g\eta, \quad y = \eta(x), \quad (1)$$

where $E = |\nabla\varphi|$ is the absolute value of the electric field strength, φ is the field potential, $K(x) = \eta_{xx}/(1 + \eta_x^2)^{3/2}$ is the surface curvature, α is the surface tension coefficient, g is the acceleration of gravity, and ρ is the liquid density. In the absence of space charge, the electric potential distribution is described by the Laplace equation

$$\varphi_{xx} + \varphi_{yy} = 0,$$

that has to be solved jointly with the conditions that (i) the surface of the conducting liquid is equipotential and (ii) the field at an infinite distance from the surface is uniform:

$$\varphi = 0, \quad y = \eta(x),$$

$$\varphi \longrightarrow -E_0 y, \quad y \longrightarrow \infty.$$

Let us consider the case of interest, whereby the field strength at the surface far exceeds the applied field value ($E \gg E_0$), which is characteristic of a surface possessing various sharp features (angles and cusps). In this case, the terms in the right-hand part of Eq. (1) can be ignored and the condition of equilibrium can be expressed in the following form:

$$E^2/(8\pi) + \alpha K = 0, \quad y = \eta(x).$$

Selecting E_0 as the unit of field strength and $8\pi\alpha E_0^{-2}$ as the unit of length, we obtain

$$E^2 - E_\varphi = 0, \quad y = \eta(x), \quad (2)$$

where it is taken into account that the curvature of the equipotential surface can be expressed via the field potential as $K = -|\nabla\varphi|_\varphi$ [4].

For the subsequent considerations, it is convenient to use the potential φ and the harmonic conjugate function ψ (such that the condition $\psi = \text{const}$ determines the electric field lines) as independent variables and to represent the unknown function in the form $f = \ln E$. This is a harmonic function of x and y [4] and, hence, of the new variables φ and ψ as well:

$$f_{\psi\psi} + f_{\varphi\varphi} = 0. \quad (3)$$

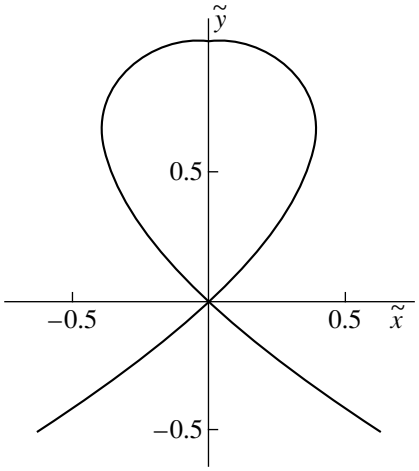

Figure.

The boundary condition (2) can be written as

$$f_\varphi = \exp f, \quad \varphi = 0. \tag{4}$$

Taking into account that $E \longrightarrow 1$ for $z \longrightarrow \infty$, we conclude that function f must decay at infinity:

$$f \longrightarrow 0, \quad \varphi \longrightarrow -\infty. \tag{5}$$

Thus, the initial boundary problem with an unknown boundary is transformed into the nonlinear boundary problem (3)–(5) on the halfplane $\varphi < 0$.

Using the known solution to the Laplace equation on the halfplane for the functions decaying at infinity, we may write

$$f(\psi, \varphi) = -\frac{1}{\pi}\int_{-\infty}^{+\infty} \frac{\varphi f(\psi', 0)}{(\psi' - \psi)^2 + \varphi^2} d\psi', \quad \varphi < 0.$$

Differentiating this expression with respect to ψ, we obtain the boundary condition

$$f_\varphi|_{\varphi = 0} = -\hat{H}\tilde{f}_\psi,$$

where $\tilde{f}(\psi) = f|_{\varphi = 0}$ and $\hat{H}$ is the Hilbert integral operator

$$\hat{H}\tilde{f} = \frac{1}{\pi}\text{V.P.}\int_{-\infty}^{+\infty} \frac{\tilde{f}(\psi')}{\psi' - \psi} d\psi'.$$

Using these relationships, we may exclude the derivative f_φ from Eq. (4) and reduce the two-dimensional boundary problem (3)– (5) to the following one-dimensional integrodifferential equation:

$$\hat{H}\tilde{f}_\psi = -\exp\tilde{f}.$$

Upon applying the Hilbert operator to both parts of this equation and taking into account that $\hat{H}^2 = -1$, we obtain

$$\tilde{E}_\psi = \tilde{E}\hat{H}\tilde{E}, \tag{6}$$

where $\tilde{E} = E|_{\varphi = 0} = \exp\tilde{f}$ is a function determining the absolute value of the electric field strength at the boundary of the conducting liquid. Thus, Eq. (6) describes the potential distribution at the equilibrium surface assuming that the induced field is markedly stronger than the applied field.

In order to solve Eq. (6), let us represent $\tilde{E}$ as the sum of two functions, $\tilde{E} = \tilde{E}^{(+)} + \tilde{E}^{(-)}$, which are analytical in the upper and lower halfplanes of the complex variable ψ, respectively. Substituting this expression into Eq. (6) and taking into account that $\hat{H}\tilde{E}^{(\pm)} = \pm i\tilde{E}^{(\pm)}$, we obtain a pair of ordinary differential equations

$$\tilde{E}_\psi^{(\pm)} = \pm i[\tilde{E}^{(\pm)}]^2.$$

A solution to these equations is given by the formula $\tilde{E}^{(\pm)} = \pm i/(\psi \pm iq)$, where q is a constant such that $\text{Re}q > 0$. Not loosing generality, we may assume this constant to be real. Then the solution to Eq. (6) takes the form

$$\tilde{E} = 2q/(\psi^2 + q^2). \tag{7}$$

Let us construct a surface corresponding to this solution. Note that the angle θ between the electric field vector and the abscissa axis is a harmonic conjugate to f [4]. Then, taking into account the Cauchy–Riemann condition ($\theta_\psi = f_\varphi$) and using Eq. (4), we obtain the following relationships for the surface $\varphi = 0$,

$$\tilde{\theta}_\psi = \exp\tilde{f} = \tilde{E},$$

where $\tilde{\theta} = \theta|_{\varphi = 0}$. Upon substituting formula (7) into this relationship and integrating the resulting equation with respect to ψ, we obtain an expression for the angle $\tilde{\theta}$:

$$\tilde{\theta} = \pi/2 + 2\arctan(\psi/q).$$

The passage to variables x and y is provided by the transformation [4]

$$x + iy = i\int \tilde{E}^{-1}\exp(i\tilde{\theta})d\psi.$$

Upon calculating the integral in the right-hand part of this relationship, separating real and imaginary parts, and excluding the parameter ψ, we arrive at

$$\tilde{x}^2 = \tilde{y}^2 - \tilde{y}^3,$$

(where $\tilde{y} = 2y/(3q^2)$ and $\tilde{x} = 2x/(\sqrt{3}\,q^2)$), which corresponds to the so-called parabolic folium (see figure). This surface is self-intersecting at $\tilde{x} = \tilde{y} = 0$, which implies that the solution is physically unrealizable.

From this we infer that the initial assumption concerning the possibility for the electric field strength at an equilibrium surface to be considerably greater than the applied value E_0 is incorrect, and, hence, no singu-

lar (cusp) stationary configurations of the charged surface of a conducting liquid ensuring unlimited local amplification of the electric field at the cusps (breaks) can exist in two-dimensional geometry.

Consequently, a certain ultimately permissible value of the field perturbation on the equilibrium surface of such a liquid exists that depends on the applied field strength and the parameters of medium. For example, in the class of solutions to the problem concerning the stationary configuration of a conducting liquid for $g = 0$ (gravity forces ignored) found in [4, 5], the maximum possible field strength at the surface is $7.1E_0$.

It must be also pointed out that an analogous situation takes place for a dielectric liquid bearing the free surface charge providing for the equipotentiality condition. In this case, an additional term appears in the equation of force balance (1) to account for the electrostatic pressure at the surface on the side of liquid. Evidently, this term is negligibly small at the cusps (the field at the singular points is screened by the surface) and the surface shape can be described to a high precision by Eq. (2). From this we infer that dielectric liquids, as well as the conducting ones, cannot exhibit equilibrium cusp formation on the charged surface in the planar geometry.

Acknowledgments. This study was supported by the Russian Foundation for Basic Research (project nos. 00-02-17428) and by the INTAS Foundation (project no. 99-1068).

REFERENCES

1. G. I. Taylor, Proc. R. Soc. London, Ser. A **280**, 383 (1964).
2. A. L. Pregenzer and B. M. Marder, J. Appl. Phys. **60** (11), 3821 (1986).
3. V. G. Suvorov and E. A. Litvinov, J. Phys. D **33**, 1245 (2000).
4. N. M. Zubarev, Zh. Éksp. Teor. Fiz. **116** (6), 1990 (1999) [JETP **89**, 1078 (1999)].
5. N. M. Zubarev, Pis'ma Zh. Tekh. Fiz. **25** (22), 79 (1999) [Tech. Phys. Lett. **25**, 920 (1999)].

Translated by P. Pozdeev

Technical Physics Letters, Vol. 27, No. 3, 2001, pp. 220–222. Translated from Pis'ma v Zhurnal Tekhnicheskoĭ Fiziki, Vol. 27, No. 6, 2001, pp. 7–12.

A Mechanism of Electron Emission in an Open Discharge

A. P. Bokhan and P. A. Bokhan

Institute of Semiconductor Physics, Siberian Division, Russian Academy of Sciences, 630090 Novosibirsk, Russia

Received October 16, 2000

Abstract—The effect of an artificial UV emission from the drift space on the open discharge current, caused by an additional discharge operating between the anode and the electron collector, was studied. The experiments were performed in the continuous, quasicontinuous, and pulsed regimes of the electron beam generation in a range of currents from 1 mA/cm^2 to 10 A/cm^2. It was established that the energy efficiency of the additional discharge acting upon the beam current is greater than that of the beam proper. It is concluded that UV emission is the main factor providing for the supply of electrons to the open discharge. © *2001 MAIK "Nauka/Interperiodica".*

Open discharge as the source of an electron beam is an object of extensive investigation. An important question of this research is related to the nature of electron emission from the cathode to the discharge region. Previously, it was believed that the main mechanism responsible for the beam current in the open discharge is an UV emission from the drift space [1–5]. However, this model was later criticized, for the most part in [6–8] where the role of UV emission was reduced to providing a uniform discharge initiation in the early stage at a current density of $j < 10^{-4}$ A/cm^2. Subsequently, up to a current density on the order of $j \le 10^{-1}$ A/cm^2, the discharge is maintained by ionization in the field protruding beyond the anode grid into the drift space. Then the process develops into an anomalous glowing discharge, during which the main fraction of the beam electrons is generated [9, 10].

The limited space in this publication does not allow us to analyze the results of [6–10] in much detail. A full analysis is planned for publication in the *Zhurnal Tekhnicheskoĭ Fiziki* (Journal of Technical Physics). Here we will only note that the evidence presented in [6–10] is entirely indirect and cannot serve a basis for unambiguously judging the nature of electron emission in an open discharge. The main effort in this study was devoted to direct experiments aimed at determining the influence of the UV emission from the drift space on the current–voltage characteristics of the open discharge.

For this purpose, the usual cell configuration conventionally employed for the open discharge realization (cathode–anode grid–drift space–electron collector) was modified by adding a second grid mounted in the drift space at a distance of 2 mm from the anode grid. The length of the drift space was 20 mm. The cathode–anode distance was 1 mm, and the anode grid cell size was 0.2 mm. The experiments devoted to elucidating the effect of the UV emission from the drift space on the discharge characteristics were performed with both grids at the same potential. This minimized the field sagging both from the cathode–anode region into the drift space (beyond the second grid) and from the drift space to the accelerating gap. As a result, it was possible to study the direct effect of the UV emission from the drift space by increasing its intensity with the aid of an additional gas discharge operating in this space.

The experimental discharge cell employed a polished stainless steel cathode with a diameter of 13.5 mm and a perforated anode with a diameter of 12.5 mm. The working gas (commercial high-purity grade helium) was additionally purified with the aid of an activated charcoal trap. The open discharge operation was studied in three regimes: (1) continuous (current density up to 5 mA/cm^2); (2) quasicontinuous (current density, up to 1 A/cm^2) involving rectangular pulses with a typical duration of 10 μs; and (3) pulsed (current density, up to 10 A/cm^2) employing the discharge of a 600 pF capacitor through the accelerating gap. In order to minimize the role of transient processes related to the discharge initiation in regimes 2 and 3, a continuous initiating discharge with a current density of 1–2 mA/cm^2 was maintained in the gap. Under these conditions, according to the conclusions of [8, 9], no effect of UV emission from the drift space should be manifested at all.

Figure 1 shows the plots of the discharge current I_2 (measured in the second grid–collector circuit) and I_g (cathode–anode, or accelerating gap circuit) versus the voltage U_2 applied to the second grid–collector gap (curves *1* and *2*, respectively). The accelerating voltage was U_g = 1040 V and the helium pressure was p_{He} = 11 Torr. Curves *1*' and *2*' show the analogous curves measured in the quasicontinuous regime for U_g = 2400 V and p_{He} = 16 Torr. In all cases, the collector potential was positive relative to the second grid potential.

Figure 2 shows the plots of the relative current increment versus the P_p/P_d ratio, where P_p is the dis-

charge power calculated using from data of Fig. 1 and P_d is the power dissipated by fast electrons on crossing the drift space (calculated as described in [5, 11, 12]). The energy losses of electrons with energies in the keV range are calculated to within a 50% accuracy. Nevertheless, the data of Fig. 2 indicate that an additional discharge with a power typically smaller than that dissipated by the beam results in doubling of the current in the anode–cathode circuit. It should be emphasized that this doubling takes place at an additional discharge voltage sufficiently small to exclude the possibility of electron multiplication in the second grid–collector circuit (i.e, under the conditions of a strictly non-selfsustained discharge, maintained by the high-energy electron beam). A discharge of this type affects only the secondary electron energy distribution in the beam. Since the major contribution to the gas excitation by the beam is related to the secondary electrons [5, 11], we may speak of the identical nature of the UV quanta production and their action upon the electron emission from the cathode. Therefore, the close energy efficiencies of the electron beam action and the additional discharge effect upon the current in the accelerating gap is evidence for the photoelectron nature of the electron generation in the open discharge, at least for current densities below 1 A/cm^2.

The results of experiments with additional UV emission performed in the pulsed regimes are difficult to interpret because a short electron pulse propagating in a weakly ionized gas generates large induction currents. As a result, the beam penetration becomes significantly lower, and the UV emission power becomes significantly greater than the values provided by the energy loss calculations. In these regimes, the effect of UV emission was studied in a two-stage experiment. First, we measured the *I–V* curves for the open discharge at a floating potential of both grids [13] and determined the floating potential value of these grids relative to the collector. Then the *I–V* curve was measured for the discharge in the cell with grounded grids. The difference between the two cases consists in that an additional current passes between collector and grids in the former (floating grid potential) regime due to a charge leak from the grids.

It was found that the floating potential on the grids in the continuous and quasicontinuous regimes was U = 15–20 V. The effect of this potential and the related current on the *I–V* curves was precisely the same as the effect of potential U_2 observed (see above) in the case of independent additional discharge operating in the second grid–collector gap. In the pulsed regime, the U value was essentially nonstationary and varied in a complicated manner. During the current development, U = 200–400 V and the open discharge current measured in the floating grid potential mode was 30–50% greater than that in the grounded grid mode.

Taking into account the results described above, the effect of the additional UV emission was checked upon applying an additional potential U_c to the collector relative to the grounded grids. The U_c value was selected such that an independent discharge could not be induced even in the presence of the electron beam. The *I–V* curves of the open discharge were measured with and without applying this additional potential to the collector. Figure 2 shows a plot (curve *3*) of the current gain I_g/I_{g0} determined with an additional potential of

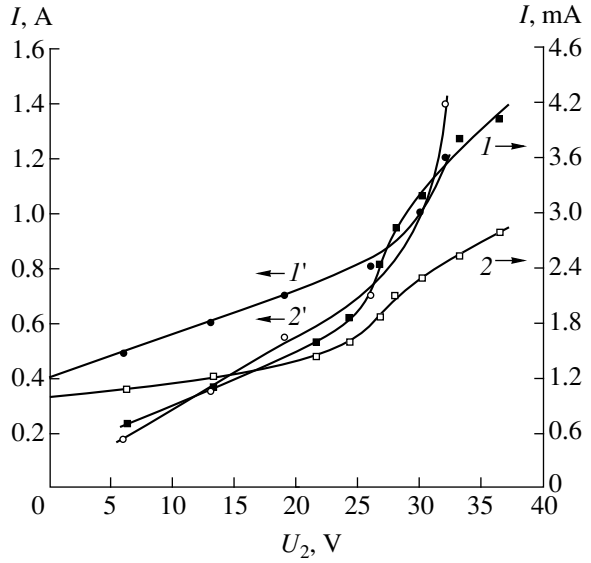

Fig. 1. The plots of discharge currents (*1*, *1*') I_2 measured in the second grid–collector circuit and (*2*, *2*') I_g measured in the cathode–anode gap (accelerating gap) circuit versus the voltage U_2 applied to the second grid–collector gap in the (*1*, *2*) continuous and (*1*', *2*') quasicontinuous regimes.

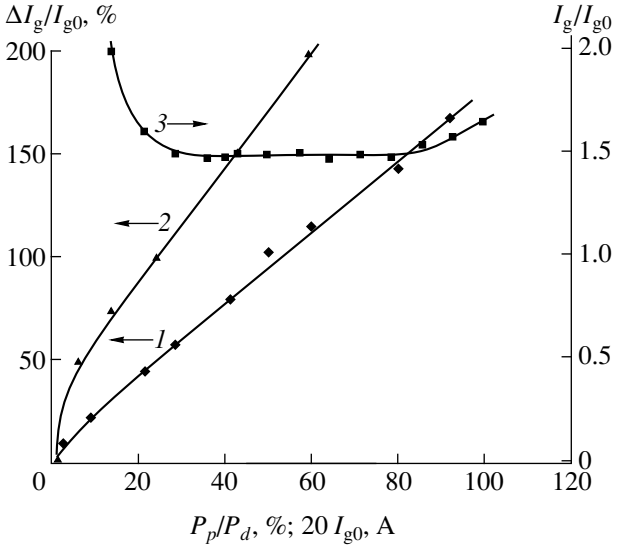

Fig. 2. Plots of (*1*, 2) the current increment $\Delta I_g/I_{g0}$ in the cathode–anode gap versus relative power P_p/P_d supplied to the drift space and (*3*) current gain I_g/I_{g0} versus I_{30} measured in the (*1*) continuous, (*2*) quasicontinuous, and (*3*) pulsed open discharge regimes.

U_c = –300 V relative to the I_{g0} value observed for U_c = 0. The curve is nonmonotonic, but the current gain in all cases is not smaller than that due to the additional UV emission during the open discharge in the floating potential mode. This is evidence that the open discharge current in the pulsed regime is also due to the photoelectrons generated under the action of UV emission from the drift space.

Thus, the results of our direct experiments for determining the role of UV emission from the drift space showed that, in a broad range of conditions including the pulsed, quasicontinuous, and continuous discharge regimes with the discharge current ranging from 1 mA/cm^2 to 10 A/cm^2, the open discharge current is determined by the photoelectron emission from the cathode surface. Therefore, the open discharge is not an anomalous discharge as was stated in [9, 10]. This is manifested, in particular, in that the current density in the open discharge is smaller by more than one order of magnitude as compared to the value in the anomalous discharge. A more detailed comparison between open and anomalous discharges, including analysis of the *I*–*V* characteristics, will be given in the following publication.

REFERENCES

1. P. A. Bokhan and G. V. Kolbychev, Zh. Tekh. Fiz. **51** (9), 1823 (1981) [Sov. Phys. Tech. Phys. **26**, 1057 (1981)].
2. G. V. Kolbychev and B. A. Samyshkin, Zh. Tekh. Fiz. **51** (10), 2031 (1981) [Sov. Phys. Tech. Phys. **26**, 1185 (1981)].
3. G. V. Kolbychev and N. V. Ptashnik, Zh. Tekh. Fiz. **59** (9), 104 (1989) [Sov. Phys. Tech. Phys. **34**, 1018 (1989)].
4. P. A. Bokhan, Zh. Tekh. Fiz. **61** (6), 61 (1991) [Sov. Phys. Tech. Phys. **36**, 620 (1991)].
5. S. V. Arlantsev, B. L. Borovich, V. V. Buchanov, *et al.*, J. Russ. Laser Res. **16** (2), 99 (1995).
6. A. R. Sorokin, Pis'ma Zh. Tekh. Fiz. **21** (17), 33 (1995) [Tech. Phys. Lett. **21**, 692 (1995)].
7. A. R. Sorokin, Pis'ma Zh. Tekh. Fiz. **21** (20), 37 (1995) [Tech. Phys. Lett. **21**, 832 (1995)].
8. A. R. Sorokin, Pis'ma Zh. Tekh. Fiz. **22** (13), 17 (1996) [Tech. Phys. Lett. **22**, 526 (1996)].
9. A. R. Sorokin, Zh. Tekh. Fiz. **68** (3), 33 (1998) [Tech. Phys. **43**, 296 (1998)].
10. K. A. Klimenko and Yu. D. Korolev, Zh. Tekh. Fiz. **60** (9), 138 (1990) [Sov. Phys. Tech. Phys. **35**, 1084 (1990)].
11. Yu. N. Sytsko and S. I. Yakovlenko, Fiz. Plazmy **2** (1), 63 (1976) [Sov. J. Plasma Phys. **2**, 34 (1976)].
12. L. A. La Verne and A. J. Mozumder, J. Phys. Chem. **89** (20), 4219 (1985).
13. A. R. Sorokin, Pis'ma Zh. Tekh. Fiz. **17** (23), 92 (1991) [Sov. Tech. Phys. Lett. **17**, 858 (1991)].

Translated by P. Pozdeev

Technical Physics Letters, Vol. 27, No. 3, 2001, pp. 223–225. Translated from Pis'ma v Zhurnal Tekhnicheskoĭ Fiziki, Vol. 27, No. 6, 2001, pp. 13–18.

The Effect of a Space Charge of Electrons Multiply Backscattered from the Anode on the Current in a Planar Diode

A. V. Kirikov*, V. V. Ryzhov, I. Yu. Turchanovskiĭ**, and V. I. Bespalov***

** Institute of High-Current Electronics, Siberian Division, Russian Academy of Sciences, Tomsk, Russia*

*** Tomsk Polytechnical University, Tomsk, Russia*

e-mail: kir@to.hcei.tsc.ru

Received October 2, 2000

Abstract—The effect of a space charge of electrons multiply backscattered from the anode on the current in a planar diode was theoretically studied. Spectral distributions of the energy of electrons moving along the electric field were calculated by the Monte Carlo code. It was found that the maximum decrease in the current of diodes with high-Z anodes does not exceed 20%. © *2001 MAIK "Nauka/Interperiodica".*

In a planar nonrelativistic diode, the density of the electric current passing through the device is related to the applied voltage by the well known "3/2" law,

$$j_0 = \frac{2}{9\pi}\left(\frac{e}{2m}\right)^{1/2}\frac{U^{3/2}}{d^2}, \qquad (1)$$

where e and m are the electron charge and mass, respectively; d is the interelectrode gap width; and U is the anode potential [1]. This relationship is derived for the case when the anode fully absorbs all the electrons of the incident beam.

In real diodes, a certain fraction of the electrons in the beam accelerated to an energy of $\varepsilon_0 = eU$ exhibit reflection from the anode and, losing some of their initial energy, return to the diode gap. Then, these electrons are stopped and reaccelerated by the field to strike the anode surface again. A fraction of the electrons returned to the anode upon a single reflection may be reflected once more, leading to a "cloud" of n-fold reflected electrons forming in the diode space. This space charge leads to a decrease in the diode current as compared to the diode current value j_0 predicted by the Child–Langmuir formula (1). This effect was repeatedly studied both experimentally and theoretically, but the results of various investigations still exhibit certain discrepancies. For example, Zaĭtsev *et al.* [2] experimentally established that a decrease in the diode current amounts to 10%, while the theoretical calculation of Pereira [3] predicted that the effect may reach 25–40%.

In order to describe the characteristics of a nonrelativistic diode with an allowance for the space charge formed by multiply backscattered electrons, it is necessary to solve the Poisson equation for the potential $\phi(x) = \varphi(x)/U$ [1]:

$$\frac{d^2\phi}{dx^2} = -4\pi j_d^{sc}\left(\frac{d^2}{U^{3/2}}\right)\left(\frac{m}{2e}\right)^{1/2}[\phi^{-1/2} + F(\phi, x)]. \qquad (2)$$

In the stationary case, the forward and reverse currents of scattered electrons are equal in absolute value. Under this assumption, the function $F(\phi, x)$ describing a distribution of the charge of reflected electrons in the interelectrode gap has the following form:

$$F(\phi, x) = 2\int_{1-\phi(x)}^{1}\frac{f_x(t')}{[t' - (1-\phi(x))]^{1/2}}dt'. \qquad (3a)$$

Here, $f_x(t = \varepsilon_x/eU)$ is the distribution of reflected electrons with respect to the kinetic energy of motion along the x-axis coinciding with the electric field vector orientation. This function can be expanded into a series with respect to the order of the electron reflection from anode [3]:

$$f_x(t) = \sum_{i=1}^{n} R_i f_i(t) = \sum_{i=1}^{n}\bar{\eta}^i\tilde{f}(t) \approx \tilde{f}(t)\sum_{i=1}^{n}\bar{\eta}^i = \frac{\bar{\eta}}{1-\bar{\eta}}\tilde{f}(t) = R\tilde{f}(t), \qquad (4)$$

where $R_i = (\bar{\eta})^i$ is the fraction of primary electrons reflected from the anode in the ith reflection; $R = \sum_{i=1}^{\infty} R_i = \frac{\bar{\eta}}{(1-\bar{\eta})}$ is the fraction of electrons reflected in all orders; $\bar{\eta}$ is the reflection coefficient averaged over

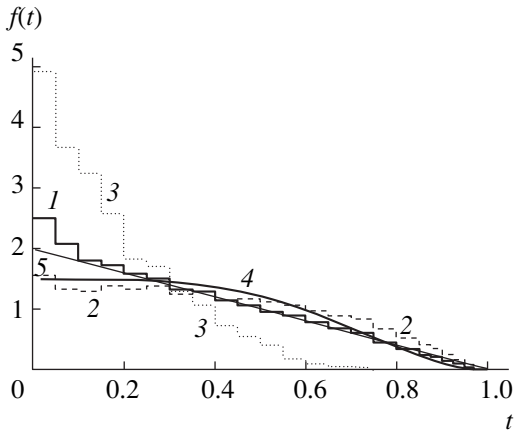

Fig. 1. The distribution functions (normalized to unity) of electrons multiply backscattered from a Pt anode (U = 100 kV) with respect to the kinetic energy of motion along the x-axis (histograms were calculated by the TRACS program): (*1*) total spectrum; (*2*) spectrum upon the first reflection; (*3*) spectrum upon the fourth reflection; (*4*) spectrum calculated by formula (5); (*5*) $f_\Delta = 2(1 - t)$.

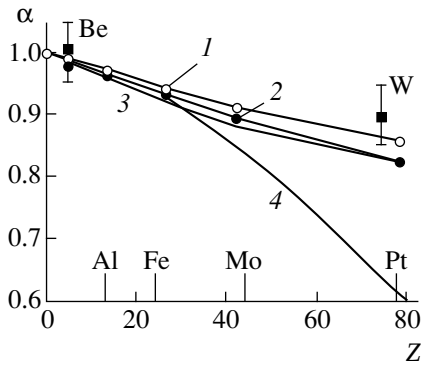

Fig. 2. Plots of the current attenuation in a planar diode versus atomic number Z: (*1*) calculation with allowance for electrons upon single reflection; (*2*) calculation taking into account multiply backscattered electrons; (*3*) calculation for $f_\Delta = 2(1 - t)$; (*4*) data from [3]. Points present the experimental data for beryllium and tungsten taken from [2].

the particle angles and energies; and $f_i(t)$ is the distribution function (normalized to unity) of i-fold reflected electrons with respect to the kinetic energy of motion along the x-axis. Assuming that the shape of the spectrum is independent of the order of reflection, $f_i(t) \approx \tilde{f}(t)$, the above series (4) is readily integrated to yield

$$F(\phi, x) = 2\frac{\bar{\eta}}{1-\bar{\eta}} \int_{1-\phi(x)}^{1} \frac{\tilde{f}(t')}{[t' - (1-\phi(x))]^{1/2}} dt'. \quad (3b)$$

This formula indicates that, in the linear approximation, a contribution to the diode current decrease due to electrons multiply reflected from heavy (high-Z) elements is comparable to the contribution of electrons upon the first reflection. Therefore, a correct evaluation of the space charge effect requires taking into account the contribution of electrons reflected in all orders, which implies that the electron angle and energy distribution functions must be determined.

At present, data on the $f_x(t)$ and $f_i(t)$ functions are not available because the calculation of these distributions with allowance for multiple backscattering encounters certain difficulties. For example, Pereira [3] described the $f_x(\varepsilon_x)$ function using analytical expressions derived under the assumption that the differential angular and energy distributions of n-fold reflected electrons $f(\varepsilon, \theta)$ are independent of the corresponding distributions of incident particles and can be presented in the form $f(\varepsilon, \theta) = g(\varepsilon)\cos\theta$, where $g(\varepsilon)$ is the universal energy spectrum of reflected electrons. Under these assumptions, the distribution function for n = 4–6 is

$$f_x(\varepsilon_x) = (n+2)/n\pi\{1 - \varepsilon_x^n[1 + n(1-\varepsilon_x)]\}. \quad (5)$$

In order to calculate the distribution functions of multiply backscattered electrons with respect to the kinetic energy of motion along the x-axis, we developed a special TRACS program capable of modeling (using the Monte Carlo code [4]) the electron trajectories in a diode with preset electric and magnetic fields (equations of motions) with allowance for the electron scattering in the anode material. Figure 1 (histograms) shows the results of calculation of the $f_i(t)$ and $f_x(t)$ functions for a diode with a platinum anode operated at U = 100 kV; line *5* represents a model distribution in which the fraction of low-energy electrons gradually increases by the law $f_\Delta = 2(1 - t)$. For comparison, the areas of all distributions are normalized to unity.

As seen from Fig. 1 (curve *4*), the distribution given by Eq. (5) [3] is applicable only to the distribution of electrons upon the first reflection (resulting from the initial electron beam normally incident to the anode). The results of our calculations showed that an increase in the multiplicity of reflection increases the proportion of low-energy electrons in the $f_i(t)$ distributions, so that the latter functions depend on the reflection order. Therefore, approximation (3b) may appear as rather rough, for example, in diodes with high-Z anode materials.

To the first approximation, the $f_x(t)$ distributions for large-Z anodes depend on the energy according to a linear law: $f_\Delta = 2(1 - t)$. We obtained a solution to the Poisson equation for this model distribution by using expansion into a hypergeometric series. According to this solution, the ratio of the diode current j_d^{sc} calculated with allowance for the space charge effect on the Langmuir current j_0 determined by formula (1) is given by the expression (Fig. 2, curve *1*)

$$\alpha = j_d^{sc}/j_0 = \left[{}_2F_1\left(a; b; c; -d\frac{\bar{\eta}}{1-\bar{\eta}}\right)\right]^2, \quad (6)$$

where ${}_2F_1$ is the hypergeometric function of the second kind, a = 3/8, b = 1/2, c = 11/8, and d = 16/15.

For the distribution functions $f_x(t)$ obtained by the Monte Carlo method, the values of α were determined by numerically solving the Poisson equation (2) in approximation (3a). The results of these numerical calculations for the diodes with aluminum, iron, molybdenum, and platinum anodes are presented in Fig. 2 by points on curve *2*. For comparison, curve *1* shows the results of calculations taking into account only the contribution of electrons upon the first reflection. A difference between curves *1* (single reflection) and *2* (total reflection spectrum) is determined by a decrease in the diode current caused by the multiple backscattering; for high-*Z* metals, this difference may reach up to 25%.

A decrease in the diode current determined from the results of our calculations is only about one third of the value predicted by Pereira [3]. This difference is explained by the fact that the spectra of multiply reflected electrons calculated by the Monte Carlo code contain a markedly greater proportion of low-energy electrons as compared to the spectrum (5) used in [3] (see Fig. 1). The effect of low-energy electrons on the diode current is not as pronounced as that of the high-energy particles. However, our calculated data are closer to the experimental results reported in [2]. Any discrepancy still observed can be explained by the effect of a magnetic mirror existing near the collector of the experimental setup, which results in not all the electrons scattered from anode returning to the diode region.

Acknowledgments. The authors are grateful to S.D. Korovin and S.Ya. Belomyttsev for valuable advice and fruitful discussions.

This study was supported by the Russian Foundation for Basic Research.

REFERENCES

1. R. B. Miller, *Introduction to the Physics of Intense Charged Particle Beams* (Plenum, New York, 1982; Mir, Moscow, 1984).
2. N. I. Zaĭtsev, G. S. Korablev, I. S. Kulagin, and V. E. Nechaev, Fiz. Plazmy **8** (5), 918 (1982) [Sov. J. Plasma Phys. **8**, 515 (1982)].
3. N. R. Pereira, J. Appl. Phys. **54** (11), 6307 (1983).
4. V. I. Bespalov, V. V. Ryzhov, and I. Yu. Turchanovskiĭ, Pis'ma Zh. Tekh. Fiz. **24** (4), 77 (1998) [Tech. Phys. Lett. **24**, 157 (1998)].

Translated by P. Pozdeev

Technical Physics Letters, Vol. 27, No. 3, 2001, pp. 226–228. Translated from Pis'ma v Zhurnal Tekhnicheskoĭ Fiziki, Vol. 27, No. 6, 2001, pp. 19–25.

Nonequilibrium Phase Transitions and *S*-Shaped Current–Voltage Characteristics in a Model Semiconductor–Metal System

A. V. Melkikh, A. A. Povzner, A. G. Andreeva, and I. N. Sachkov

Ural State Technical University, Yekaterinburg, Russia

Received May 31, 2000; in final form, November 3, 2000

Abstract—A model of nonequilibrium phase transition in a semiconductor–metal system was considered using a finite-element method. It is shown that, beginning with a certain fraction of the metal component in the heterophase system, the *S*-shaped current–voltage characteristics exhibit a change: the system features a hysteresis but possesses no singular points. *© 2001 MAIK "Nauka/Interperiodica".*

1. As is known, the current–voltage (*I–V*) characteristics of semiconductors and related film resistors exhibit *S*- and *N*-shaped nonlinearities in strong electric fields [1–3]. At present, it is reliably established that the appearance of these nonlinearities is accompanied by nonlocal features in the electric current distribution. However, the factors responsible for these features are not yet completely clear. In particular, nonlocal features in the electric current distributions were not studied in heterophase systems comprising a semiconductor matrix with metal inclusions.

In addition, a system with the *S*-shaped *I–V* characteristic should exhibit an instability of the nonequilibrium phase transition type. This instability may be related to positive feedback between the temperature of a sample and the current density in this sample. Indeed, an increase in the current enhances heating of the material, which leads to a further growth in the current density (since the current significantly increases with the temperature).

2. First, let us consider the behavior of a single-phase semiconductor film. The conductivity of the semiconductor is assumed to be temperature dependent, with the *I–V* curve determined by the following relationship:

$$j = \sigma_0 \frac{1}{L} \exp\left(-\frac{E_g}{kT}\right)\Delta\varphi, \tag{1}$$

where j is the current density, σ_0 is a constant (independent of the temperature to the first approximation), L is the sample length, and E_g is the semiconductor bandgap width.

It must be taken into account that the heat dissipated in the semiconductor may lead to an increase in the sample temperature. An increase in the sample temperature will lead to a growth in the conductivity, since the concentration of free electrons in semiconductors exponentially increases with the temperature. This accounts for the positive feedback that enables hysteresis manifestations to occur in the system.

The power density liberated in the system can be expressed as the product

$$j\Delta\varphi. \tag{2}$$

The thermal flux density from sample to substrate can be approximately expressed as

$$-2\lambda\frac{T_0 - T}{h}, \tag{3}$$

where λ is the thermal conductivity of the sample material, T is the temperature established as a result of the heat evolution, T_0 is the substrate temperature, and h is the sample thickness.

In the stationary state, the quantities (2) and (3) must be equal. Using this condition, we can obtain a formula for the sample temperature:

$$T = T_0 + j\Delta\varphi\frac{h}{2\lambda}. \tag{4}$$

Substituting this formula into Eq. (1), we obtain an expression showing that the current density is a nonlinear function of $\Delta\varphi$:

$$j = \sigma_0 \frac{1}{L} \exp\left(-\frac{E_g}{k(T_0 + j\Delta\varphi h/2\lambda)}\right)\Delta\varphi. \tag{5}$$

Let us analyze this relationship for the presence of extrema. Taking a derivative and equating it to zero,

$$\frac{\partial\Delta\varphi}{\partial j} = \frac{L}{\sigma_0}\exp\left(\frac{E_g}{kT}\right)\left[1 - \frac{E_g\left(j\Delta\varphi + j^2\frac{\partial\Delta\varphi}{\partial j}\right)\frac{kh}{2\lambda}}{\left(kT_0 + \frac{kh}{2\lambda}j\Delta\varphi\right)^2}\right] = 0, \tag{6}$$

1063-7850/01/2703-0226$21.00 © 2001 MAIK "Nauka/Interperiodica"

we obtain an equation for the singular points,

$$\left(kT_0 + \frac{kh}{2\lambda}X\right)^2 = \frac{E_g kh}{2\lambda}X, \quad (7)$$

where $X = (j\Delta\varphi)_s$ (the subscript s implies singularity). Solving this equation with respect to X, we obtain

$$X_{1,2} = \frac{2\lambda}{kh}\frac{E_g - 2kT_0 \pm \sqrt{E_g(E_g - 4kT_0)}}{2}. \quad (8)$$

The critical points of the system are determined by zeros of the expression under the square root or the second derivative:

$$\frac{\partial^2 \Delta\varphi}{\partial j^2} = 0. \quad (9)$$

This condition yields the values of parameters that are critical from the standpoint of the metastable state formation:

$$(E_g)_c = 4kT_0, \quad X_c = \frac{2\lambda T_0}{h}. \quad (10)$$

For $E_g > (E_g)_c$, the system has an *S*-shaped *I–V* curve. In this region, each value of the potential difference corresponds to three values of the current density.

Let us consider the behavior of the system for $E_g > (E_g)_c$ in the interval of potential differences $\Delta\varphi_{S1} < \Delta\varphi < \Delta\varphi_{S2}$. In this interval, one branch of the *S*-shaped *I–V* characteristic is metastable. The average value of j apparently corresponds to the absolutely unstable state and is not realized in practice. Near the $\Delta\varphi_{S2}$ value, the "cold" current becomes unstable and the system passes in a jumplike manner to the upper branch ("thermal breakdown"). Near $\Delta\varphi_{S1}$, the "hot" current is unstable and the system passes to the lower branch.

3. Let us analyze the *I–V* characteristic for a two-dimensional semiconductor matrix with square metal inclusions (Fig. 1). The content of the metal component may vary.

In calculating the *I–V* curve for this semiconductor–metal system, we have used an approach based on the variational form of the transfer equations and the method of finite elements. According to this approach, a square elementary cell is separated in the heterogeneous system under consideration, the boundaries of which coincide with the lines of mirror symmetry of the regular structure (dashed line in Fig. 1). We use the cells of minimum size containing one quarter of the metal inclusion. The origin of the Cartesian coordinate system (X, Y) is placed into a cell vertex and the coordinate axes are directed along the cell sides. The electric field is oriented in the Y axis. The lines $Y = Y_0$ and $Y = 0$ are equipotential, while the lines $X = 0$ and $X = X_0$ are not penetrated by the flow.

The electric potential distribution $\varphi(X, Y)$ is established using a variational approach, according to which

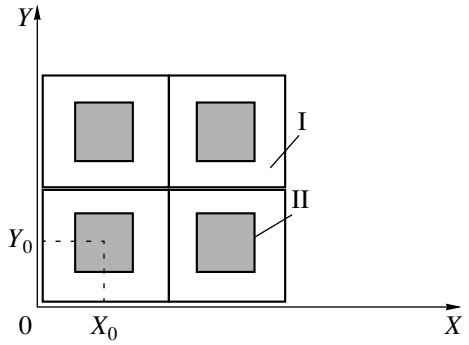

Fig. 1. A scheme of the model heterophase system comprising a semiconductor matrix I with metal inclusions II and the coordinate system used in the analysis.

the transfer processes correspond to extrema of the functional

$$\chi = \int_{S_c} \sigma(\text{grad}\varphi)^2 dS, \quad (11)$$

where σ is the local conductivity and S_c is the elementary cell area. The function φ corresponding to a minimum of χ is determined by the finite-element method [4] involving discretization of the two-dimensional space S_c with the aid of triangular simplex elements. The function $\varphi(X, Y)$ is approximated in the S_c region by a continuous piecewise linear function with the parameters uniquely determined by a set of nodal values $\{\varphi_j\}$. The algorithm of finding $\varphi(X, Y)$ is described in detail elsewhere [5]. Using the approximate values of the potential, one may readily calculate the fields of potential gradient, current density, and heat deposition density.

A numerical experiment for determining the effect of the concentration of inclusions in the *I–V* characteristics was performed on a personal computer of the IBM PC type using lattices with a cell density of 50×100, adapted to the shape of inclusions. Figure 2 shows typical *I–V* curves obtained by the method of finite elements, where $j^* = \langle j\rangle/\langle j\rangle_0$ and $E^* = \langle E\rangle/\langle E\rangle_0$ are the relative current density j and the field strength $E = \text{grad}\varphi$ averaged over the elementary cell area S_c, respectively ($\langle j\rangle_0$ and $\langle E\rangle_0$ are the average of values j and E for a homogeneous metal conductor at a temperature equal to the substrate temperature T_0). In Fig. 2, the solid curve refers to a single- phase semiconductor film and dashed curves correspond to heterophase systems with various concentrations C of the metal component. The calculations were performed assuming $E_g = 10kT_0$. The conductivity of the metal phase was assumed to be independent of the temperature and taken to be equal to the semiconductor conductivity at $T = T_0$.

An analysis of the results of our numerical experiment led to the following conclusions. The single-phase system (e.g., $C = 0$) exhibits hysteresis phenom-

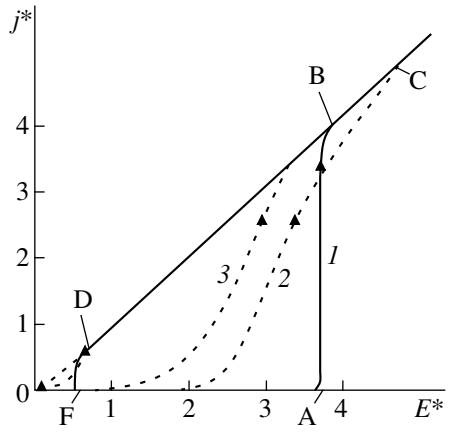

Fig. 2. Current–voltage characteristics of a semiconductor-metal system with various concentrations of the metal component $C = 0$ (*1*); 0.8 (*2*); 0.6 (*3*).

ena analogous to those discussed above. The cold branch of the *I–V* curve corresponds to a very small conductivity. For this reason, the region of this branch between points 0 and A (Fig. 2) virtually coincides with the abscissa axis. Then the system very sharply passes from a cold to a hot branch (A–B transition). As the field strength increases further, the system follows a linear relationship $j^*(E^*)$ (along the BC line) typical of a metal. As the applied voltage is decreased, the *I–V* characteristic exhibits a considerable hysteresis followed by a jumplike passage to the cold branch (D–F transition).

Introducing the metal inclusions smears the transitions between cold and hot branches of the *I–V* characteristic. The higher the metal content in the system, the smaller the difference of currents corresponding to the two branches and the narrower the hysteresis loop. An analysis of the topograms of the spatial distribution of temperature within an elementary cell in the heterogeneous system studied showed that the single-phase and heterophase systems differ in the character of the nonequilibrium transition from the cold to the hot branch. In a pure semiconductor film, the transition proceeds virtually simultaneously over the entire space. In a semiconductor matrix–metal inclusion system, heated regions first appear in the semiconductor in the regions with the maximum concentration of current lines and then expand with increasing applied voltage. Analogous behavior is observed for the reverse transition. This spatial inhomogeneity leads to the disappearance of the points corresponding to the loss of stability determined by Eq. (6).

Thus, we have established that, at certain values of the applied potential difference, a metal–semiconductor matrix system must exhibit a sharp change in the current that can be considered as a nonequilibrium phase transition. In the heterogeneous system, the transition from the cold to the hot state takes place at much lower voltages than the analogous transition in the single-phase system. This decrease in the transition threshold is explained by a nonuniform current distribution in the heterogeneous system. This behavior has much in common with some other phenomena such as, for example, ignition and quenching [6].

Finally, it should be noted that we have considered a simplified but still rather typical situation. Subsequently we will consider transformations of the *I–V* characteristics of heterophase systems depending on the shape of inclusions, on the relative values of E_g, λ, and L, and on the parameters characterizing heat exchange in the system studied. We may expect systems to exist in which the current density distribution is characterized by a still greater nonuniformity. Therefore, it would also be of interest to study the transition features related to the geometry of the heterophase system and the laws of processes leading to the decay of the metastable conducting sates. This circumstance seems to be very important from the standpoint of searching for the new ways to increase the operational stability of resistors based on composite heterophase systems comprising a mixture of semiconductor and metal components.

REFERENCES

1. A. Krotkus and Z. Dobrovol'skis, *Electric Conductivity of Narrow-Bandgap Semiconductors* (Mokslas, Vilnius, 1988).
2. V. L. Bonch-Bruevich, I. P. Zvyagin, and A. G. Mironov, *Domain Electrical Instabilities in Semiconductors* (Nauka, Moscow, 1972; Consultants Bureau, New York, 1975).
3. M. E. Levinshteĭn, K. Yu. Pozhela, and M. S. Shur, *Gunn Effect* (Sov. Radio, Moscow, 1975).
4. L. Segerlind, *Applied Finite Element Analysis* (Wiley, New York, 1976; Mir, Moscow, 1979).
5. I. N. Sachkov, Zh. Tekh. Fiz. **66** (12), 48 (1996) [Tech. Phys. **41**, 1225 (1996)].
6. A. G. Merzhanov and A. M. Stolin, Prikl. Mekh. Tekh. Fiz., No. 1, 65 (1974).

Translated by P. Pozdeev

Technical Physics Letters, Vol. 27, No. 3, 2001, pp. 229–232. Translated from Pis'ma v Zhurnal Tekhnicheskoĭ Fiziki, Vol. 27, No. 6, 2001, pp. 26–33.

The Dissolution of Intermetallic Inclusions in Atomic Displacement Cascades during Neutron Irradiation of Dispersion-Hardening Alloys

V. V. Sagaradze, V. M. Koloskov, V. A. Shabashov, T. M. Lapina, V. L. Arbuzov, B. N. Goshchitskiĭ, and V. D. Pakhomenko

Institute of Metal Physics, Ural Division, Russian Academy of Sciences, Yekaterinburg, Russia

Received in final form October 24, 2000

Abstract—The data of Mössbauer spectroscopy show evidence of a low-temperature (340 K) dissolution of dispersed intermetallic Ni_3Ti particles in the fcc lattice of a Fe–Ni–Ti Invar-type alloy under the conditions of cascade-inducing neutron irradiation. The dissolution rate markedly increases with a decrease in the initial size of the intermetallic particles. © *2001 MAIK "Nauka/Interperiodica".*

The process of secondary phase dissolution in atomic collision cascades was theoretically analyzed in [1]. Unfortunately, experimental data concerning the dissolution of intermetallic particles under the conditions of ion irradiation are rather few; this is still more valid for the neutron irradiation. The most informative report of Nelson *et al.* [2] presented the electron-microscopic data indicative of the dissolution of rather large particles of the γ'-Ni_3Al phase and the formation of smaller γ' phase particles in nickel-based alloys subjected to cascade-inducing ion irradiation under the conditions of elevated temperatures (923 K). However, under these conditions, it is difficult to separate the effects related to thermal, radiation-enhanced, and non-equilibrium radiation-initiated processes.

Discussing the results reported in [2], Gelles [3] came to the conclusion that the concept of γ' phase dissolution in the atomic displacement cascades is inapplicable to the analysis of radiation-induced structural changes in the aged PE-16 alloy. Estimates of the low-temperature (298 K) dissolution of the ordered Ni_3Al intermetallic phase [2], based on the vanishing of superstructural reflections, is also rather ambiguous and can be assigned entirely to disordering of the γ' phase inclusions. The purpose of this work was to study the neutron-initiated process of Ni_3Ti particle dissolution by the method of Mössbauer spectroscopy. Ni_3Ti intermetallic phase inclusions represent a rather widely occurring phase in fcc reactor alloys.

The experiments were performed on a model aging fcc alloy N35T3 of the Invar type with the composition (at. %): Ni, 34.2; Ti, 3; C, 0.1; Fe, balance. From the standpoint of determining the content of a coherent ordered γ'-Ni_3Ti phase in the irradiated samples of this alloy, insufficient information is provided both by electron microscopy (due to the poor resolution of the disperse particles) and by neutron diffractometry (since neutron irradiation may produce disordering of the Ni_3Ti phase without dissolving it), which complicates the quantitative phase analysis based on the measurement of superstructural reflections. For this reason, the process of the radiation-induced dissolution or separation of the high-nickel Ni_3Ti phase, leading to the austenite matrix enrichment with or depletion of nickel, respectively, and strongly changing magnetic properties of the model alloy, was studied by Mössbauer spectroscopy which is most informative in this respect.

The Mössbauer spectra were measured at 298 K on a nuclear γ-resonance spectrometer with a $^{57}Co(Cr)$ source. Dissolution of the dispersed γ'-Ni_3Ti phase in the atomic displacement cascades was studied in the course of irradiation of the alloy samples with fast neutrons (fluence, 5×10^{19} cm^{-2} and structure-damaging dose, ~0.05 displacements per atom). The exposures were carried out in an IVV-2M reactor; the samples were maintained at a temperature of 340 K in order to avoid the development of competitive aging processes activated at elevated temperatures. As is known [4] the presence of titanium atoms in the lattice sites (substitution solution) at an amount of 2–3 wt % virtually does not affect the Mössbauer spectra of the alloy studied. However, the dissolution or separation of the high-nickel Ni_3Ti phase leads to a strong change in the magnetic characteristics, in particular, in the Zeeman splitting of the Mössbauer signal [4]. Thus, the redistribution of Ni in the N35T3 alloy can be studied within the framework of the quasibinary approximation.

However, solving the direct spectral problem of separating individual components (subspectra) corresponding to certain atomic positions in the matrix of a Fe–Ni Invar-type alloy from the total experimental Mössbauer spectrum is hindered by poor resolution and by the distributed character of the Mössbauer parameters. Development of the molecular models of mixed

1063-7850/01/2703-0229$21.00

exchange interaction [6, 7] and "smeared" magnetic transition [8–10] in fcc Fe–Ni alloys made it possible to establish relationships between the inhomogeneous magnetic structure and the composition fluctuations in these alloys [9–13]. It was concluded that the distribution of atoms in the alloy matrix can be analyzed using the functions of distribution of the effective internal field strength $P(H)$ on ^{57}Fe nuclei.

The distribution density functions $P(H)$ were restored using the Window [14] and Hesse–Rubartsch [15] algorithms with regularization [16]. The initial information was represented by data on the asymmetry of the Mössbauer spectra of Fe–Ni alloys, related to a difference between the isomer shift (*IS*) values of the paramagnetic and ferromagnetic austenite, and by notions of the "smeared" magnetic transition admitting coexistence of the paramagnetic and ferromagnetic regions at temperatures below T_C. In the ferromagnetic region, a variable linear relationship was established between H and *IS* (in accordance with the model describing dependence of the magnetic moment of iron on the nearest atomic environment), while the anisotropic magnetic and quadrupole contributions were neglected because of the small magnetic moments of Fe and Ni atoms and the cubic symmetry of the crystal lattice. Reliability of the restored $P(H)$ function was judged by the regularization process and by stability of the solution $P(H)$ with respect to various restoration algorithms [14, 15]. It is commonly accepted [9, 11, 12] that peaks in the density function $P(H)$ at higher field strengths correspond to increased Ni concentrations within the first coordination sphere of Fe.

The quantitative interpretation of $P(H)$ is ambiguous (exhibiting a rather qualitative character) because of the superposition of dynamic processes in the system of magnetic moments [17], which is especially pronounced in the vicinity of T_C. For this reason, the quantitative analysis based on the $P(H)$ calculations was supplemented by algorithms of the Mössbauer "phase" analysis, according to which the "phases" (regions of the structure exhibiting local inhomogeneity) can be characterized by stable average values of the distributed Mössbauer parameters, for example, the $\hat{H}$ value calculated as the weighted-average $\hat{H} = \Sigma HP(H)$. The possibility of quantitative analysis based on the average Mössbauer parameters is explained by the strong dependence of both local and average Mössbauer parameters on the local and average alloy composition. The calculated average $\hat{H}$ values were used for determining the matrix composition of the N35T3 alloy using the calibration curves $\hat{H} = f(C_{\mathrm{Ni}})$ obtained in [5]. The upper limiting error in determining $\hat{H}$, related to the maximum uncertainty of the aprioric Mössbauer parameters, is lower by at least one order of magnitude than the magnitude of variations in the $\hat{H}$ value to be analyzed.

In fcc Fe–Ni alloys of the N36 type irradiated with fast neutrons at an energy of $E > 0.1$ MeV in an IVV-2M reactor, the average size of the atomic displacement cascade region is 4–6 nm [18]. Therefore, it was of interest to estimate the rate of the radiation-induced dissolution of intermetallic inclusions with dimensions both smaller and greater than the displacement cascade region. The coherent γ'-Ni_3Ti phase particles with the smallest size of 2–3 nm [19–20] and an fcc lattice close to that of the austenite matrix were obtained by incomplete quenching of the N35T3 alloy samples in water from 1323 K. These particles are poorly resolved in the electron microscope, showing a diffraction contrast of the ripple type. The γ'-Ni_3Ti phase inclusions of greater size (with a diameter of up to ~8 nm) were obtained by aging the quenched N35T3 alloy for 30 min at 923 K.

Figure 1 (curves *a*, *a*', *c*, *c*') shows the Mössbauer spectra and the corresponding magnetic field strength distributions $P(H)$ in the N35T3 alloy containing γ'-Ni_3Ti particles of various dimensions. After the neutron irradiation at 340 K, both the Mössbauer spectra and the $P(H)$ distributions significantly change (cf. curves *b*, *b*', *d*, *d*'). The $P(H)$ functions corresponding to the spectra of initial and irradiated samples exhibit a number of density peaks, where the growth in H reflects an increase in the number of Ni atoms in the first coordination sphere of Fe [9]. The irradiation leads to an increase in the integral intensity (area) of peaks with higher H values, which corresponds to the increase in the nickel content in the alloy matrix. Judging by the average magnetic field strength on the ^{57}Fe nucleus ($\hat{H}$ = 137 kOe), we may conclude (see [5]) that the Fe–Ni–Ti austenite matrix of the N35T3 alloy contains ~31.2 at. % Ni (for an overall nickel concentration of 34.2 at. %). Therefore, 3 at. % of nickel belong to the γ'-Ni_3Ti phase formed in the course of quenching. Thus, the total proportion of atoms constituting the γ' phase in the quenched N35T3 alloy is 4 at. % (according to the Ni_3Ti stoichiometry).

The Mössbauer spectrum of the neutron-irradiated alloy (fluence, 5×10^{19} cm^{-2}, 340 K) displays a magnetic sextet with a significantly greater average field ($\hat{H}$ = 171 kOe) on the ^{57}Fe nucleus, which corresponds to a reduction in the average nickel content in austenite of 32.4 at. % (Fig. 1, curves *b* and *b*'). This change can be explained only by the radiation-induced dissolution of the high-nickel γ'-Ni_3Ti phase. The neutron irradiation of a nonaging alloy Fe + 35 at. % Ni under the same conditions produced no noticeable changes in the Mössbauer spectra. It should be noted that a change in the H value for the fcc Fe–Ni alloy can be also related to the process of phase separation and/or short-range ordering. However, in this case the appearance of partial components corresponding to increased fields in $P(H)$ is accompanied by the formation of components corresponding to small fields [21, 22]. As a result, the

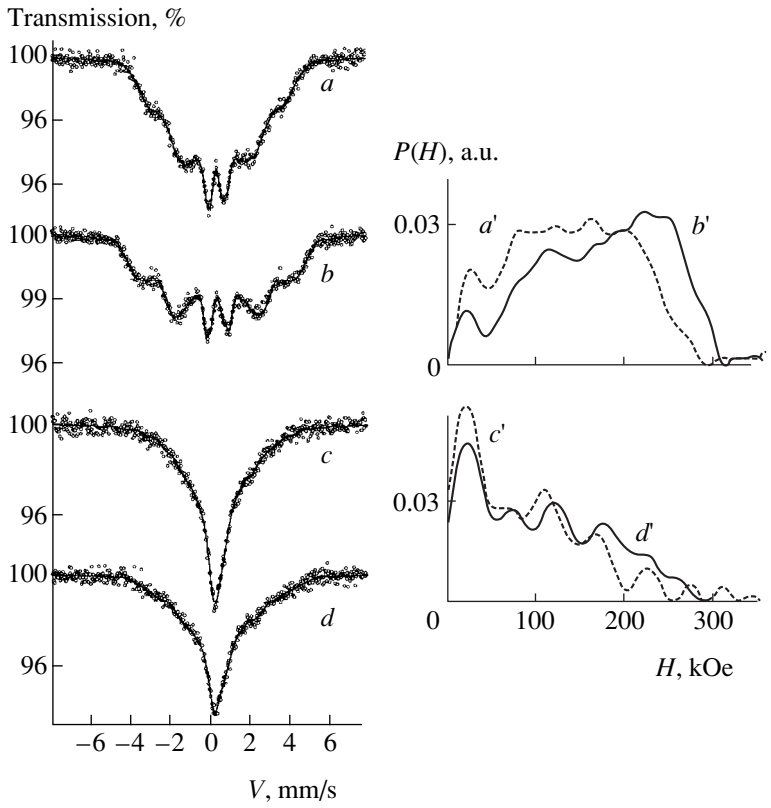

Fig. 1. (*a*–*d*) The Mössbauer spectra and (*a*'–*d*') the corresponding probability density functions of the magnetic field strength distribution $P(H)$ for the N35T3 alloy after various treatments: (*a*, *a*') quenching from 1373 K; (*b*, *b*') quenching followed by fast neutron irradiation at 340 K to a fluence of 5×10^{19} cm^2; (*c*, *c*') aging for 0.5 h at 923 K; (*d*, *d*') aging followed by fast neutron irradiation.

$\hat{H}$ value varies rather insignificantly. The Mössbauer spectra and the corresponding $P(H)$ distributions for the aging N35T3 alloy with large (8 nm) particles of the γ' phase measured before and after irradiation are presented by curves *c* and *d* in Fig. 1. The neutron irradiation increases the average field strength on the $\hat{H}$ nucleus from 90 to 104 kOe, which corresponds to the average nickel concentration increasing by only 0.2 at. % (from 30.5 to 30.7 at. %) [5].

Thus, an increase in the nickel concentration in the austenite matrix upon irradiation of the N35T3 alloy with small (2–3 nm) and large (8 nm) particles of the γ' phase by 1.2 and 0.2 at. %, respectively, is indicative of a radiation-induced dissolution of 1.6 at. % Ni and Ti constituting the disperse γ'-Ni_3Ti phase particles in the quenched alloy and of 0.27 at. % Ni and Ti from larger γ' phase inclusions in the aged alloy. The atomic mixing and dissolution of γ' phase particles may take place when an atomic displacement cascade involves either the edges of the particle and the matrix or the whole particle (if the particle dimensions are smaller than the size of the displacement cascade region). An atomic displacement cascade formed inside a large Ni_3Ti inclusion produces only disordering of this intermetallic particle, rather than dissolution of the γ' phase in the matrix.

Let us compare the character of the γ' phase distribution in the quenched and aged Fe–Ni alloy to the distribution of cascade regions caused by the neutron irradiation. According to the Mössbauer data, the austenite matrix in the quenched N35T3 alloy (with a total of 34.2 at. % Ni) contains only 31.2 at. % Ni. The remainder (3 at. % Ni) enters into the disperse γ'-Ni_3Ti phase particles, which corresponds to a total of 4 at. % Ni and Ti. For an average γ' particle size of 2 nm, the density of these inclusions is approximately 4.5×10^{18} cm^{-3} (see table in [23]) and the average distance between their centers is 5 nm (or 3 nm between the particle surfaces). This pattern of the intermetallic phase distribution is illustrated in Fig. 2a. After aging of the of the N35T3 alloy at 923 K, the difference between initial and residual nickel in the austenite amounts to 3.7 at. %, which corresponds to 4.9 at. % Ni and Ti entering into the Ni_3Ti phase. For an average γ' particle size of 8 nm, the density of these inclusions is ~10^{17} cm^{-3}, the average distance between the particle centers is ~17 nm, and the average distance between their surfaces is ~9 nm [23] (Fig. 2b). Assuming the initial size of the displacement cascade region to be 6 nm [18], any random distribution of cascades in the quenched N35T3 alloy would enable each cascade involve one or more disperse particles and would induce their dissolution (Fig. 2a). In the aged

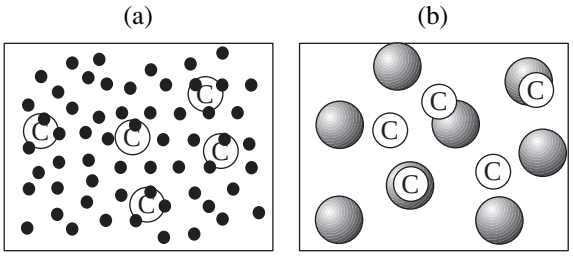

Fig. 2. Schematic diagrams illustrating the distribution of atomic displacement cascades (indicated by open circles) in samples of the N35T3 alloy with (a) small and (b) large particles of the γ' phase (represented by black circles).

alloy with an average distance between the particle surfaces of ~9 nm, the atomic displacement cascade may form either at the edge of a particle, between particles, or inside a particle (Fig. 2b). In the latter two cases, the cascade will not induce dissolution of the intermetallic particle. For a neutron fluence of 5×10^{19} cm^{-2}, the concentration of the atomic displacement cascades with an average size of 6 nm may amount to ~10^{18} cm^{-3} [18], which accounts for ~1/3 of the total sample volume [23]. Not taking into account the probability that a collision cascade would strike the same site, the fraction of disperse γ' phase particles dissolved in the quenched N35T3 alloy matrix reaches ~33%. Apparently, the proportion of coarse inclusions dissolved during the irradiation of an aged alloy will be markedly smaller.

It must be noted that one equilibrium phase transformation in Fe–Ni alloys of the N35T3 type at such a low temperature is aging with a γ' phase separation. This is confirmed by data on the radiation-accelerated aging of these alloys at 433–473 K in the course of a cascade-free sample irradiation by an electron beam with an energy of 5.5 MeV [5]. This electron bombardment resulted primarily in the formation of single vacancies and interstitial atoms. From this we may conclude that the radiation-induced dissolution of intermetallic particles observed in the N35T3 alloy at 340 K is related predominantly to processes occurring in the atomic displacement cascade regions rather than to a "postdynamic" effect enhanced by the point radiation defects.

Acknowledgments. This study was supported by the International Scientific-Technological Center (project no. 467) and by the Russian Foundation for Basic Research (project no. 00-15-96581).

REFERENCES

1. A. S. Bakaĭ and N. M. Kiryukhin, Vopr. At. Nauki Tekh. **5** (28), 33 (1983).
2. R. S. Nelson, J. A. Hudson, and D. J. Mazey, J. Nucl. Mater. **44**, 318 (1972).
3. D. S. Gelles, J. Nucl. Mater. **83**, 200 (1979).
4. V. A. Shabashov, V. V. Sagaradze, S. V. Morozov, and G. A. Volkov, Metallofizika **12** (4), 107 (1990).
5. V. V. Sagaradze, V. A. Shabashov, T. M. Lapina, and V. L. Arbuzov, Fiz. Met. Metalloved. **78** (4), 88 (1994).
6. S. K. Sidorov and A. V. Doroshenko, Fiz. Met. Metalloved. **19** (5), 786 (1965).
7. A. Z. Men'shikov and E. E. Yurchikov, Zh. Éksp. Teor. Fiz. **63** (1), 190 (1972) [Sov. Phys. JETP **36**, 100 (1972)].
8. B. N. Rolov, *Smeared Phase Transitions* (Zinatne, Riga, 1972).
9. V. V. Bukhalenkov, in *Proceedings of the International Conference on the Applications of the Mössbauer Effect, ICAME-83, 1983*, H5, p. 273.
10. J. Crangle and G. C. Hallam, Proc. R. Soc. London, Ser. A **272** (1348), 119 (1963).
11. A. Z. Men'shikov and E. E. Yurchikov, Izv. Akad. Nauk SSSR, Ser. Fiz. **36** (7), 1463 (1972).
12. V. A. Makarov, I. M. Puzeĭ, T. V. Sakharova, and I. G. Gutovskiĭ, Zh. Éksp. Teor. Fiz. **67** (2), 771 (1974) [Sov. Phys. JETP **40**, 382 (1975)].
13. S. Komura, G. Lippman, and W. Shmatz, J. Magn. Magn. Mater. **5** (2), 123 (1977).
14. B. Window, J. Phys. E **4** (5), 401 (1971).
15. J. Hesse and A. Rubartsch, J. Phys. E **7** (7), 526 (1974).
16. V. S. Litvinov, S. D. Karakishev, and V. V. Ovchinnikov, *Nuclear Gamma-Resonance Spectroscopy of Alloys* (Metallurgiya, Moscow, 1982).
17. F. van der Woud and A. J. Bekker, Phys. Status Solidi **9** (3), 775 (1965).
18. B. N. Goshchitskii, V. V. Sagaradze, V. L. Arbuzov, *et al.*, J. Nucl. Mater. **258**–**263**, 1681 (1998).
19. J. K. Abraham, J. K. Jackson, and K. Leonard, ASM Trans. Q. **61**, 223 (1968).
20. V. M. Alyab'ev, V. G. Vologin, S. F. Dubinin, *et al.*, Fiz. Met. Metalloved., No. 8, 142 (1990).
21. A. Chamberod, J. Laugier, and J. M. Penisson, J. Magn. Magn. Mater. **10** (2–3), 139 (1979).
22. S. S. Aliev, P. L. Gruzin, A. Z. Men'shikov, *et al.*, Metallofizika **7** (5), 80 (1985).
23. V. V. Sagaradze, V. M. Nalesnik, S. S. Lapin, and V. M. Alyabiev, J. Nucl. Mater. **202**, 137 (1993).

Translated by P. Pozdeev

Technical Physics Letters, Vol. 27, No. 3, 2001, pp. 233–235. Translated from Pis'ma v Zhurnal Tekhnicheskoĭ Fiziki, Vol. 27, No. 6, 2001, pp. 34–39.

InGaAs Nanodomains Formed *in situ* on the Surface of (Al,Ga)As

I. L. Krestnikov, N. A. Cherkashin, D. S. Sizov, D. A. Bedarev, I. V. Kochnev†, V. M. Lantratov, and N. N. Ledentsov

Ioffe Physicotechnical Institute, Russian Academy of Sciences, St. Petersburg, Russia;
e-mail: igov@beam.ioffe.vssi.ru

Received October 30, 2000

Abstract—A new method for obtaining InGaAs nanodomains on the surface of GaAs or (Al,Ga)As is suggested. At the first stage, an InGaAs layer with a thickness above the critical value for dislocation formation is deposited onto the substrate surface by metalorganic CVD. Then the InGaAs film is coated with a thin AlAs layer and annealed at an elevated temperature. The "repulsion" of AlAs from plastically relaxed regions near dislocations and the high temperature stability of AlAs result in that evaporation is restricted to the regions containing defects. The self-organization effects favor the formation of an ordered array of coherent nanodomains that can be used for obtaining buried low-dimensional nanostructures and/or nanoheteroepitaxial inclusions. © *2001 MAIK "Nauka/Interperiodica".*

In recent years, considerable progress has been achieved in obtaining semiconductor micro- and optoelectronic devices by methods involving self-organization processes [1]. These achievements are especially pronounced in the fabrication of longwave (1.3 μm) lasers based on structures with quantum dots (QDs) on GaAs substrates [2–4]. The progress is based on the development of technologies for obtaining three-dimensional QDs using molecular beam epitaxy (MBE) [5] or metalorganic chemical vapor deposition (MOCVD) [6] processes employing growth by the Stranski–Krastanow mechanism. MOCVD laser heterostructures with QDs showed a high temperature stability of the threshold current at room temperature [7]. In addition to producing the effects related to modification of the density of states, QDs are capable of considerably suppressing the surface transport of nonequilibrium charge carriers thus decreasing their nonradiative recombination on crystal faces. This prevents the working faces from overheating and inhibits the growth of dislocations stimulated by nonradiative recombination.

Below we describe a new method for obtaining InGaAs nanodomains, which is principally different from the methods based on the Stranski–Krastanow or Volmer–Weber growth mechanisms. In the proposed method, an InGaAs (quantum dot) layer with a thickness above the critical value for dislocation formation is deposited by MOCVD onto an AlGaAs underlayer (buffer). A lattice mismatch between deposit and substrate results in the formation of a dislocation network in InGaAs. The InGaAs QD with the dislocation network is coated with a thin AlAs layer, which forms a continuous film only on the dislocation-free areas retaining the lattice parameter of the AlGaAs buffer (equal to the lattice parameter of GaAs). The dislocation pileups serve as the sites of stress release for the biaxially compressed InGaAs layer. As a result, the lattice parameter at these sites becomes greater than that of GaAs (AlAs). Thus, a structure is formed in which the defect-free areas are coated with a thin continuous

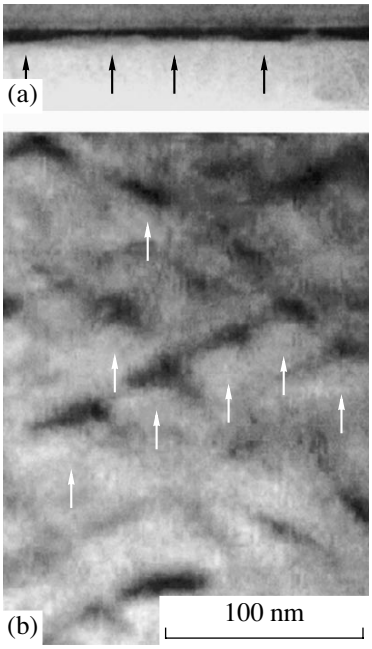

Fig. 1. A TEM micrograph of InGaAs nanodomains (indicated by arrows) in a sample prepared with an AlAs overlayer: (a) transverse cross section; (b) plane view.

† Deceased.

1063-7850/01/2703-0233$21.00 © 2001 MAIK "Nauka/Interperiodica"

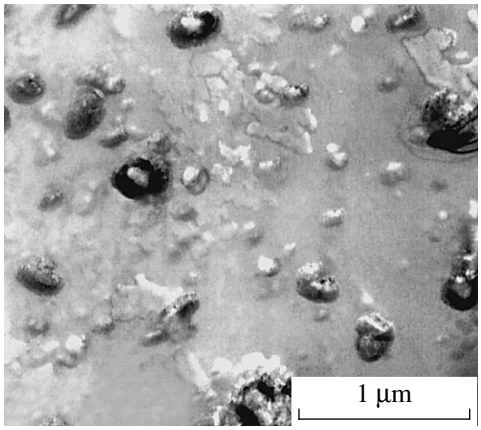

Fig. 2. A TEM micrograph (plane view) of a sample prepared without a protective AlAs overlayer, showing the formation of defect clusters and indium droplets.

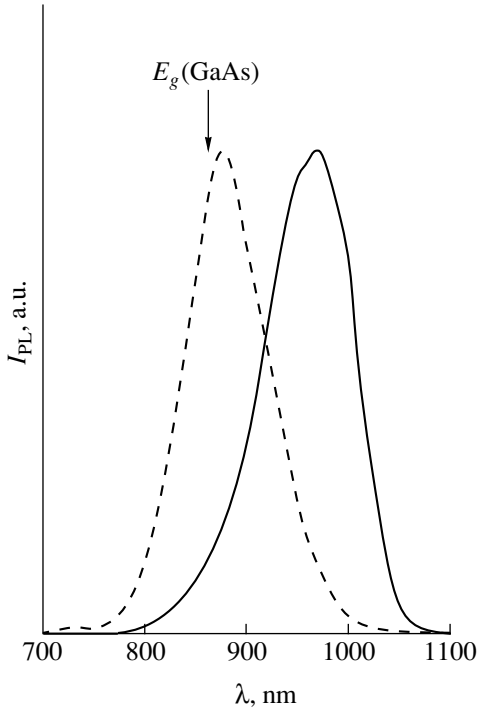

Fig. 3. Normalized room-temperature PL spectra of InGaAs nanodomain structures prepared with (solid curve) and without (dashed curve) AlAs overlayers.

AlAs film, whereas the dislocated regions remain exposed. The subsequent high-temperature annealing leads to evaporation of the exposed (dislocated) InGaAs regions, while the AlAs-coated areas of InGaAs form defect-free nanodomains. These nanodomains can be subsequently overgrown with (Al,Ga)As or used for nanoheteroepitaxy.

The sample structures studied were prepared by MOCVD on (001)-oriented GaAs substrates. The component sources were trimethylgallium, trimethylaluminum, trimethylindium, and arsine. A buffer layer of $Al_{0.2}Ga_{0.8}As$ was grown on the substrate heated to a temperature of 750°C, while the $In_{0.3}Ga_{0.7}As$ QD with a thickness of 20 nm was deposited at 600°C. The temperature was decreased immediately in the course of the AlGaAs buffer layer growth, without suspending the process. A ~2-nm-thick AlAs layer was also deposited at 600°C. The subsequent high-temperature annealing was effected at 750°C for 2 min in a hydrogen atmosphere, while the third group elements and arsine were not supplied to the reactor. Upon annealing, the structure was overgrown with $Al_{0.2}Ga_{0.8}As$ at 750°C. In order to eliminate the nonradiative recombination of charge carriers on the outer surface and at the substrate, the active region was insulated from these interfaces by $Al_{0.3}Ga_{0.7}As$ barriers. For comparison, we studied the sample structures with and without thin AlAs overlayers.

The samples were studied by transmission electron microscopy (TEM) on a Philips EM-420 microscope operated at an accelerating voltage of 100 kV. The room-temperature photoluminescence (PL) spectra were excited by radiation of a Ar^+ laser focused on a sample. The emission was analyzed by an MDR-23 monochromator and detected by cooled photomultiplier tubes (FEU-83) operated in the photon count mode.

Figure 1 shows a typical TEM micrograph of a sample structure with an AlAs overlayer. As seen, the domain formation is clearly manifested both in the plane and in the transverse cross section. The domain size varies from 20–30 to 50–60 nm. As seen in the cross section image, the nanodomains are shaped like mushrooms. This is probably explained by an elastic stress relaxation in the upper part of the InGaAs nanodomains, whereby the nanodomain top expands into the empty space formed as a result of annealing and slows down the evaporation of InGaAs [8]. Thus, we may suggest that the lattice parameter in the upper part of the nanodomain is close to that of InGaAs. This circumstance can be employed for subsequently growing inclusions with a high indium content and/or large thickness on the top of InGaAs nanodomains, which would provide laser structures emitting in the region of 1.3 or 1.55 μm. The shape of the nanodomains does not correspond to the pattern of dislocations characteristic of plastically relaxed InGaAs regions on GaAs substrates, but is rather close to that observed in such layers upon a high-temperature annealing *ex situ* [9].

A critical factor from the standpoint of obtaining an ordered array of nanodomains is the presence of the AlAs overlayer protecting the InGaAs QDs in the course of annealing. In the absence of this overlayer, the surface features the evaporation of InAs accompanied by the formation of indium droplets (see Fig. 2 presenting the TEM of a sample prepared without AlAs overlayer). In this case, the quantum energy corresponding to the PL intensity maximum (Fig. 3, dashed

curve) is close to the GaAs bandgap width, while the PL peak for the structure with AlAs overlayer (Fig. 3, solid curve) exhibits a longwave shift and broadening related to the distribution of nanodomains with respect to lateral dimensions.

Thus, the results of our investigation showed that high-temperature annealing of dislocated InGaAs quantum dots coated with a thin AlAs film leads to the formation of an ordered array of defect-free nanodomains. This structure can be used as an active region of optoelectronic devices and/or a base structure for nanoheteroepitaxy.

Acknowledgments. This work was supported in part by the Russian Foundation for Basic Research and by the Volkswagen Foundation.

REFERENCES

1. D. Bimberg, M. Grundmann, and N. N. Ledentsov, *Quantum Dot Heterostructures* (Wiley, Chichester, 1999).
2. D. L. Huffaker, G. Park, Z. Zou, *et al.*, Appl. Phys. Lett. **73**, 2564 (1998).
3. Yu. M. Shernyakov, D. A. Bedarev, E. Yu. Kondrat'eva, *et al.*, Electron. Lett. **35**, 898 (1999).
4. G. T. Liu, A. Stintz, H. Li, *et al.*, Electron. Lett. **35**, 1163 (1999).
5. V. M. Ustinov, N. A. Maleev, A. E. Zhukov, *et al.*, Appl. Phys. Lett. **74**, 2815 (1999).
6. N. N. Ledentsov, M. V. Maximov, D. Bimberg, *et al.*, Semicond. Sci. Technol. **15**, 604 (2000).
7. M. V. Maximov, I. V. Kochnev, Yu. M. Shernyakov, *et al.*, Jpn. J. Appl. Phys. **36**, 4221 (1997).
8. F. Turco, J. C. Guillaume, and J. Massies, J. Cryst. Growth **88**, 282 (1988).
9. R. Beanland, M. A. Lourenco, and K. P. Homewood, in *Microscopy of Semiconductor Materials*, Ed. by A. G. Gullis and J. L. Hutchinson; Inst. Phys. Conf. Ser. **157**, 145 (1997).

Translated by P. Pozdeev

Technical Physics Letters, Vol. 27, No. 3, 2001, pp. 236–239. Translated from Pis'ma v Zhurnal Tekhnicheskoĭ Fiziki, Vol. 27, No. 6, 2001, pp. 40–49.

Skin Effect, Ion-Acoustic Turbulence, and Anomalous Transport in a Nonisothermal Solid-State Plasma Generated by a High-Power Femtosecond Laser

N. B. Volkov

Institute of Electrophysics, Ural Division, Russian Academy of Sciences, Yekaterinburg, Russia
e-mail: nbv@ami.uran.ru
Received October 19, 2000

Abstract—We propose an interpretation of the experimental data reported by Milchberg, Freeman *et al.* [1] on the absorption of intense 400-fs laser radiation pulses in an aluminum target. It is shown that the electric conductivity of a nonisothermal aluminum plasma possessing a solid-state density in these experiments was determined by the ion-acoustic oscillations (ion-acoustic turbulence). It is therefore necessary to study theoretically the ion-acoustic turbulence effect in a nonisothermal plasma possessing solid-state density. Possible approaches to a theoretical description of this effect and the interactions of a such a plasma with high-power ultrashort laser pulses are discussed. © *2001 MAIK "Nauka/Interperiodica".*

The progress achieved in obtaining ultrashort pulses of high-power laser radiation is primarily related to solving the tasks of fundamental and applied physics, in particular, to the need in energy sources for pumping X-ray and gamma lasers and the inertial thermonuclear synthesis process [2]. The interaction of ultrashort high-power laser radiation pulses with various substances, in particular, with metals, gives rise to new physical phenomena. For example, semiconductor targets exhibit superfast vibronic phase transitions [3], while metal targets show the formation of periodic spatial surface structures [4] and generate protons with energies up to 18 MeV [5] and soft X-ray radiation [6] (see also [7]).

Milchberg, Freeman *et al.* [1] measured the intensity of high-power laser radiation with a fixed pulse duration (t_p = 400 fs) reflected from an aluminum target and established that the reflection coefficient decreased with increasing intensity of the incident laser radiation. According to experimental estimates (based on the results of spectral measurements) of the electron temperature T_e of the laser-generated plasma, this value varied from room temperature up to 100 eV. Figure 1 shows the relationship between the resistivity of the aluminum plasma and the laser intensity determined [1] by mathematically solving the inverse problem (each point in this figure corresponds to an independent experiment). Attempts at explaining the results reported in [1], were based on various hypotheses, including the possibility of superfast energy exchange between electrons and ions [8]. However, simple estimates presented below show that the target lattice cannot be heated during the laser pulse action. The main purpose of this short communication is to discuss the possible physical mechanisms responsible for absorption of the energy of ultrashort laser pulses without recourse to any *ad hoc* hypotheses about ultrafast energy exchange between electrons and ions.

Before considering the experimental results obtained by Milchberg, Freeman *et al.* [1], let us present several estimates of the parameters of an aluminum plasma possessing a solid-state density at $T = T_0$ = 300 K with a particle concentration of $n = n_0 = 6.02 \times 10^{22}$ cm^{-3}. We obtain $r_s = (3m_i(4\pi\rho_0)^{-1})^{1/3} = 1.583 \times 10^{-8}$ cm for the average interatomic distance (m_i and ρ_0 are the ion mass and the unperturbed metal density, respectively); Z = 13 and z_0 = 3 are the nuclear charge and the number of free electrons per unit atomic cell; Θ = 428 K is the Debye temperature; and ε_F = 11.63 eV is the Fermi energy. The Debye frequency ω_m and the average sound velocity C_{s0} determined using the Θ value are $\omega_m = 6.502 \times 10^{13}$ s^{-1} and $C_{s0} = 4.885 \times 10^5$ cm/s. The isothermal ion sound velocity C_{si} corresponding to the electron temperature at the Fermi energy $T_F = 2\varepsilon_F/(3k_B)$ is $C_{si} = (k_B T_F/m_i)^{-1/2} = 5.265 \times 10^5$ cm/s. The close values C_{s0} and C_{si}, as well as the proximity of the isotropic Debye phonon spectrum and the spectrum of ion-acoustic oscillations in the nonisothermal plasma, allowed some researchers to identify lattice oscillations in nontransition metals (plasmalike media) with ion-acoustic oscillations [9]. The ion and electron plasma frequencies are $\omega_{pi} = 1.873 \times 10^{14}$ s^{-1} and $\omega_{pe} = 1.384 \times 10^{16}$ s^{-1}, respectively, so that $\omega_{pe} \gg \omega_{pi} > \omega_m$. The time of establishing an equilibrium distribution in the electron and phonon gas is $\tau_r \sim 1.5 \times 10^{-14}$ s. The time of establishing a thermodynamic equilibrium between electrons and phonons (lattice) τ_ϵ

1063-7850/01/2703-0236$21.00 © 2001 MAIK "Nauka/Interperiodica"

obeys the inequality $1.465 \times 10^{-12} < \tau_\epsilon < 3.781 \times 10^{-10}$ s, where the lower limit is obtained using the formula $\tau_\epsilon = k_B T_i \tau_r (2 m_e C_{s0}^2)^{-1}$ valid for $T_i \gg \Theta$ [10] (in aluminum at $T_0 = 300$ K and $\Theta \sim T_0$ this formula gives a correct lower estimate for τ_ϵ). The upper limit for τ_ϵ is based on the relationship $\tau_\epsilon = m_i \tau_r (2 m_e)^{-1}$ obtained for $T \longrightarrow \infty$ from the expression used in obtaining the lower estimate. A lower estimate of the skin layer thickness is $\delta_s = 9.339 \times 10^{-6}$ cm $\gg r_s$. Assuming that plasma in the skin layer expands at a velocity equal to C_{s0} (ideal skin layer explosion), the wave of rarefaction propagating at the velocity of sound would travel over the distance δ_s during $t_s = 1.912 \times 10^{-11}$ s $> \tau_\epsilon \gg \tau_r$ (note that $t_s \gg t_p$).

The above estimates show, with a high accuracy, that the aluminum plasma obtained in [1] was essentially nonisothermal and possessed a density equal to that of the initial metal. The phonon gas in this medium can be considered as "cold", possessing a temperature of $T_i = T_0 = 300$ K. In connection with this, we must note that an interpretation of the experimental results obtained in [1] (in particular, those presented in Fig. 1) proposed by Yakubov [8] employed various model relationships obtained in the physics of low-temperature nonideal plasma. In particular, the ascending branch of the resistivity curve in the vicinity of the maximum was descried in [8] by a "universal" expression for the electric conductivity of a nonideal plasma (obtained in experiments on the impact compression of inert gases) assuming the ion temperature to be $T_i = 0.8$ eV $= 9.28 \times 10^3$ K. Therefore, a question arises as to what can be the physical mechanism capable of heating aluminum ions up to 9280 K during the laser pulse as short as $t_p = 4 \times 10^{-13}$ s (see the above estimates). We believe that it would be more correct to assume that, under the conditions studied in [1], ions were cold (having a temperature of 300 K). In this case, a factor responsible for the observed increase in resistivity of the aluminum target heated by a femtosecond laser pulse must be related to certain small-scale kinetic instabilities [11].

The lowest excitation threshold in a nonisothermal plasma at $T_e \gg T_i$ belongs to the ion-acoustic instability, whereby low-frequency acoustic oscillations are excited in the plasma at an ion sound velocity $C_{si} = (k_B T_e m_i^{-1})^{1/2}$ and exhibit a resonance collisionless decay (Landau damping) [9]. Upon reaching a certain threshold level (in a current-carrying plasma, the drift velocity exceeds the ion sound velocity [11, 12]), the plasma features excitation caused by ion-acoustic turbulence leading to the appearance of an anomalous resistivity. The effective collisional frequency ν_{eff} in this case is proportional to the ratio $T_e T_i^{-1}$ [11]. Since the contribution of the Fermi liquid effects in the electron–electron collisions to the electric conductivity of nontransition

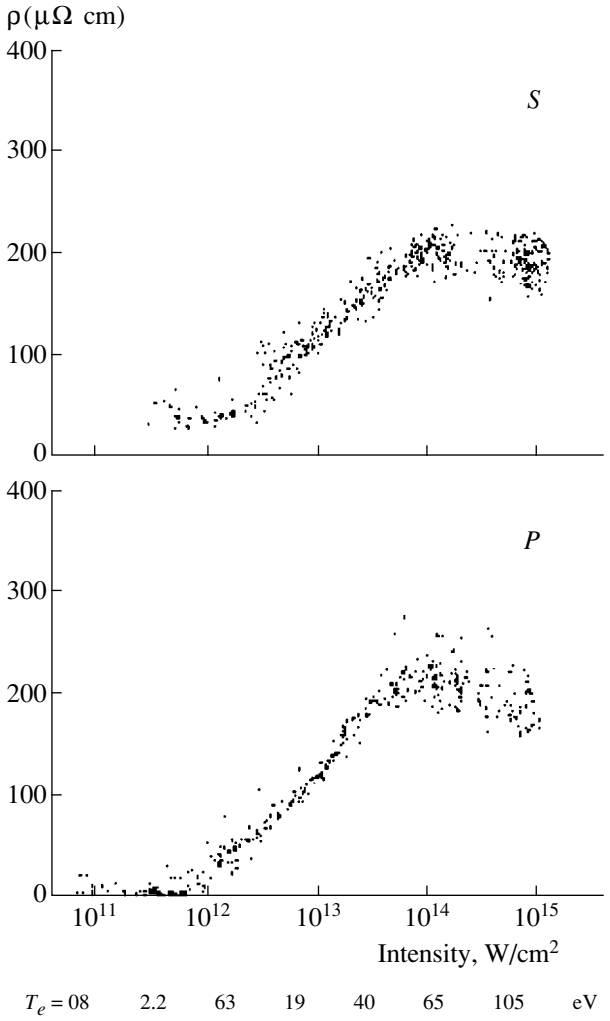

Fig. 1. Experimental curves of the resistivity of aluminum plasma possessing a solid-state density versus the intensity of 400-fs laser radiation pulses [1] (each point corresponds to an independent experiment).

metals (plasmalike media) is negligibly small [13] and the violation of quasineutrality is hindered (a time scale of this violation is provided by the electron plasma frequency, which is equal for aluminum $\omega_{pe} = 1.384 \times 10^{16}$ s^{-1}), we believe that the resistivity of aluminum plasma under the experimental conditions studied in [1] is determined by scattering on the density fluctuations excited by the ion-acoustic oscillations.

Let us confirm this statement. For this purpose, we will use the plasma model of a metal developed previously [14]. According to this model, the electron transport in a locally equilibrium plasmalike medium (a normal nonmagnetic metal) and the density fluctuations in the longwave approximation are determined by the factor $G = \kappa_s (n k_B T_i)^{-1} = C_s^2 C_{\text{Ti}}^{-2}$ ($C_{Ti} = (k_B T_i m_i^{-1})^{1/2}$ being the isothermal sound velocity at $\gamma = 1$ and $\kappa_s = \rho (dP/d\rho)_T$ being the hydrostatic compressibility modulus). In the case of a strongly nonisothermal (nonequi-

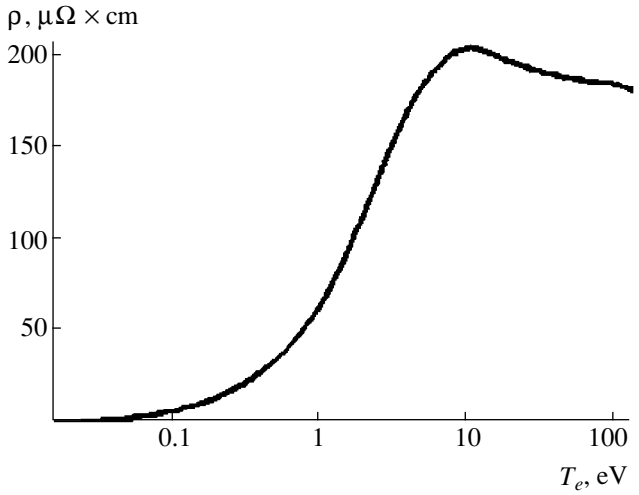

Fig. 2. A theoretical curve of resistivity versus electron temperature for an aluminum plasma of solid-state density.

librium) plasma with solid-state density, this factor can be expressed as follows:

$$G = \frac{C_s^2}{C_{si}^2} = \frac{\kappa_s}{nk_BT_e}. \quad (1)$$

According to this expression, the asymptotic behavior of a nonisothermal ideal plasma corresponds to $G \propto T_e/T_i$.

Substituting Eq. (1) into an expression for the electric conductivity derived in the plasma metal model, we obtain the following formula for the conductivity of a nonisothermal plasma with solid-state density (for simplicity, we neglect the contribution of scattering on the ion core electrons):

$$\sigma = \frac{(2k_BT_e)^{1/2}\kappa_{s0}}{3\pi m_e\tilde{z}n_0e^2\Lambda}\frac{F_3'(x)}{F_{1/2}(x)}, \quad x = \frac{\mu_{\text{eff}}}{k_BT_e}. \quad (2)$$

In Eq. (2), μ_{eff} is the effective chemical potential;

$$F_\nu(x) = \int_0^\infty \frac{z^\nu dz}{\exp(z-x)-1}$$

is the Fermi function of the νth order; $F_\nu'(x) = dF_\nu(x)/dx$;

$$\Lambda = b_1^4\int_0^{\frac{2k\Theta}{q_DT_{i0}}} \frac{\zeta^4 d\zeta}{(\exp(\zeta)-1)(1+b_1^2\zeta^2)^2}, \quad b_1 = \frac{q_D}{k_D}\frac{T_{i0}}{\Theta}$$

is the effective Coulomb logarithm; $q_D \sim r_s^{-1}$ is the Debye wavenumber of a lattice subsystem of the nonideal plasma; $k_D^2 = \min\{k_s^2, k_{ei}^2\}$ ($k_s^2 = r_s^{-2}$; $k_{ei}^2 = k_{De}^2 + (k_{Di}^4 + k_s^4)k_{Di}^{-2}$ [15], k_{De}, k_{Di} being the Debye wavenumbers of electrons and ions, respectively);

$$k = \frac{1}{\hbar}\left(2m_ek_BT_e\frac{F_{3/2}(x)}{F_{1/2}(x)}\right)^{1/2}$$

is the wavenumber of the conduction electron; T_{i0} = 300 K is the ion (lattice) temperature; $n_0 = \rho_0 m_i^{-1}$; and $\kappa_{s0} = \kappa_s(\rho_0)$.

Figure 2 shows variation in the resistivity of the aluminum plasma calculated using Eq. (2) to obtain the conductivity and Eq. (1) to obtain the structural factor. This resistivity curve corresponds to a change in the effective Coulomb logarithm from $\Lambda_0 = 0.684$ at $T_e = T_{i0} = 300$ K to $\Lambda_\infty = 0.491$ at $T_e \geq 0.4$ eV. A comparison of Figs. 1 and 2 shows that the experimental and theoretical resistivity curves qualitatively agree. From this we infer that it is necessary to formulate and solve the problem of the kinetic instability development of this type of ion-acoustic and small-scale turbulence in metals under the action of ultrashort high-power laser radiation pulses.

The situation considered above is characterized by the existence of "cold" ions with a solid-state density and "hot" electrons with the mean free path markedly exceeding the average interatomic distance r_s. An analogous situation takes place in normal metals at low temperatures, where (due to the small number of phonons) the mean free path of the conduction electrons markedly exceeds the interatomic distance. In this case, the conduction electrons deform the lattice, thus producing excitation in it. This leads eventually to an increase in the effective scattering cross section and to the limitation of the electron mean free path. A theoretical interpretation of the nonlinear dynamics of conduction electrons in this system requires a consistent consideration of the nonlinear lattice dynamics to be undertaken jointly with the kinetic equations for the quasiparticle excitations (conduction electrons and phonons) in the deformed lattice. The most consistent consideration of this problem for a quasistationary electric field and a defectless metal in a quasiclassical approximation was carried out by Andreev and Pushkarov [16]. In [17], the joint dynamics of conduction electrons, phonons, and topological defects (dislocations and disclinations) in a current-carrying plasma-like medium (normal metal) was also considered for a quasistationary electromagnetic field in a quasiclassical approximation. It was shown that the passage of the electric current leads to the production of topological defects and, hence, increases the effective electron scattering cross section [18].

In [16, 17], the dynamics of conduction electrons in a deformed lattice was considered within the framework of a quasiclassical kinetic equation that cannot be applied to the study of interaction between ultrashort high-power laser radiation pulses and metal. Problems

in metallooptics are frequently solved using the Gurzhi quantum kinetic equation [19] derived under the assumption that the electron interaction with phonons and electromagnetic field in a nondeformed defect-free metal is small, which is valid for $\hbar\omega \geq k_B T$. Since the photon occupation numbers are always markedly greater than unity, the electromagnetic field in this theory [19] is considered as an external nonquantized field obeying the classical Maxwell equations. Vo Khong An [20] constructed a linear theory describing the parametric interaction of the high-power electromagnetic radiation with nondeformable solids in the random phase approximation. A theoretical description of the high-power laser action upon metals requires the generalization of the methods developed in [12, 16–20]. The electromagnetic field can still be considered as an external classical field, while the lattice deformation of a defectless metal can be described either within the framework of a nonlinear or weakly nonlinear elasticity theory (because the ion-acoustic oscillations are longwave) or using a nonlinear model of a metal with topological defects analogous to the model developed in [17]. The quantum kinetic equation for electrons must take into account their heating and interband transitions (ion-recombination and radiative) and pass into a quasiclassical kinetic equation upon removal of the degeneracy of the conduction electrons.

Thus, we have explained the experimental data reported by Milchberg, Freeman *et al.* [1] on the absorption of intense 400-fs laser radiation pulses in an aluminum target, demonstrated a need in the theoretical study of small-scale (kinetic) instabilities and the ion-acoustic turbulence in the nonequilibrium plasma possessing a solid-state density, and discussed the possible approaches to this analysis. In the future we are planning to construct and study a self-consistent model describing the interaction of a high-power laser radiation with metals, which will consider a multiparticle system of quasiparticle excitations (photons, phonons, conduction electrons, and plasmons) in a deformed lattice, generally, with topological defects.

REFERENCES

1. N. M. Milchberg, R. R. Freeman, S. C. Davey, and R. M. More, Phys. Rev. Lett. **61**, 2364 (1988); N. M. Milchberg and R. R. Freeman, Phys. Fluids B **2**, 1395 (1990).
2. N. Bloembergen, Rev. Mod. Phys. **71**, S283 (1999).
3. V. I. Emel'yanov and D. V. Babak, Fiz. Tverd. Tela (St. Petersburg) **41**, 1462 (1999) [Phys. Solid State **41**, 1338 (1999)].
4. M. B. Agranat, S. I. Anisimov, S. I. Ashitkov, *et al.*, Zh. Éksp. Teor. Fiz. **115**, 675 (1999) [JETP **88**, 370 (1999)].
5. E. L. Clark, K. Kruchelnick, J. R. Davies, *et al.*, Phys. Rev. Lett. **84**, 670 (2000).
6. T. Nichikawa, H. Nakano, N. Versugi, *et al.*, Appl. Phys. Lett. **75**, 4079 (1999).
7. G. Petite, in *Proceedings of the 1st International Congress on Radiation Physics, High Current Electronics, and Modification of Materials, Tomsk, Russia, 2000*, Ed. by D. Vaisburd (Vodolei, Tomsk, 2000), Vol. 1, p. 13.
8. I. T. Yakubov, Usp. Fiz. Nauk **163** (5), 35 (1993) [Phys. Usp. **36**, 365 (1993)]; Teplofiz. Vys. Temp. **33**, 833 (1995).
9. L. A. Artsimovich and R. Z. Sagdeev, *Plasma Physics for Physicists* (Atomizdat, Moscow, 1979).
10. V. L. Ginzburg and V. P. Shabanskiĭ, Dokl. Akad. Nauk SSSR **100**, 445 (1955); M. I. Kaganov, I. M. Lifshits, and L. V. Tanatarov, Zh. Éksp. Teor. Fiz. **31**, 232 (1956) [Sov. Phys. JETP **4**, 173 (1957)].
11. A. A. Galeev and R. Z. Sagdeev, in *Reviews of Plasma Physics*, Ed. by M. A. Leontovich (Atomizdat, Moscow, 1973; Consultants Bureau, New York, 1979), Vol. 7.
12. V. Yu. Bychenkov, V. P. Silin, and S. A. Uryupin, Phys. Rep. **164**, 119 (1988).
13. V. L. Ginzburg and V. P. Silin, Zh. Éksp. Teor. Fiz. **29**, 64 (1955) [Sov. Phys. JETP **2**, 46 (1956)]; V. P. Silin, Fiz. Met. Metalloved. **7**, 331 (1959).
14. N. B. Volkov, Zh. Tekh. Fiz. **49**, 2000 (1979) [Sov. Phys. Tech. Phys. **24**, 1128 (1979)]; N. B. Volkov and A. Z. Nemirovsky, J. Phys. D **24**, 693 (1991); N. B. Volkov, Author's Abstract of Doctoral Dissertation in Mathematical Physics (Inst. Élektrofiz. Ural. Otd. Ross. Akad. Nauk, Yekaterinburg, 1999).
15. I. M. Bespalov and A. Ya. Polishchuk, Preprint No. 1-257, IVTAN (Institute of High Temperatures, Russian Academy of Sciences, Moscow, 1988).
16. A. F. Andreev and D. I. Pushkarov, Zh. Éksp. Teor. Fiz. **89**, 1883 (1985) [Sov. Phys. JETP **62**, 1087 (1985)].
17. N. B. Volkov, J. Phys. A **30**, 6391 (1997).
18. N. B. Volkov, in *Proceedings of the 1st International Congress on Radiation Physics, High Current Electronics, and Modification of Materials, Tomsk, Russia, 2000*, Ed. by G. Mesyats, B. Kovalchuk, and G. Remnev (Vodolei, Tomsk, 2000), Vol. 2, p. 94.
19. R. N. Gurzhi, Zh. Éksp. Teor. Fiz. **33**, 451 (1957) [Sov. Phys. JETP **6**, 352 (1958)]; K. P. Gurov, *Foundations of Kinetic Theory* (Nauka, Moscow, 1966).
20. Vo Hong Anh, *Theory of the Parametric Action of High Power Electromagnetic Radiation on Solids* (Nauka, Moscow, 1985).

Translated by P. Pozdeev

Technical Physics Letters, Vol. 27, No. 3, 2001, pp. 240–244. Translated from Pis'ma v Zhurnal Tekhnicheskoĭ Fiziki, Vol. 27, No. 6, 2001, pp. 50–58.

A Two-Dimensional Distributed Feedback Used for Synchronization of a Multibeam Planar Free-Electron Maser System

N. S. Ginzburg*, N. Yu. Peskov*, A. S. Sergeev*, A. V. Arzhannikov, and S. L. Sinitskiĭ****

** Institute of Applied Physics, Russian Academy of Sciences, Nizhni Novgorod, Russia*

*** Budker Institute of Nuclear Physics, Siberian Division, Russian Academy of Sciences, Novosibirsk, Russia*

Received August 8, 2000

Abstract—We suggest to use a two-dimensional distributed feedback for synchronizing the radiation of a multibeam generator representing a system of planar free-electron maser (FEM) units, each FEM being power supplied with a ribbon-shaped relativistic electron beam. It is demonstrated that various FEM units can be coupled by transverse electromagnetic energy fluxes arising in two-dimensional Bragg structures. © *2001 MAIK "Nauka/Interperiodica".*

Introduction. At present, rather extensive theoretical [1–4] and experimental [5–7] investigations are devoted to the use of two-dimensional (2D) distributed feedback in the generation of high-power coherent radiation by relativistic electron beams of a ribbon or annular geometry. This distributed feedback mechanism can be implemented with the aid of 2D Bragg resonators with planar or coaxial geometry. Theoretical analysis shows that both configurations may ensure the generation of spatially coherent radiation, provided that one of the transverse system dimensions is several orders of magnitude greater than the radiation wavelength.

The functionality of this 2D distributed feedback system was recently demonstrated by Agarin *et al.* [5, 6] in experiments with a free electron maser (FEM) operating in the 4 mm wavelength range. The FEM was based on a special electron accelerator of the ELMI type (Budker Institute of Nuclear Physics, Novosibirsk) capable of producing a pulsed ribbon relativistic electron beam (REB) with a particle energy of 1 MeV, a linear current density of 200 A/cm, a cross section of 0.3×20 cm, and a pulse duration above 5 μs. In the development of these investigations, it is planned to create high-power electromagnetic radiation sources based on a synchronously operating generator or modular structures amplifier composed of planar FEM units adjoining one another so as to form a unified system with a multilayer electrodynamic structure and spatial coupling in two transverse coordinates.

Below we will demonstrate that synchronization of the oscillation phase can be attained by coupling various units with transverse (relative to the direction of the particle propagation) fluxes of electromagnetic energy arising in two-dimensional Bragg structures. This approach allows the realization of both generator and amplifier systems. In the former case, it is necessary to provide for the circular closing of energy fluxes from the first and last system units. In the latter case, the circle is broken and the ends are used as signal inputs. The first experimental verification of the proposed synchronization mechanism planned on the ELMI facility will consist in combining two planar masers so as to form a unified system.

System description. Figure 1a shows a general scheme of a multiunit FEM generator. Each FEM unit (Fig. 1b) represents an oscillator with a 2D planar Bragg resonator, the plates of which are corrugated according to the law

$$a = a_1 \cos(\bar{h}z)\cos(\bar{h}x), \qquad (1)$$

where $\bar{h} = \sqrt{2}\,\pi/d$, d is the corrugation period, and $2a_1$ is the corrugation profile depth. Each FEM unit is power supplied with a ribbon-shaped REB propagating along the z-axis. Electrons in the REB, focused with a guiding magnetic field, oscillate in the field of a planar undulator adjoining each FEM unit. Various units are coupled in series by transverse energy fluxes arising as a result of the electron scattering accompanying the excitation of the 2D Bragg resonators with the ribbon REBs. In order to close the feedback circle, the first and last FEM units must be also coupled to one another.

The electromagnetic field inside each FEM unit can be represented as a sum of four partial waves, two of which ($\mathcal{A}_\pm$) are propagating in the longitudinal direction and two other ($\mathcal{B}_\pm$), in the transverse direction rel-

ative to the REB propagation direction:

$$\mathbf{E} = \mathbf{E}_0 \mathrm{Re}([\mathscr{A}_{+,n} e^{-i\bar{h}z} + \mathscr{A}_{-,n} e^{i\bar{h}z} + \mathscr{B}_{+,n} e^{-i\bar{h}x} + \mathscr{B}_{-,n} e^{i\bar{h}x}] e^{i\bar{\omega}t}). \quad (2)$$

Here, $\mathscr{A}_{\pm}(x, z, t)$ and $\mathscr{B}_{\pm}(x, z, t)$ are slowly-varying functions and $\bar{\omega} = \bar{h}c$ is the carrier frequency (selected equal precisely to the Bragg resonance value).

The electron-wave interaction in the nth FEM unit can be described by the following set of equations (cf. [2, 3]):

$$\left(\frac{\partial}{\partial Z} + \beta_{gr}^{-1}\frac{\partial}{\partial \tau}\right)A_{+,n} + i\alpha(B_{+,n} + B_{-,n}) = J_n,$$

$$J_n = \frac{1}{\pi}\int_0^{2\pi} e^{-i\theta_n} d\theta_{0n},$$

$$\left(\frac{\partial}{\partial Z} - \beta_{gr}^{-1}\frac{\partial}{\partial \tau}\right)A_{-,n} + i\alpha(B_{+,n} + B_{-,n}) = 0, \quad (3)$$

$$\left(\frac{\partial}{\partial X} \pm \beta_{gr}^{-1}\frac{\partial}{\partial \tau}\right)B_{\pm,n} + i\alpha(A_{+,n} + A_{-,n}) = 0,$$

$$\left(\frac{\partial}{\partial Z} + \beta_{\|}^{-1}\frac{\partial}{\partial \tau}\right)^2 \theta_n = \mathrm{Re}(A_{+,n} e^{i\theta_n}),$$

where $Z = z\bar{h}C$, $X = x\bar{h}C$, $\tau = t\bar{\omega}C$, $(A_{\pm}, B_{\pm}) = (\mathscr{A}_{\pm}, \mathscr{B}_{\pm})eK\mu/\gamma m\bar{\omega}cC^2$; $K \approx \beta_{\perp}/2\beta_{\|}$ is the electron–wave coupling parameter; $\mu \approx \gamma^{-2}$ is the inertial group parameter; γ is the relativistic electron mass factor; $v_{\|,\perp} = \beta_{\|,\perp}c$ are the propagatory and oscillatory particle velocities, respectively; $v_{gr} = \beta_{gr}c$ is the wave group velocity; $\theta = \bar{\omega}t - hz - h_w z$ is the electron phase relative to the synchronous wave; $h_w = 2\pi/d_w$, d_w is the undulator period;

$$C = \left(\frac{eI_0}{mc^3}\frac{\lambda^2 \mu K^2}{8\pi\gamma a_0}\right)^{1/3}$$

is the gain factor (Pierce parameter), I_0 is the beam linear current density; a_0 is the distance between plates; α is the wave coupling coefficient in the 2D Bragg structure, which is proportional to the corrugation profile depth a_1 [1, 2].

The boundary conditions for the electron beam and the partial waves propagating along the beam (parallel to the z-axis) can be formulated as follows:

$$A_{+,n}\big|_{Z=0} = 0, \quad A_{-,n}\big|_{Z=L_z} = 0, \quad (4)$$

$$\theta_n\big|_{Z=0} = \theta_{0n} \in [0, 2\pi),$$

$$\left(\frac{\partial}{\partial Z} + \beta_{\|}^{-1}\frac{\partial}{\partial \tau}\right)\theta_n\big|_{Z=0} = \Delta_n, \quad (5)$$

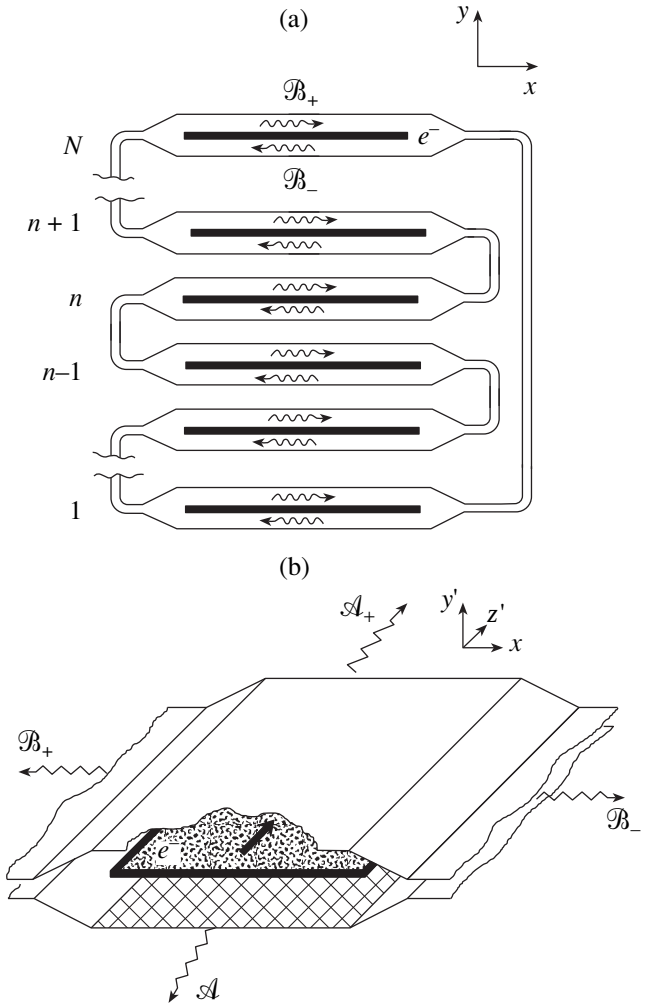

Fig. 1. Schematic diagrams of (a) a multibeam FEM system composed of N planar units (for each unit, the cross section shows a ribbon REB and the transverse electromagnetic energy fluxes) and (b) an individual FEM unit with 2D Bragg resonator power supplied with a ribbon REB.

where L_z is the FEM unit length and $\Delta_n = (\bar{\omega} - h v_{\|} - h_w v_{\|})/\bar{\omega}C$ is the initial undulator synchronism detuning at the carrier frequency in the nth unit. For the partial waves propagating in the transverse direction, which provide for the coupling between various units, the boundary conditions are as follows:

$$[B_{+,n}(\tau) = \Gamma B_{-,n-1}(\tau - T)]_{X=0},$$
$$[B_{-,n}(\tau) = \Gamma B_{+,n+1}(\tau - T)]_{X=L_x},$$
$$[B_{-,N}(\tau) = \Gamma^N B_{+,1}(\tau - NT)]_{X=L_x}, \quad (6)$$
$$[B_{-,1}(\tau) = \Gamma^N B_{+,N}(\tau - NT)]_{X=L_x},$$

where L_x is the FEM unit lateral size, T is the delay time for the signal propagation between neighboring units,

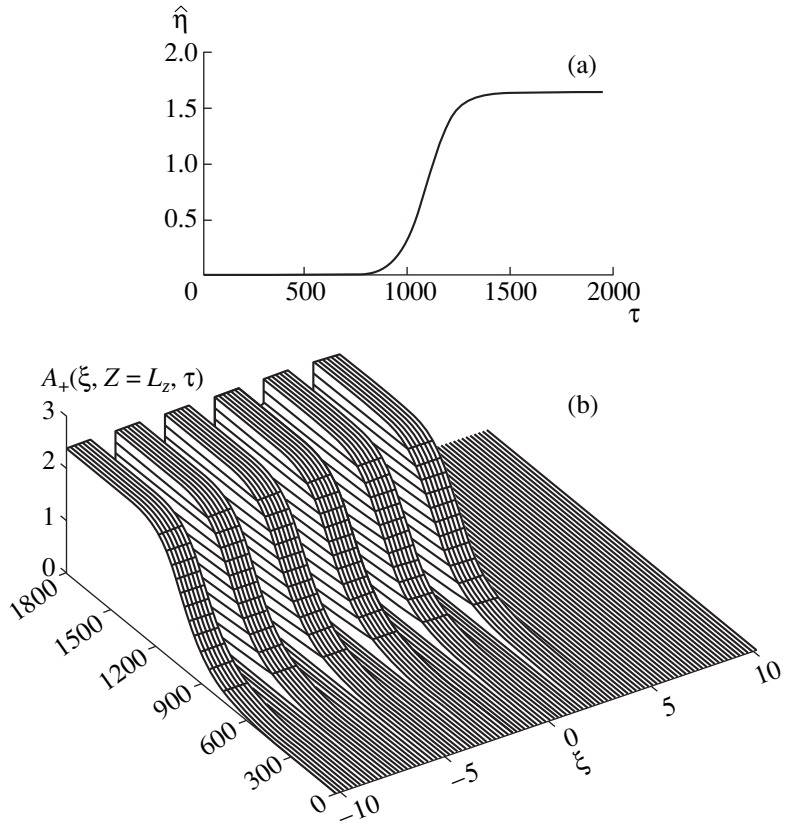

Fig. 2. Modeling of the process of establishing a self-oscillation regime in a six-unit ($N = 6$) FEM generator: (a) plot of the normalized integral electron efficiency; (b) wave amplitude distribution in the output cross section $Z = L_z$ ($L_z = 6.8$, $L_x = 1.2$, $T = 1.2$, $\alpha = 0.1$, $\Delta = -0.2$, $\Gamma = 0.95$).

and $\Gamma < 1$ is the ohmic loss factor. For the coupling between terminal units, the delay time was naturally taken equal to be NT, where N is the total number of units.

Thus, the FEM units are in fact linked in a circle (Fig. 1a) and the process of synchronized self-oscillations in the system of N units is generally analogous to that in a FEM generator with a coaxial 2D Bragg resonator [3]. It should be also noted that, similar to a FEM with axial geometry, the presence of ohmic losses for the $\mathcal{B}_\pm$ waves is a condition necessary for establishing a stationary self-oscillation regime in the system.

Modeling results. The process of FEM unit synchronization was modeled using parameters close to the conditions of experiments planned on the ELMI accelerator. The oscillatory velocity $\beta_\perp = 0.2$–0.25 was imparted to the particles in an active planar undulator with a period of 4 cm, a transverse undulator field component up to 0.2 T, and a guiding field strength of 1 T. The width of separate beams was taken equal to 15 cm at a linear current density of ~200 A/cm. Thus, the Pierce parameter at a frequency of 75 GHz was equal to $C \approx 4 \times 10^{-3}$. Figures 2 and 3 present the results of modeling the synchronization process for a system of six generator units with a reduced normalized interaction space width of $L_x = 1.2$ (corresponding to $l_x = 20$ cm for the ELMI experiment) a module length of $L_z = 6.8$ ($l_z = 110$ cm), a normalized delay time of $T = 1.2$ (0.67 ns), and the ohmic loss factor $\Gamma \approx 0.95$.

Figure 2 illustrates the process of establishing a steady-state generation regime. The oscillation frequency in the established regime is close to the exact value of the Bragg resonance frequency. Figure 2a presents a plot of the integral efficiency (for all FEM units) and Fig. 2b shows a distribution of the field A_+ in the output cross section $Z = L_z$. The coordinate ξ is introduced to describe the field distribution over the entire system contour including all FEM units and coupling waveguides. Figure 3 shows a spatial distribution of the field for a synchronous wave A_+ and one of the transverse waves B_+ involved in synchronization of the FEM units.

It is important to emphasize that synchronization takes place even when various units are power supplied by electron beams possessing somewhat different energies and, hence, different values of the synchronism detuning Δ_n. For the geometric parameters under consideration, the self-excitation and synchronization of

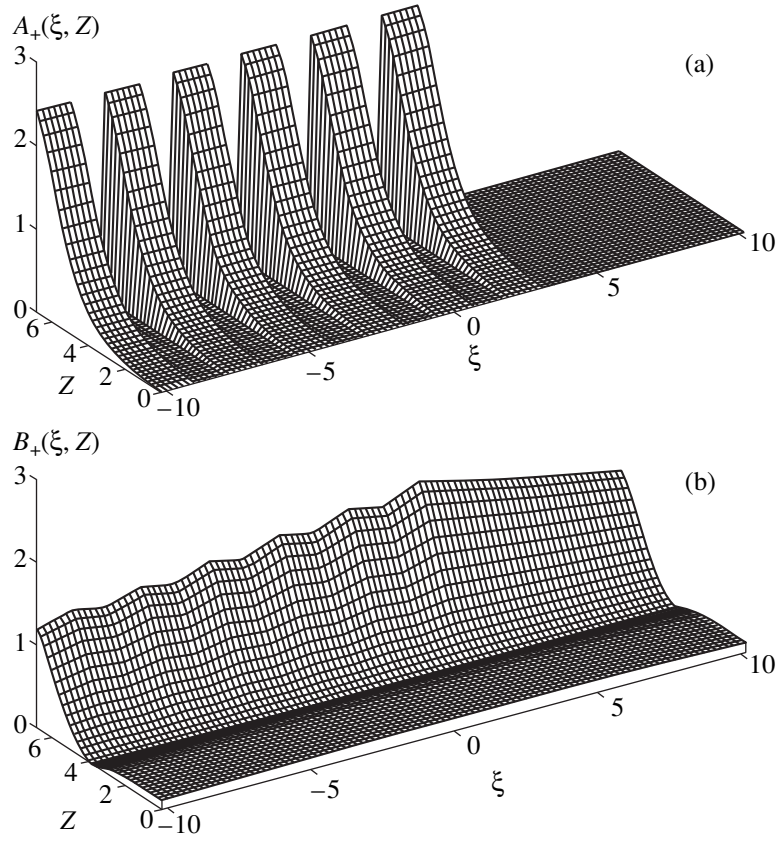

Fig. 3. A spatial distribution of the field amplitudes for the partial waves (a) $\mathcal{A}_+$ and (b) $\mathcal{B}_+$ in a steady-state generation regime for the same FEM parameters as in Fig. 2.

various units took place for a relative scatter of the detuning as large as 50% of the self-excitation bandwidth, but a greater scatter led to the breakdown of oscillations. The modeling revealed no cases of synchronization breakage followed by various units generating at different frequencies.

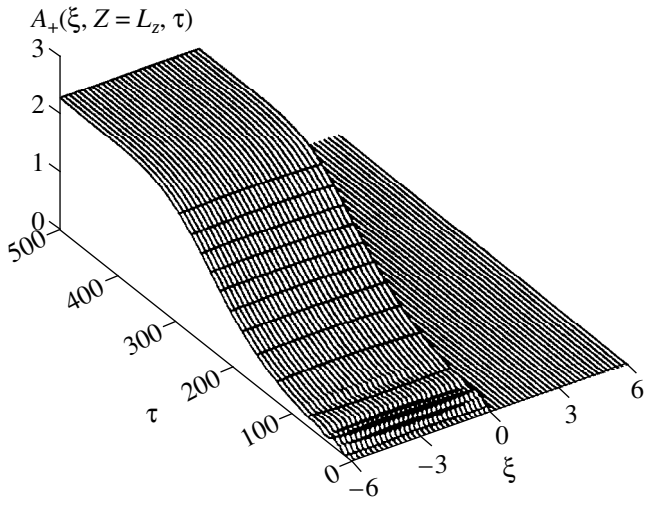

Fig. 4. Modeling of the process of establishing a self-oscillation regime in a single-unit ($N = 1$) planar FEM generator with closed transverse electromagnetic fluxes. A plot of the wave field amplitude distribution in the output cross section $Z = L_z$ ($L_z = 6.8$, $L_x = 6$, $T = 6$, $\alpha = 0.1$, $\Delta = 0$, $\Gamma = 0.95$).

Conclusion. It should be noted that the transverse synchronization of radiation in the generator, provided by closing the boundaries of the interaction space, can be also effective in the case of a single unit. As was demonstrated previously [1–3], use of the 2D distributed feedback prompts an almost unlimited increase in the width of the interaction space in the case of systems open in the transverse direction. At the same time, a considerable advantage from the standpoint of practical implementation is offered by systems closed in the transverse direction.

It was demonstrated [4] that the problem can be partly solved by using FEMs with combined resonators composed of 1D and 2D planar Bragg mirrors. Using an additional waveguide closing the transverse energy fluxes from terminal units can be considered as an alternative solution, offering an advantage of higher selectivity with respect to the transverse index. Figure 4 illustrates the formation of a transverse distribution of the output radiation amplitude, which corresponds to establishing a steady-state generation regime with a frequency coinciding with the Bragg resonance value.

REFERENCES

1. N. S. Ginzburg, N. Yu. Peskov, and A. S. Sergeev, Pis'ma Zh. Tekh. Fiz. **18** (9), 23 (1992) [Sov. Tech. Phys. Lett. **18**, 285 (1992)].
2. N. S. Ginzburg, N. Yu. Peskov, A. S. Sergeev, *et al.*, Phys. Rev. E **60**, 935 (1999).
3. N. S. Ginzburg, N. Yu. Peskov, and A. S. Sergeev, Opt. Commun. **112**, 151 (1994).
4. N. S. Ginzburg, N. Yu. Peskov, A. S. Sergeev, *et al.*, Pis'ma Zh. Tekh. Fiz. **26** (16), 8 (2000) [Tech. Phys. Lett. **26**, 701 (2000)].
5. N. V. Agarin, A. V. Arzhannikov, V. B. Bobylev, *et al.*, in *Proceedings of the 4th International Workshop "Strong Microwaves in Plasmas," Nizhni Novgorod, Russia, 1999*, p. S24.
6. N. V. Agarin, A. V. Arzhannikov, V. B. Bobylev, *et al.*, in *Abstracts of the 21st International Free Electron Laser Conference, Hamburg, Germany, 1999*, p. Mo-O-04.
7. A. D. R. Phelps, A. W. Cross, G. R. M. Robb, *et al.*, in *Proceedings of the 19th International Free Electron Laser Conference, Beijing, China, 1997*, p. II-122.

Translated by P. Pozdeev

Technical Physics Letters, Vol. 27, No. 3, 2001, pp. 245–247. Translated from Pis'ma v Zhurnal Tekhnicheskoĭ Fiziki, Vol. 27, No. 6, 2001, pp. 59–64.

Microwave Pulses Compressed in a Barrel-Shaped Resonator with Screw Corrugation

Yu. Yu. Danilov, S. V. Kuzikov, V. G. Pavel'ev, and Yu. I. Koshurinov

Institute of Applied Physics, Russian Academy of Sciences, Nizhni Novgorod, Russia

e-mail: danilov@appl.sci-nnov.ru

Received July 7, 2000

Abstract—The microwave pulse compressor proposed previously [1], having the form of an oversized waveguide resonator with a screw-corrugated inner surface, was constructed and experimentally tested. A fivefold compression of microwave pulses with a 70% efficiency was obtained in a 3-cm wavelength range. *© 2001 MAIK "Nauka/Interperiodica".*

Introduction. A possible method of compressing microwave pulses consists in transmitting a phase-modulated pulse via a circular resonator [2, 3]. The energy parameters of such resonators are usually limited by breakdown in the element coupling the resonator to a waveguide.

Recently [1], we proposed a variant of the circular resonator based on an axisymmetric metal waveguide structure (Fig. 1) comprising several sections with various diameters connected by sloping junctions. The intrinsic oscillations of the resonator are confined within a slightly expanded middle section between supercritical narrowings. The coupling of a wave passing through the resonator to the working mode (of a rotating whispering-gallery type) is provided by a screw corrugation pattern on the inner surface of the resonator. The corrugation has a small height compared to the wavelength, and the geometric parameters obey the conditions [1]

$$m_j - m_s = \bar{m}, \quad h_j \approx \bar{h} = \frac{2\pi}{d},$$

where $\bar{m}$ and d are the number of threads and pitch of the screw, respectively; m_s is the azimuthal index of the resonant mode; and m_j and h_j are the azimuthal index and propagation constant of the transmitted wave, respectively. Reirradiation into spurious modes is suppressed by selecting the resonator and waveguide modes rotating in opposite directions.

Resonator design. The experiments were performed with a copper resonator having the parameters presented in the table. The resonator operated on a clockwise H_{61} mode with a frequency of 11.39 GHz. Selecting the resonant H mode prevented parasitic scattering on sloping connectors from contributing to the E mode with the same azimuthal index. The energy was supplied to and extracted from the resonator with a counterclockwise H_{41} mode. The resonator was first calculated by an approximate analytical method [1] and then numerically refined by a modified method of planar transverse cross sections [4, 5].

The energy was supplied to the compressor via a standard rectangular waveguide with a 23 × 10 mm cross section using an H_{10} wave with a system converting this wave into the H_{41} mode. The conversion system

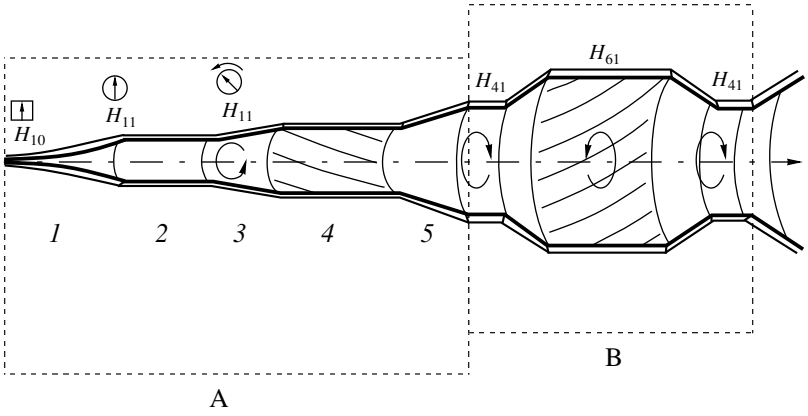

Fig. 1. Schematic diagram of the compressor: (A) mode converter; (B) circular resonator (see the text for explanations).

1063-7850/01/2703-0245$21.00 © 2001 MAIK "Nauka/Interperiodica"

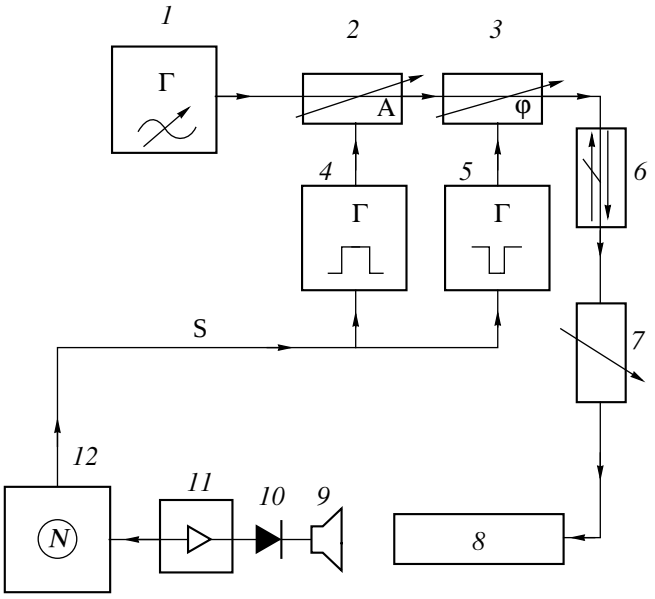

Fig. 2. Schematic diagram of the experimental setup. S is the synchronizing signal (for other notations see the text).

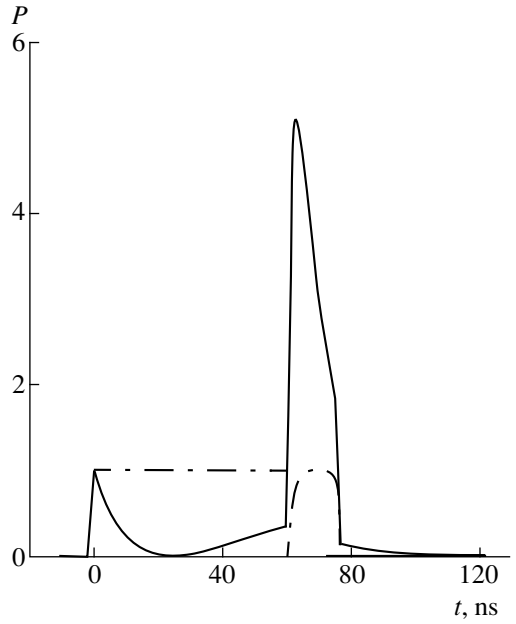

Fig. 3. Typical oscillograms of the (dashed) input and (solid) output microwave power pulses.

included the following elements (Fig. 1): (*1*) a standard junction from a rectangular waveguide with a H_{10} working mode to a circular waveguide with a H_{11} working mode; (*2*) an elliptic-waveguide polarizer with a clockwise-polarized H_{11} wave at the output; (*3*, *5*) conical junctions; (*4*) a circular waveguide with a five-thread screw corrugation converting the clockwise H_{11} wave into a counterclockwise H_{41} wave. The calculated efficiency of conversion in this system is ≈98%.

Experimental setup and results. The input pulses were compressed using the so-called SLED scheme [2, 3]. Along most of the input pulse length, the resonator accumulates microwave energy and reirradiates this energy into the waveguide with a phase opposite to that of the transmitted wave. At a certain time before the pulse end, the input signal phase is inverted and the transmitted wave adds to that irradiated from the resonator.

Resonator parameters

Smooth section length, mm	45.06
Conical junction length, mm	10.41
Corrugated section length, mm	59.59
Smooth section diameter, mm	59.84
Corrugated section diameter, mm	63.54
Number of threads	10
Screw pitch	37.08
Corrugation height, mm	0.125
Loaded Q (experimental value)	1140
Transmission line coupling factor (experimental value)	14

Figure 2 shows a schematic diagram of the experimental setup including the following elements: (*1*) microwave generator; (*2*) amplitude modulator; (*3*) electrically controlled phase-rotating circuit (implementing two FETs) with a characteristic time of 1 ns;[1] (*4*, *5*) pulse generators; (*6*) ferrite switch; (*7*) high-precision attenuator; (*8*) mode converter and circular resonator (Fig. 1); (*9*) horn antenna; (*10*) detector; (*11*) microwave amplifier; (*12*) oscillograph.

Figure 3 shows typical oscillograms of the input and output pulses. The compressor operation is conventionally characterized by the compression factor (equal to the ratio of the input and output pulse durations),[2] efficiency (equal to the ratio of energies stored in the output and input pulses), and power gain (a product of the compression factor by the efficiency) [2, 3]. According to Fig. 3, the system ensuring a fivefold pulse compression had an efficiency of ≈70% and a power gain of ≈3.5. These values agree well with the results of calculations using the experimental parameters. The oscillogram of the output pulse deviates from the calculated curve by no more than 5%; the difference is apparently related to uncertainty in the system manufacture and adjustment, as well as to experimental errors.

[1] By the characteristic time of the phase-rotating circuit we imply the value $\tau_f = t_0/\ln 2$, where t_0 is the time of the input pulse power decay to zero during the phase reversal.

[2] By the input pulse duration we imply that of the flat pulse top equal to 75 ns [3]; the output pulse duration is defined as the time period from the phase-rotating circuit switch on to the input pulse termination.

Conclusion. The results of the model experiment described above showed the possibility of effectively compressing microwave pulses using the proposed resonator design. Application of the resonator in accelerator technology would require the passage to spatially developed modes. According to [3], the intrinsic Q value of the resonator must be not less than 100000, which implies that the resonant mode must be of the E type and possess an azimuthal index of not less than ~15.

Acknowledgments. The authors are grateful to M.I. Petelin for his permanent interest in this study.

This work was supported by the Russian Foundation for Basic Research, project nos. 96-02-16217 and 99-02-17781.

REFERENCES

1. Yu. Yu. Danilov, S. V. Kuzikov, and M. I. Petelin, Zh. Tekh. Fiz. **70** (1), 65 (2000) [Tech. Phys. **45**, 63 (2000)].
2. Z. D. Farcas, H. A. Hogg, G. A. Loew, and P. B. Wilson, in *Proceedings of the 9th Conference on High Energy Accelerator, SLAC, Stanford, 1974*, p. 576.
3. V. E. Balakin and I. V. Syrachev, in *Proceedings of the 3rd European Particle Accelerator Conference, Berlin, 1992*, p. 1173.
4. Sh. E. Tsimring and V. G. Pavel'ev, Radiotekh. Élektron. (Moscow) **27** (6), 1099 (1982).
5. V. G. Pavel'ev and Sh. E. Tsimring, Radiotekh. Élektron. (Moscow) **32** (6), 1121 (1987).

Translated by P. Pozdeev

Technical Physics Letters, Vol. 27, No. 3, 2001, pp. 248–250. Translated from Pis'ma v Zhurnal Tekhnicheskoĭ Fiziki, Vol. 27, No. 6, 2001, pp. 65–70.

An Active Lasing Region with a Quantum Well and a Quantum Dot Array

V. P. Evtikhiev, O. V. Konstantinov, and A. V. Matveentsev

Ioffe Physicotechnical Institute, Russian Academy of Sciences, St. Petersburg, Russia

Received October 26, 2000

Abstract—A combined active lasing region of the new type, containing an $In_{0.2}Ga_{0.8}As$ quantum well (QW) and a single-layer array of InAs quantum dots (QDs) located outside the QW, was studied. In this system, the QW accumulates the injected charge carriers and the QD array serves as a radiator. The energy levels of electrons and holes in a QD were calculated. It is shown that the QDs can be filled by the resonance tunneling of holes from the QW to an unoccupied QD. The electron energy level in an unoccupied QD is markedly higher than that in the QW, but occupation of the QD by a hole leads to a resonance of the electron levels. Theoretical conclusions agree with the results of observations on a prototype laser with a combined active region. © *2001 MAIK "Nauka/Interperiodica".*

A number of lasers employing quantum dot (QD) arrays have been described. For example, diode lasers with InAs QDs confined between GaAs layers operating at a photon energy of 1.2–1.3 eV were reported in [1, 2]. A distinctive feature of these lasers is the relatively low value of the room-temperature threshold current (~200 A/cm^2). The lasing regions of these devices comprise one or several layers of QDs arranged in an undoped part of the *p–n* structure. Our preliminary experimental investigations showed that certain advantages can be offered by a quantum well (QW) located within a tunneling range near a single-layer QD array: in particular, the quantum yield in this structure is virtually independent of the excitation current.

We have studied a structure comprising a QW and a single layer QD array outside the QW. Our experience showed that the distance between these layers must be on the order of 40 Å. The purpose of this study was to develop a theory that can describe the system parameters for which the energies of electron ionization from the QW and from a QD would coincide. This would provide conditions for the resonance tunneling of holes from the QW to QDs. As is demonstrated below, an $In_{0.2}Ga_{0.8}As$ QW with a thickness of $w = 80$ Å possesses a hole ground level ionization energy virtually coinciding with the hole energy level in an unoccupied QD. The electron energy level in an unoccupied QD lies 25 meV above that in the QW. However, when a hole occupies the QD, the electron level in this QD decreases by 28 meV as a result of the Coulomb interaction between hole and electron. This also provides conditions for a resonance tunneling of electrons from the QW to the QD occupied by the hole. The electron and hole in the QD form a bound exciton. Only bound excitons in the singlet state can produce emission, while the triplet states exhibit a nonradiative recombination by the Auger mechanism. For this reason, the quantum yield (at a relatively low current) in such a system must not exceed 25%, which agrees with experimental observations.

An important feature of the InAs QD confined between GaAs layers is that a quadratic approximation of the dispersion law is inapplicable to electrons in this system because the energy of the electron state is markedly greater than that of the conduction band bottom. As for the energy spectrum of heavy holes, the quadratic approximation holds within rather broad limits. According to the data presented in the reference book [3] and reported in [4], this approximation is valid for hole energies below 0.4 eV. It should be noted that the dispersion laws were calculated in both cited papers using the nonlocal pseudopotential method, which provides the most reliable results. Based on these data, we believe that the hole energy obeys the quadratic dispersion law:

$$E_v(k) = \frac{\hbar^2 k^2}{2m_v}, \quad (1)$$

where k is the wave vector of the hole and $m_v = 0.41m_0$ is the tabulated value of the effective hole mass in InAs. In [4], the energy is expressed in eV and the wave vector, in fractions of its limiting value in the [001] direction $\left(\frac{ka}{2\pi}\right)$, where $a = 6.06$ Å is the InAs crystal lattice constant. The validity of relationship (1) is illustrated by curves in the bottom part of the figure, where the lower and upper dashed curves show the results of the band calculations [4] for the directions parallel to [100] and [111], respectively, while the solid curve represents the standard quadratic dispersion law given by formula (1) with the effective mass equal to the tabulated value. As can be seen, the solid curve occupies

an intermediate position between the dashed ones, the difference between the latter curves reflecting the corrugation of the isoenergetic surfaces of heavy holes.

A quadratic approximation for the electron energy spectrum is valid only within an unacceptably narrow energy interval. However, we have established that semiempirical relationships similar to the Kane formulas provide a sufficiently correct analytical description of the results of numerical calculations performed in [4]. For the electron energy in the conduction band E_c, this approximation yields the following relationship:

$$E_c(k) = \frac{E_g}{2}\left(\sqrt{1+\frac{2\hbar^2k^2}{m_cE_g}}-1\right); \qquad (2)$$

where $E_g = 0.356$ eV is the bandgap width in InAs and m_c is the effective electron mass (considered as a fitting parameter).

Let us consider the E_c value as a function of the wavevector k. The curve calculated by formula (2) is depicted by the thick solid line in the top part of the figure. The calculation was performed for the effective electron mass selected equal to $m_c = 0.057m_0$. Virtually coinciding with the thick solid curve, a dashed curve represents the results of the band calculations obtained in [4]. In addition, the electron energy in the conduction band is characterized by a thin solid curve corresponding to the standard quadratic approximation with a tabulated value of $m_c = 0.027m_0$. As can be seen, this approximation actually leads to very large errors in the electron energies exceeding 0.05 eV. Note that, according to the band calculations [4], the electron energy spectrum is isotropic up to $E_c \approx 1$ eV, where a significant anisotropic contribution appears due to the difference between the L and X valleys.

Now let us proceed to a spherical model of the quantum dot. This model is necessary because equation (2) describing the dispersion law refers to the case of flat bands in an infinite medium. The InAs QDs confined between GaAs layers have the shape of truncated pyramids with rounded vertices whose diameter is 15 Å. The bottom base of the pyramid has an elliptic shape with axes equal to 150 and 170 Å, the pyramid height being 20 Å. A nonparabolic effective mass Hamiltonian is not available for an object possessing such a complicated shape and can be constructed only for a spherical microobject. According to Asryan and Suris [5], the optimum diameter of the sphere modeling an acute pyramid falls between the diameters of inscribed and superscribed spheres, the latter sphere passing through the pyramid vertex and touching the base. In our case, the pyramid shape resembles a throwing discus, and the diameters of inscribed and superscribed spheres differ only slightly. We will assume that the optimum diameter of the model sphere is equal to the height of the nontruncated (acute) pyramid, that is, to the diameter of the superscribed sphere $d = 22.2$ Å. The values of the band

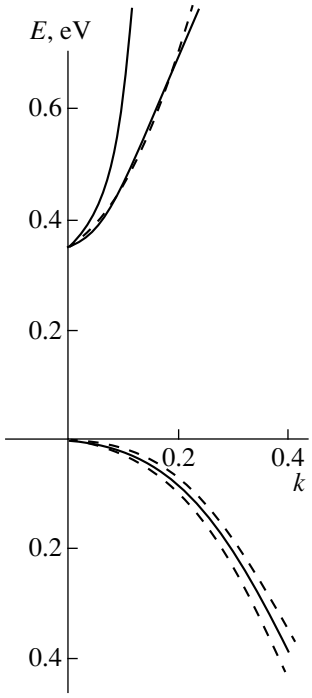

Dispersion laws in the valence (bottom part) and conduction (top part) bands. Dashed curves show the results of calculations performed by the method of pseudopotential [4]. Thick solid curves present the dispersion laws adopted in this study and approximated by Eqs. (1) and (2) for holes and electrons, respectively. The thin solid curve in the top part shows the standard quadratic law of dispersion.

edge breakage at the QD boundaries can be estimated by ignoring deformations related to the lattice mismatch and using the conventional assumptions: $\Delta E_c = 0.65\Delta E_g$ and $\Delta E_v = 0.35\Delta E_g$. For the QD under consideration, $\Delta E_g = 1.072$ eV, and the approximation adopted yields $\Delta E_c = 0.6968$ eV and $\Delta E_v = 0.3752$ eV. These determine the depth of the spherical potential well for electrons and holes.

Let us determine the energies of quantum levels for the charge carriers in these spherical potential wells. The Schrödinger equation for holes contains a kinetic energy operator obtained from formula (1) by substituting the operator $(-i\nabla)$ for the wavevector k. We will seek the spherically symmetric solutions, depending only on the radius and proportional to $\sin(kr)/r$, in order to ensure that the wavefunction is finite in a spherical well with $r = 0$. Dependence of the hole energy (measured from the well bottom) on the wavevector k is still given by formula (1).

For a wide-bandgap material (GaAs) surrounding the model spherical QD, the kinetic energy Hamiltonian is obtained from (1) by substituting the operator $(-i\nabla)$ for the wavevector k and the effective hole mass $m_B^h = 0.45m_0$ (in GaAs), for $m_v = 0.41m_0$. The resulting wavefunction in the wide-bandgap material is De^{-qr}/r. The wavevector k must be determined from the condi-

tion of continuity for the wavefunction Ψ and its derivative at the boundary of the sphere modeling the QD. This yields an equation that is well-known from the handbooks:

$$-x\cot(x) = \sqrt{\frac{\Delta E - E(k)}{E_B}}, \quad x = \frac{kd}{2}, \quad E_B = \frac{2\hbar^2}{m_B d^2}, \quad (3)$$

where m_B is the effective carrier mass in GaAs, d = 22.2 Å is the model sphere diameter, and $E(k)$ is determined by formula (1). It is convenient to modify Eq. (1) by taking its square and introducing the ionization potential $I(x)$ such that

$$I(x) + E(k) = \Delta E, \quad I(x) = E_B x^2 \tan^2\left(x - m\frac{\pi}{2}\right), \quad (4)$$
$$m = 1, 2, \ldots$$

The value m = 1 corresponds to the hole ground state in the QD, while m = 2 corresponds to an excited state not realized for the system parameters studied. Substituting ΔE = 0.375 eV and E_B = 0.069 eV, we obtain I = 0.067 eV.

It must be noted that Eq. (4) is valid for the QW as well. In this case, the hole ground state corresponds to m = 0 and ΔE = 0.075 eV (the well depth for the $In_{0.2}Ga_{0.8}As$ composition). The electron energy in the well is smaller and can be determined in the quadratic approximation. Using Eq. (4) for E_B, one should substitute the QW thickness w for the QD diameter d. For an experimental value of w = 8 nm, we obtain E_B = 0.0053 eV and I = 0.0668 eV. This value virtually coincides with the hole ionization energy in the QD. Similar calculations for electrons in the QW yield ΔE = 0.139 and I = 0.096 eV.

The electron energy in the QD is still determined by Eq. (4), but the $E(k)$ value is taken in the form of Eq. (2). Using the value of the conduction band breakage ΔE = 0.697 eV, we obtain an electron ionization energy of I = 0.071 eV. This value is 25 meV below the electron ionization energy in the QW, which puts these levels significantly out of resonance. The electron tunneling from the QW to an unoccupied QD is possible only provided that an acoustic phonon is simultaneously absorbed. However, filling the QD with a hole decreases the electron energy level by a value equal to the electron–hole interaction energy at a distance of 4 nm, that is by 27 meV.; As a result, the QD occupied by a hole has an electron energy level in resonance with the QW.

Acknowledgments. The authors are grateful to R.A. Suris for a productive discussion of the results.

REFERENCES

1. I. V. Kudryashov, V. P. Evtikhiev, V. E. Tokranov, *et al.*, J. Cryst. Growth **201/202**, 1158 (1999).
2. K. Seeger, *Semiconductor Physics* (Springer-Verlag, Berlin, 1974; Mir, Moscow, 1977).
3. Landolt-Bornstein, *New Series* (Springer-Verlag, Berlin), Vol. III/22a.
4. J. R. Chelikowsky and M. L. Cohen, Phys. Rev. B **14** (2), 556 (1976).
5. L. V. Asryan and R. A. Suris, Semicond. Sci. Technol. **11**, 554 (1996).

Translated by P. Pozdeev

Technical Physics Letters, Vol. 27, No. 3, 2001, pp. 251–253. Translated from Pis'ma v Zhurnal Tekhnicheskoĭ Fiziki, Vol. 27, No. 6, 2001, pp. 71–76.

Data Transfer Using Masking Chaotic Oscillations

É. V. Kal'yanov and V. V. Grigor'yants

Fryazino Department, Institute of Radio Engineering and Electronics, Russian Academy of Sciences, Fryazino, Moscow oblast, Russia

Received June 1, 2000

Abstract—A hidden communication scheme for cable and optical fiber data transfer systems is proposed. A two-channel variant based on using a coded random signal for masking the transmitted data was analyzed by numerical methods. © *2001 MAIK "Nauka/Interperiodica".*

At present, researchers are actively investigating the possibility of using chaotic oscillations for masking transmitted data. One advantage of this masking principle is the potentially higher efficacy of this approach as compared to the conventional one using various methods of data coding [1]. Several possible hidden communication schemes implementing the phenomenon of chaotic synchronization were described in the literature [2–9]. However, the practical realization of these systems encounters difficulties in the stage of useful signal separation in the receiver. These difficulties are related to the fact that the synchronized dynamic receiver system must be capable of generating chaotic oscillations, which must be precisely identical to the transmitted signals. This requirement makes the realization of the proposed communication systems a rather difficult task. This circumstance stimulates the search for new methods of hidden data transfer using the advantages of chaotic oscillations.

Below we consider a hidden communication system in which the useful signal separation from chaos does not require providing for the identical character of oscillations by means of synchronization of the corresponding generators. The task is solved by using two communication channels instead of one. This solution, albeit complicating the transmission line, allows the useful signal to be masked by the superposition of complex external oscillations including chaotic ones. The proposed communication channels are especially promising in optical fiber transmission lines, since they ensure extremely small losses and virtually zero dispersion at a relatively small size of multifiber cables.

A possible variant of the hidden data transfer system using complex oscillations for masking the useful signal is schematically illustrated in Fig. 1. The system comprises a transmitter composed of elements *1–4*, a communication channel (transmission lines *5* and *6*), and a receiver including elements *7* and *8*. A masking signal $x(t)$, produced by a stochastic generator *1*, is distributed between two channels by the dividing element *2*. In one channel, a part of this chaotic signal $\gamma x(t)$ ($\gamma < 1$ is a constant coefficient) passes through a coding device *3* to acquire the coded form $\nu_1(t)$. This signal is added to the useful signal $u(t)$ in the summing device *4*, after which the resulting oscillations are transmitted via the line *5* in the form of $f(t) = \nu_1(t) + u(t)$. Another part of the chaotic oscillation signal from generator *1*, equal to $(1 - \gamma)x(t)$, is transmitted via the parallel line *6* to the coding device *7* identical to *3*, which converts this signal into $\nu_2(t)$. The useful signal is separated in the subtracting device *8*, which determines the useful signal as the difference $f(t) - \nu_2(t)$.

In the proposed scheme of data transfer, the degree of the useful signal distortion is determined only by the nonequivalence of the coding devices employed. The output signal of the subtracting device reproduces the input signal, provided that the coding devices are identical and the divided chaotic signal fractions are equal (for $\gamma = 0.5$), since this would ensure that $\nu_1(t) = \nu_2(t)$. For $\gamma \neq 0.5$, the useful signal can be restored with the aid of certain compensating elements.

It should be noted that an advantage of the scheme presented in Fig. 1 is that the masking signal may employ not only oscillations (chaotic or complex, in particular, multifrequency) generated by some dynamic systems, but the random noise oscillations produced by any noise sources as well.

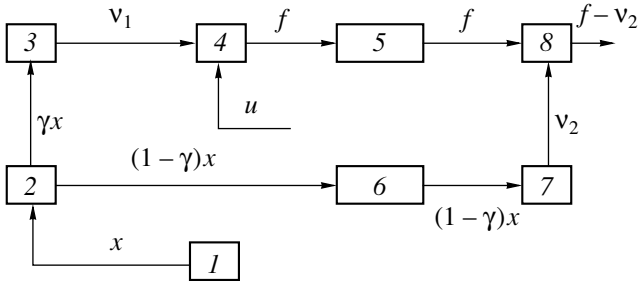

Fig. 1. Schematic diagram of a system of hidden data transfer using masking chaotic oscillations: (*1–4*) transmitter elements; (*5*, *6*) transmission lines; (*7*, *8*) receiver elements. See the text for explanations.

1063-7850/01/2703-0251$21.00

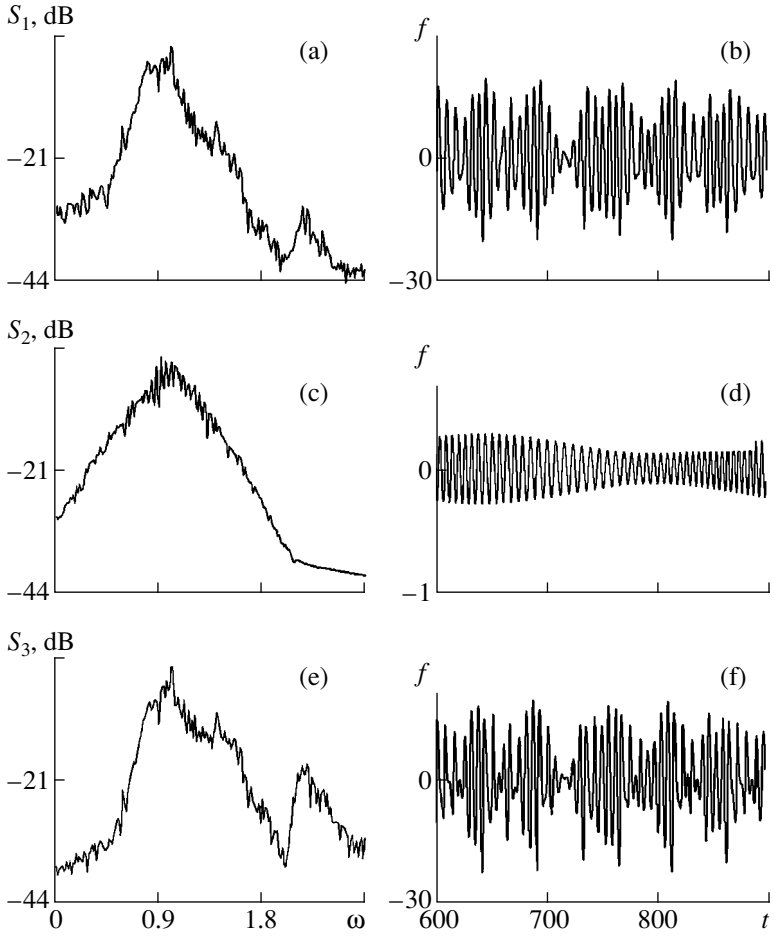

Fig. 2. Operation of the proposed data transfer system illustrated by (a, c, e) signal power spectra and (b, d, f) the corresponding time patterns. See the text for explanations.

For an analysis of the scheme depicted in Fig. 1, it is expedient to employ a masking signal in the form of oscillations generated by a random dynamic system using various sources of chaotic oscillations [2–4]. For example, a convenient generator of chaotic oscillations is offered by a source described by the Rössler equations [10]

$$\begin{aligned} \dot{x} &= -y - z, \\ \dot{y} &= x + \alpha y, \\ \dot{z} &= -\beta z + xy + \delta. \end{aligned} \tag{1}$$

A solution $x(t)$ to this set of nonlinear differential equations with $\alpha = 0.3$, $\beta = 8.5$, and $\delta = 0.4$ represents chaotic oscillations.

Let us employ a useful signal $u(t)$ represented by a harmonic oscillation modulated with respect to amplitude and frequency:

$$u = A_0((1 + M\cos\Omega t)\cos[(\omega_0 + m\cos\Omega t)t]), \tag{2}$$

where A_0, ω_0 are the amplitude and frequency of the harmonic signal, respectively; M, m, and Ω are the amplitude modulation coefficient, the frequency modulation index, and the modulation frequency, respectively.

Relatively simple coding devices *3* and *6* can be represented by second-order filters. In this case, the output signal $\nu_1(t)$ produced by filter *3* from the input oscillations $\gamma x(t)$ is given by a solution to the following differential equation:

$$\ddot{\nu}_1 + (\omega_1/Q_1)\dot{\nu}_1 + \omega_1^2(\nu_1 - \gamma x) = 0, \tag{3a}$$

where ω_1 and Q_1 are the resonance frequency and quality factor of the second-order filter. By the same token, the output signal $\nu_2(t)$ of filter *7* (having the resonance frequency ω_2 and the quality factor Q_2) is described by the equation

$$\ddot{\nu}_2 + (\omega_2/Q_2)\dot{\nu}_2 + \omega_2^2[\nu_2 - (1 - \gamma)x] = 0. \tag{3b}$$

Relationships (1)–(3) determine a mathematical model describing the operation of the proposed data transfer system. Figure 2 shows the results of the numerical analysis of this mathematical model. The spectra were calculated for a masking signal in the form of chaotic oscillations $x(t)$ described above ($\alpha = 0.3$,

$\beta = 8.5$, and $\delta = 0.4$). The parameters of equations (2) and (3) were as follows: $A_0 = 0.2$; $M = 0.1$; $m = 0.01$; $\omega_0 = 1$; $\Omega = 0.02$; $\omega_1 = \omega_2 = 1$; $Q_1 = Q_2 = 4$; $\gamma = 0.5$.

Figure 2a shows the frequency spectrum S_1 of the oscillations $f(t)$ transmitted via line *5*. This spectrum virtually coincides with the spectrum of chaotic oscillations $\nu_1(t)$ because the amplitude of the useful signal $u(t)$ is considerable (by two orders of magnitude) lower than the maximum fluctuation amplitude of the chaotic oscillation process $\nu_1(t)$. Figure 2b shows a fragment of the time pattern of the signal calculated using the same parameters as those for spectrum S_1. The spectrum of oscillations of the useful signal S_2 obtained at the output of the subtracting device *8* in the system with equivalent decoding filters is illustrated in Fig. 2c. As can be seen, this signal is virtually identical to the initial useful signal entering the input of the summing device in the transmitter. The corresponding time pattern is depicted in Fig. 2d. At the same time, the difference of the oscillation processes $f(t)$ and $(1 - \gamma)x(t)$ in the transmission lines (spectrum S_3 presented in Fig. 2e) and the corresponding time pattern (Fig. 2f) reflect the chaotic nature of the masking signal. This indicates that the useful signal cannot be separated in case of nonauthorized access to the communication line.

The above analysis shows the high potential efficacy of the two-channel data transmission for the transfer of confidential data. As noted above, the masking signal can be represented both by chaotic oscillations generated by dynamic systems and by noise signals as well. It should be noted that the operation of the system described above can be adversely affected in practice by the nonequivalence of the coding devices and the transmission line as well as by the time instability of their characteristics. For this reason, the proposed method is especially promising for confidential data transfer via optical fiber communication lines.

Acknowledgments. This study was supported by the Russian Foundation for Basic Research, project no. 98-02-16722.

REFERENCES

1. L. E. Varakin, *Communication Systems with Noise-Like Signals* (Radio i Svyaz', Moscow, 1985).
2. A. R. Volkovskiĭ and N. F. Rul'kov, Pis'ma Zh. Tekh. Fiz. **19** (3), 72 (1993) [Tech. Phys. Lett. **19**, 97 (1993)].
3. P. Colet and R. Roy, Opt. Lett. **19** (24), 2056 (1994).
4. I. I. Matrosov, Pis'ma Zh. Tekh. Fiz. **22** (23), 4 (1996) [Tech. Phys. Lett. **22**, 952 (1996)].
5. V. D. Shalfeev, G. V. Osipov, A. K. Kozlov, and A. R. Volkovskiĭ, Zarubezhn. Radioélektron. Usp. Sovrem. Radioélektron., No. 10, 27 (1997).
6. L. M. Percord, T. L. Caroll, G. A. Johnson, *et al.*, Chaos **7** (4), 520 (1997).
7. É. V. Kal'yanov, Pis'ma Zh. Tekh. Fiz. **23** (14), 66 (1997) [Tech. Phys. Lett. **23**, 564 (1997)].
8. G. D. van Wiggeren and R. Roy, Phys. Rev. Lett. **81** (16), 3547 (1998).
9. É. V. Kal'yanov, Radiotekh. Élektron. (Moscow) **43** (2), 206 (1998).
10. O. E. Rössler, Phys. Lett. A **57** (5), 397 (1976).

Translated by P. Pozdeev

Technical Physics Letters, Vol. 27, No. 3, 2001, pp. 254–255. Translated from Pis'ma v Zhurnal Tekhnicheskoĭ Fiziki, Vol. 27, No. 6, 2001, pp. 77–81.

Investigation of Silicon Implanted with Carbon Ions

S. V. Bulyarskiĭ*, A. S. Ambrozevich*, S. S. Moliver*, T. A. Dzhabrailov*, R. M. Bayazitov, and R. I. Batalov****

** Ul'yanovsk State University, Ul'yanovsk, Russia*

*** Kazan Physicotechnical Institute, Russian Academy of Sciences, Kazan, Republic of Tatarstan, Russia;*

e-mail: ambra@sv.uven.ru

Received October 12, 2000

Abstract—The properties of silicon single crystals implanted with carbon ions were studied by two independent methods. It is demonstrated that the concentration of implanted carbon can be monitored by measuring the density of divacancies. © *2001 MAIK "Nauka/Interperiodica".*

The ion implantation of carbon into silicon leads to the formation of carbon-containing defects and, in addition, introduces defects (e.g., divacancies) into the initial crystal structure of silicon. Divacancies, representing one of the main types of electrically active defects, are stable at room temperature and, hence, are accessible for investigation. The presence of divacancies is an important indication of radiation and/or technological damage in a silicon structure. For example, divacancies appearing upon the implantation of boron, phosphorus, and antimony produce response signals, the intensity of which is proportional to the amount of the substance implanted [1].

We studied *p*-Si samples implanted with carbon ions at an energy of 20 keV to a dose of 6×10^{15} cm^{-2}. In the first series of experiments, the implanted samples were characterized by the photoconductivity spectra measured in the middle IR range at liquid nitrogen temperature. The photoconductivity was excited by globar radiation passed through an MDR-236 monochromator; the photoinduced current was detected in the dc mode with a V6-9 selective voltmeter. The presence of divacancies in the silicon samples studied was confirmed by comparison to the published data [2].

Another series of experiments was performed using the implanted silicon plates with a Schottky barrier formed by the galvanic deposition of gold. Ohmic contacts were obtained by depositing indium onto the back sides of the plates in a VUP-5 vacuum system. The samples with Schottky barriers were characterized by thermostimulated capacitance (TSC). The TSC measurements [3, 4] were performed as described below. The sample was biased in the forward direction (0.5 V) at room temperature and cooled down to liquid nitrogen temperature, after which the bias polarity was reversed (–2 or –3 V). The forward bias ensures occupation of the deep trapping centers, while a change in the bias polarity and magnitude allows us to modify the charged layer thickness and reveal the centers occurring at various depths. In this case, the measurements corresponded to depths of 47 and 57 nm. The TSC measurements were carried out in an automated regime. A constant voltage U was applied to a sample via a decoupling circuit (L_1, C_1). A probing signal applied to the sample from an E7-9 capacitance meter had a frequency f differing from the resonance frequency $f_0 = 1/(2\pi\sqrt{L_0 C_0})$ of the sample circuit. The f value was measured with a frequency meter (Ch3-63) and transmitted to the data channel in the form of a corresponding code. The control program calculated the sample capacity at various temperatures measured by a thermocouple. The signal from the thermocouple was fed to a digital voltmeter (V7-46/1), the coded output sig-

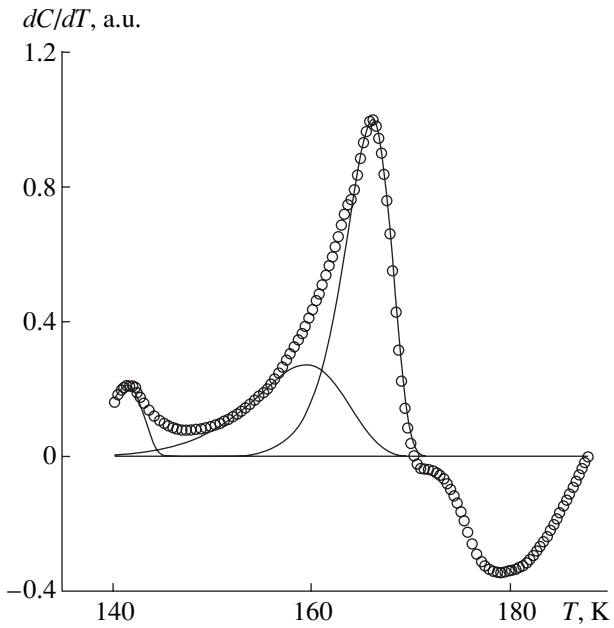

Fig. 1. TSC spectrum of carbon-implanted silicon (d = 47 nm).

1063-7850/01/2703-0254$21.00 © 2001 MAIK "Nauka/Interperiodica"

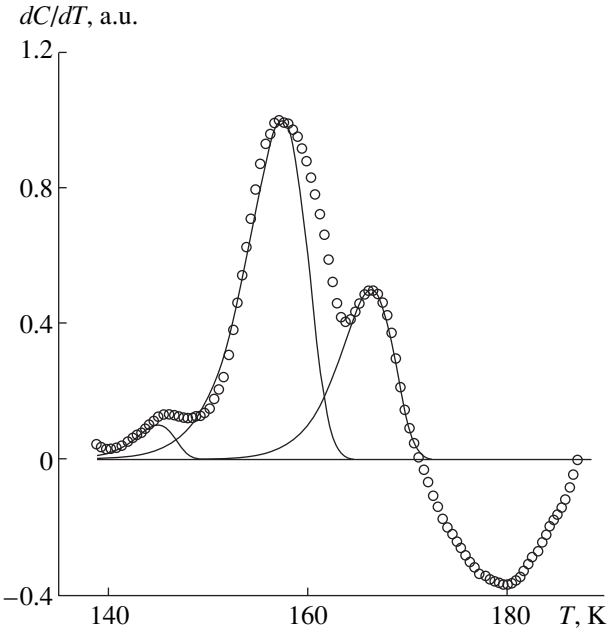

Fig. 2. TSC spectrum of carbon-implanted silicon (d = 57 nm).

nal of which also entered the data channel. The resulting $C(T)$ function was differentiated according to the formula

$$dC/dT = A(T/T_m)^2 \exp[E_t/k(1/T_m - 1/T)]$$
$$\times \exp\{1 - (T/T_m)^2 \exp[E_t/k(1/T_m - 1/T)]\},$$

where A is the signal amplitude, E_t is the trap activation energy, and T_m is the temperature of the peak maximum. The peaks in our TSC spectra frequently overlapped and were separated using the above formula. Typical differential TSC spectra obtained for the two depths are presented in Figs. 1 and 2. The parameters of the deep centers determined from these spectra are summarized in the table.

Characteristics of deep centers in silicon

T_m, K	E_t, eV	σ, cm^{-2}	N_t, cm^{-3}
d = 47 nm			
141	0.23	1.7×10^{-18}	1.6×10^{16}
159	0.42	4.9×10^{-13}	1.6×10^{16}
166	0.27	9.6×10^{-19}	3.3×10^{16}
180	0.55	2.3×10^{-11}	1.8×10^{16}
d = 57 nm			
145	0.23	9.8×10^{-19}	5.2×10^{15}
158	0.42	5.1×10^{-13}	5.0×10^{15}
166	0.27	9.6×10^{-19}	1.0×10^{16}
180	0.55	2.3×10^{-11}	6.0×10^{15}

The TSC measurements revealed four deep centers at both depths. The centers corresponding to the peaks at 141 (145) and 159 (158) K represent divacancies. The signal observed at 166 K corresponds to positively charged interstitial carbon ions C_1^+ [4]. The negative peak at 180 K is apparently also related to the implanted carbon, since a change in the probing depth affected the concentration of these centers. As can be seen from the table, each divacancy corresponds to approximately two carbon atoms at both depths, while the concentration of defects at a greater depth (d = 57 mm) is about one-third of that at a shallower depth. Thus, the concentration of implanted carbon can be monitored by measuring the density of the divacancies.

Acknowledgments. One of the authors (S.S.M.) gratefully acknowledges support of the Russian Foundation for Basic Research (project no. 98-02-03327).

REFERENCES

1. V. Avalos and S. Dannefaer, Phys. Rev. **B58** (3), 1331 (1998).
2. R. G. Humphreys, S. Brand, and M. Jaros, J. Phys. C **16** (12), L337 (1983).
3. S. V. Bulyarskiĭ and N. S. Grushko, *Generation-Recombination Processes in Active Elements* (Mosk. Gos. Univ., Moscow, 1995).
4. S. V. Bulyarskiĭ and S. I. Radautsan, Fiz. Tekh. Poluprovodn. (Leningrad) **15**, 1443 (1981) [Sov. Phys. Semicond. **15**, 836 (1981)].
5. V. S. Vavilov, N. P. Kekelidze, and L. S. Smirnov, *Radiation Effects in Semiconductors* (Nauka, Moscow, 1988).

Translated by P. Pozdeev

Technical Physics Letters, Vol. 27, No. 3, 2001, pp. 256–257. Translated from Pis'ma v Zhurnal Tekhnicheskoĭ Fiziki, Vol. 27, No. 6, 2001, pp. 82–85.

Spontaneous Arc Quenching in the Ecton Model

S. A. Barengol'ts and G. A. Mesyats

Institute of Electrophysics, Ural Division, Russian Academy of Sciences, Yekaterinburg, Russia

e-mail: sb@nsc.gpi.ru

Received November 8, 2000

Abstract—It is shown that the phenomenon of spontaneous quenching of a vacuum arc is determined by a finite ecton lifetime and the related cyclic character of processes occurring in a cathode spot of the arc. The main experimental results are explained within the framework of a statistical model based on the ecton model of the cathode spot operation. © *2001 MAIK "Nauka/Interperiodica".*

Spontaneous quenching of a weak-current arc operating in vacuum is a phenomenon that is very difficult to explain. Until now, there were no serious attempts at the theoretical investigation of this effect. As a result, a large volume of experimental material gained in the course of numerous labor-consuming investigations is unclaimed and still waits for interpretation. This is rather surprising in view of the large practical significance of the problem.

We believe that most important contribution to the study of spontaneous arc quenching was made by Kesaev [1]. He studied a large number of cathode materials and established two principal empirical relationships determining the arc quenching process. According to the first relationship, the number N of arcs operating at a time instant t is described by the random law

$$N = N_0 \exp\left(-\frac{t}{\tau}\right), \quad (1)$$

where N_0 is the total number of arcs studied and τ is the average arc lifetime. The second relationship indicates that τ is an exponential function of the current:

$$\tau = \tau_0 \exp[\varphi(i - i_{thr})], \quad (2)$$

where i_{thr} is the threshold current and τ_0 is the average discharge duration for $i = i_{thr}$.

Previously [2, 3], one of the authors developed an ecton model of the cathode spot of a vacuum arc. According to the main idea of this model, a metal cathode surface features microexplosions of the metal caused by a high concentration of energy as a result of Joule heating. The microexplosions are accompanied by the emission of electron bunches, whereby 10^{11}–10^{12} electrons are ejected within ~10^{-8} s. These emissions lead to the formation of a plasma interacting with the solid and liquid metal areas on the cathode surface, giving rise to new microexplosions. Thus, a self-sustained arc operation process is developed, which implies an intrinsic instability of the vacuum arc. Kesaev [1] showed that spontaneous arc quenching is a manifestation of this instability.

The concept of the intrinsic instability of the vacuum arc operation underlies the ecton model. Based on this model, we analyzed the phenomenon of spontaneous arc quenching [4] and showed that the arc instability is explained by the finite ecton lifetime and the related cyclic character of processes occurring in a cathode spot of the arc.

The main assumption of the ecton model is that the cathode spot of a vacuum arc consists of separate cells, each cell conducting a current not exceeding double the value of the threshold current i_{thr}. The cells possess a finite lifetime t_c called the cell cycle. The cycle includes two stages, the first corresponding to the ecton operation (during a time t_e) and the second featuring the new ecton initiation (during a shorter time t_i) instead of the vanishing one. Therefore, the probability that the ecton does not exist in the cell is

$$\alpha = \frac{t_i}{t_e + t_i}, \quad (3)$$

and the probability of the ecton operation is

$$\beta = 1 - \alpha = \frac{t_e}{t_e + t_i}. \quad (4)$$

The α value characterizes the efficiency of the ecton restoration (initiation) mechanism. If the arc current is smaller than the double threshold value $2i_{thr}$ a cathode spot will contain a flickering cell in which the ecton vanishes and appears again. For $i \gg i_{thr}$, the number of cells is

$$L = \frac{i}{2i_{thr}}. \quad (5)$$

The probability that M cells (and the corresponding ectons) are simultaneously operating at a time instant t

1063-7850/01/2703-0256$21.00 © 2001 MAIK "Nauka/Interperiodica"

can be expressed as [4]

$$\omega = \left[\frac{L!}{M!(L-M)!}\beta^M\alpha^{L-M}\right]^{t/t_c}, \quad (6)$$

where t_c is the cycle duration.

Let us define the moment of arc quenching as corresponding to the event when not a single ecton is operating. The probability that the arc exists at the time instant t is

$$\omega = [1-\alpha^L]^{t/t_c}. \quad (7)$$

Since $\alpha^L \ll 1$ for $L > 1$, Eq. (7) implies that

$$\omega \approx \exp\left(-\frac{t\alpha^L}{t_c}\right). \quad (8)$$

Therefore, the total number of the initiated arcs being N_0, the number of arcs operating at the time instant t is

$$N \approx N_0\exp\left(-\frac{t\alpha^L}{t_c}\right). \quad (9)$$

This expression coincides in form with the empirical relationship (1) and, hence, the quantity

$$\tau = \frac{t_c}{\alpha^L} \quad (10)$$

represents the average time of the arc operation.

As can be readily shown, the expressions for $\tau(i)$ in Eqs. (2) and (10) also coincide in form. Indeed, relationship (2) yields

$$\ln\frac{\tau}{\tau_0\exp(-\varphi i_{thr})} = \varphi i, \quad (11)$$

while Eq. (10) with an allowance for formula (5) yields

$$\ln\frac{\tau}{t_c} = \frac{\ln(\alpha^{-1})}{2i_{thr}}i. \quad (12)$$

Using Eqs. (11) and (12), we obtain

$$\varphi = \frac{\ln(\alpha^{-1})}{2i_{thr}}, \quad (13)$$

and

$$t_c = \tau_0\exp(-\varphi i_{thr}). \quad (14)$$

Upon substituting (13) into (14), we arrive at

$$t_c = \tau_0\alpha^{1/2}. \quad (15)$$

Thus, we have related parameters of the empirical formulas (1) and (2) obtained by Kesaev [1] to the quantities characterizing the ecton model. For example, tungsten and copper cathodes are characterized by $\alpha \approx 0.2$ and $t_c \approx 30$ ns. According to relationship (10), the average arc lifetime for $L = 2$ is $\tau \sim 10^{-6}$ s. This estimate agrees with the experimental value reported in [5].

Acknowledgments. This study was supported by the Russian Foundation for Basic Research (RFBR), project no. 99-02-18234, and by a joint RFBR–INTAS project no. 97-0663.

REFERENCES

1. I. G. Kesaev, *Cathodic Processes in Electric Arc* (Nauka, Moscow, 1968).
2. G. A. Mesyats, IEEE Trans. Plasma Sci. **23** (6), 878 (1995).
3. G. A. Mesyats, *Ectons in Vacuum Discharge: Breakdown, Spark, Arc* (Nauka, Moscow, 2000).
4. S. A. Barengolts, G. A. Mesyats, and A. V. Chentsov, in *Proceedings of the 18th International Symposium on Discharges and Electrical Insulation in Vacuum, Eindhoven, 1998*, p. 219.
5. B. Juttner and V. F. Puchkarev, *Handbook of Vacuum Arc: Science and Technology*, Ed. by R. L. Boxman, P. J. Martin, and D. M. Sanders (Noyes Publ., Park Ridge, 1995), p. 73.

Translated by P. Pozdeev

Technical Physics Letters, Vol. 27, No. 3, 2001, pp. 258–259. Translated from Pis'ma v Zhurnal Tekhnicheskoĭ Fiziki, Vol. 27, No. 6, 2001, pp. 86–89.

Melting and Crystallization of Copper, Silver, and Gold Droplets

V. D. Aleksandrov, V. N. Aleksandrova, A. A. Barannikov, N. V. Dobritsa, N. E. Malinovskaya, and S. A. Frolova

Donbass State Academy of Civil Engineering and Architecture, Donetsk, Ukraine

Received August 21, 2000; in final form, October 25, 2000

Abstract—The crystallization kinetics in 0.5-g droplets of melted copper, silver, and gold (special purity grade metals) cooled in vacuum at a rate of 0.01 K/s was studied. Under these experimental conditions, the physical supercooling observed in all three metals prior to crystallization was virtually zero. An analysis of the values of supercooling obtained in this study together with the data obtained previously under the same conditions showed that supercooling increases in a regular manner with the number of electrons on the outermost *p* level.

Data published on the values of $\Delta T_{LS} = T_L - T_S$ (where T_L and T_S are the equilibrium melting and solidification temperatures, respectively) and $\Delta T_{ph} = T_L - T_{min}$ (T_{min} is the crystallization onset temperature in the region of supercooling) for metals (including Cu, Ag, and Au) are rather contradictory. Considerable supercooling (up to 200–500 K) reported in [1–5] was mostly observed under very special conditions (e.g., particles of micron size cooled at a rate of up to ~10^{10} K/s). Such supercooling was never observed in large drops (weighing from one to several grams) cooled at a normal rate [6–11]. Unfortunately, almost no data on supercooling in Cu, Ag, and Au droplets under these conditions are available.

Taking into account that the value of precrystallization supercooling ΔT_{ph}^- may depend on many factors, we have performed a systematic investigation of the effects of superheating ΔT^+ relative to the melting temperature, duration τ of the isothermal annealing of melted droplets, and cooling rate (from 0.001 to 8.0 K/s) on the crystallization of Cu, Ag, and Au (1.0 g samples). The study was performed by the method of sequential thermal cycling (STC) [9–11].

The experiments were carried out in specially designed resistively heated furnaces mounted in a vacuum system of the VUP-4 type evacuated to a residual pressure of ~10^{-5} Torr in a dynamic pumping regime. The electric heater and thermocouple leads were connected via vacuum feedthroughs to a controlled power supply and measuring unit of the PTT type. The samples were melted in alundum crucibles. The temperature was measured with 0.2-mm-diam. chromel–alumel thermocouple with one junction kept in a thermostat at 0°C (ice–water mixture) and the other (protected with an alundum coat) placed into the sample. The power supply control and temperature monitoring was effected by a programmable device capable of switching the furnace on and off according to a preset regime and recording the sample temperature T as a function of time τ with the aid of a chart recorder of the KSP-4 type. During the STC experiments, the sample temperature was varied from $T_a = T_L - 100$ K to $T_b = T_L + 100$ K, where T_L is the melting temperature of a given metal. The lower boundary T_a of the heating–cooling cycles was the same in all cycles, while the upper boundary T_b was varied, toward increase or decrease (by 1–2 K) from one cycle to another.

The error of the sample temperature determination was 0.10–0.15 K. The reliability of the data was confirmed by the results of multiply repeated measurements (each experiment including up to 100 cycles).

It was found that the heating of the Cu, Ag, and Au samples was accompanied by the appearance of endothermicities at T_L = 1356.2 (Cu), 1235.0 (Ag), and 1337.0 K (Au) in the temperature rise diagrams. These values virtually coincide with the reference melting temperatures of these metals. On cooling the melted Cu, Ag, and Au samples, the temperature variation curves exhibited exothermal effects, manifested by the so-called crystallization plateaus at T_S = 1355.2 (Cu), 1234.2 (Ag), and 1336.4 K (Au). The corresponding temperature differences $\Delta T_{LS} = T_L - T_S$ for Cu, Ag, and Au were 1.0, 0.8, and 1.6 K, respectively.

The presence of the exothermal plateau at T_S is indicative of the equilibrium character of the melt crystallization at this temperature. At the same time, the results of our experiments showed virtually no physical supercooling ($\Delta T_{ph}^- = T_L - T_{min}$) in melted Cu, Ag, and Au samples weighing 1.0 g (irrespective of the preliminary overheating (ΔT^+), the duration of isothermal annealing above T_L (varied from 5 min to 6.5 h), and the

Data on the outermost electron shell configuration (s_p), coordination number Z for atoms in the melt (near the melting temperature), and the physical supercooling ΔT_{ph}^- for crystallization of 1.0-g metal droplets

Elements	Subgroup	Outer electron shell configuration	Z	ΔT_{ph}^-, K
Cu, Ag, Au	Ic	s^1p^0	12	0
Zn, Cd	IIc	s^2p^0	12	0
Al, Zn	IIIa	s^2p^1	11.7	1–3
Sn, Pb	IVa	s^2p^2	8.0–9.0	5–10
Sb, Bi	Va	s^3p^3	6.5–7.5	60 (Sb), 30 (Bi)
S, Te	VIa	s^3p^4	1.7	60 (S), 100 (Te)

cooling rate (0.001–8.0 K/s). Moreover, variation of the cooling rate in this interval did not affect the corresponding ΔT_{LS} values either (i.e., the equilibrium crystallization temperatures were not affected). The zero supercooling ($\Delta T_{ph}^- = 0$) indicates that Cu, Ag, and Au do not exhibit crystallization of the explosion type, whereby the temperature jumps from T_{min} to T_L (or T_S) as in the samples of bismuth, antimony, tin, and some other metals of the same weight crystallized under identical experimental conditions.

We attempted to establish a relationship between some crystallochemical characteristics of substances and the physical supercooling observed during crystallization of the melts of various elements (see table). For this purpose we analyzed the values of supercooling obtained in our preceding experiments using the same STC method [9–14]. The experimental data were selected so as to correspond to identical conditions: sample weight, 1.0 g; metal purity, special grade; cooling rate, 0.01 K/s; medium, vacuum ~ 10^{-5} Torr; preliminary overheating ΔT^+, 30 K above T_L (for ΔT^+ above this level, the average precrystallization supercooling cease to change); isothermal annealing at $\Delta T^- = 30$ K, 10 min; crucible material, alundum; thermocouples, chromel–alumel, etc.

An analysis of the experimental data showed that, depending on the element position in the Periodic Table, the ΔT_{ph}^- value grows in a regular manner upon increasing the number of p electrons in the outermost electron shell, changing the type of chemical bonding, and decreasing the coordination number Z for atoms in the liquid phase, etc. [5, 15–18].

REFERENCES

1. D. N. Hollomon and D. Tornbull, Usp. Khim. Nauk **1**, 30 (1956).
2. B. Chalmers, *Principles of Solidification* (Wiley, New York, 1964; Metallurgiya, Moscow, 1968).
3. V. K. Yatsimirskiĭ, Zh. Fiz. Khim. **51** (5), 1041 (1977).
4. I. H. Perepezko, Mater. Sci. Eng. **65** (1), 125 (1984).
5. D. E. Ovsienko, Metallofiz. Noveĭshie Tekhnol. **21** (3), 31 (1999).
6. V. I. Danilov, *Liquid Structure and Crystallization* (Akad. Nauk Urk. SSR, Kiev, 1956).
7. B. I. Kidyarov, *Kinetics of Crystal Formation from Liquid Phase* (Sib. Otd. Akad. Nauk SSSR, Novosibirsk, 1979).
8. S. N. Zadumkin, Kh. Ch. Ibragimov, and D. T. Ozniev, Izv. Vyssh. Uchebn. Zaved., Tsvetn. Metall., No. 1, 82 (1979).
9. V. D. Aleksandrov and V. I. Petrenko, Pis'ma Zh. Tekh. Fiz. **9** (22), 1354 (1983) [Sov. Tech. Phys. Lett. **9**, 582 (1983)].
10. V. D. Aleksandrov and A. A. Barannikov, Khim. Fiz. **17** (10), 140 (1998).
11. V. D. Aleksandrov and A. A. Barannikov, Pis'ma Zh. Tekh. Fiz. **24** (14), 73 (1998) [Tech. Phys. Lett. **24**, 573 (1998)].
12. V. D. Aleksandrov and V. I. Petrenko, Rasplavy **2** (5), 29 (1988).
13. V. D. Aleksandrov, M. R. Raukhman, V. I. Borovik, *et al.*, Metally, No. 6, 186 (1992).
14. V. D. Aleksandrov, Neorg. Mater. **28** (4), 709 (1992).
15. V. D. Aleksandrov and A. A. Barannikov, Ukr. Khim. Zh. (2000) (in press).
16. Ya. I. Dutchak, *X-ray Radiography of Liquid Metals* (Vishcha Shkola, Lvov, 1977).
17. A. D. Skryshevskiĭ, *Structural Analysis of Liquids and Amorphous Solids* (Vysshaya Shkola, Moscow, 1980).
18. L. I. Tatarinova, *Structure of Amorphous Solids and Liquids* (Nauka, Moscow, 1983).

Translated by P. Pozdeev